NEGATIVE ION MEASUREMENTS IN RF AND DC TEMPORALLY MODULATED HYDROGEN VOLUME ION SOURCES.

A thesis for the degree of
PHILOSOPHIAE DOCTOR

Presented to
DUBLIN CITY UNIVERSITY

By
DEIRDRE BOILSON M.Sc.
School of Physical Sciences
DUBLIN CITY UNIVERSITY

Research Supervisor: Dr. Michael B. Hopkins
External Examiner: Dr. Peter Massmann.

May 2000

Declaration

I hereby certify that this material, which I now submit for assessment on the programme of study leading to the award of Doctor of Philosophy is entirely my own work and has not been taken from the work of others save and to the extent that such work has been cited and acknowledged within the text of my work.

Signed: Deirdre Boilson ***ID No.:*** 94971111
Candidate

Date: 10/09/00.

Acknowledgements

I would like to thank all those who helped throughout the duration of this work, especially my supervisor Dr. Mike Hopkins for his help, support and encouragement over the last few years. Also thanks to the Plasma Research Laboratory, Dr. David Vender, Dr. Miles Turner, Dr. Brendan Crowley, Dr. Paul McNeeley, Neil, George, Roberto, Anne and especially Samantha, for making working in this group a happy and memorable experience, and the collaborative labs in Garching and Cadarache for all their help over the years.

I would like to acknowledge the excellent technical support from Des Lavelle, Alan Hughes, Al Devine, John Brosnan and Declan Ledgwidth.

All my friends, Dr. Andy Grey, Andrew, Mohammad, David, Fiona, Ronan and numerous other members of staff who have helped, cheers guys.

A special mention has to go to the other two of "The Three Amigos", Dr. Oonagh Meighan, and Dr. Eilish Mc Loughlin, who both kept me sane through the late nights when we paced the corridors of the physics department together, for the laughs, tears, frustration and exhilaration that we have shared together, Thanks girls, and to John for all the fun times shared, and for keeping a smile on my face, Thank you.

And most importantly, my parents and sisters, Barbara and Elizabeth, for their blind support, both financially and mentally, no mater how difficult I made it on them, they never gave up on me! And Dr. John Crowe, without whom this would never have been possible.

Table of Contents

Chapter 3 - Diagnostic Tools

Chapter Four - Plasma Parameter Measurements

Chapter Five - Negative ion Measurements

Chapter Six - Argon Seeding of Negative Ion Volume Ion Sources

Appendix A
Appendix B

Abstract

Negative ion research is stimulated by the need for high power and high density neutral beams for neutral beam heating systems to be used in proposed nuclear fusion reactors. Extensive research has been carried out on the enhancement of the production of negative ions from hydrogen/deuterium discharges. The negative ion sources used at present are being investigated in order to optimise current densities of H^-/D^- for future fusion machines.

In this thesis low pressure radio frequency (RF) hydrogen plasmas are investigated and compared to filament driven hydrogen plasmas to understand further the physics in the two different modes, and to investigate the proposal of the utilisation of an RF volume ion source in he application of neutral beam injection (NBI) systems for the proposed nuclear fusion reactors of the future.

Tuned Langmuir probes are used as a diagnostic method to measure different plasma parameters as a function of pressure and power. The spatial variations of these parameters are examined within the bulk plasma, and the effect of an applied magnetic field investigated.

The temporal filter concept is examined with a view to enhancing negative ion generation in the afterglow of an RF temporally modulated discharge. It is proposed that by modulating the RF discharge, the dominant destructive mechanism, collisional detachment (CD), will become negligible and the dominant production mechanism, dissociative attachment (DA), will be optimised, hence allowing optimum production of negative ions in the volume ion source.

A laser photodetachment technique was used to determine negative ion densities in temporally resolved filament generated and radio frequency powered hydrogen plasmas, and experimental data compared to theoretically modelled results.

In an effort to enhance negative ion production, the addition of argon to the hydrogen discharge was examined. All plasma parameters were investigated and an increase in negative ion density observed. A model of the reaction rates for production and destruction in the discharge lead to a possible explanation for the increase detected.

Langmuir probe measurements and laser photodetachment results are presented which show that the enhanced production of H^- density which is achieved with a temporally modulated filament driven discharge is also achievable in a temporally modulated radio frequency hydrogen plasma.

List of Figures

Chapter One

Introduction to Plasma Physics Research

1.0 Introduction

Thermonuclear reactions have been taking place in the universe since its creation in the presumed cosmic "big bang" of some 15 billion years ago. Significant reactions have taken place on earth, however, only since November 1952 when the first fusion or hydrogen bomb was exploded. The high temperatures needed to sustain the thermonuclear reactions in the fusion bomb are provided by a fission bomb as a trigger.[1]

A sustained and controlled thermonuclear power source a fusion reactor - is proving much more difficult to achieve. The goal, however, is being vigorously pursued because many see the fusion reactor as the ultimate power source of the future, at least as far as the generation of electricity is concerned.[2]

Negative ion research is in part inspired by this objective. Proposed nuclear fusion reactors may require the neutralisation of charged particle beams with currents of several amps and energies up to 1MeV. Negative rather than positive ions are envisaged for this purpose due to their neutralisation efficiency at the high energies that the next generation of reactors will require.

Over the years, the development of low-pressure plasma physics has found other important applications in the semiconductor industry. Radio frequency generated discharges are the principal type used in the plasma processing industry, in etching and sputtering applications [3, 4, 5, 6], as they do not have some of the disadvantages associated with DC discharges, as e.g. limited cathode lifetime.

As a result of the applications to the semiconductor industry, a significant amount of research has been carried out to investigate power input to the etch rates [7,8], energy transfer to the wafers [9,10], and the positive and negative ions formed [11].

The field of plasma physics has developed very rapidly due to the aforementioned applications. The intention of this chapter is to introduce the concept of plasma physics and its role in thermonuclear fusion as a solution to the energy crisis.

1.1 Nuclear Fusion

The attractiveness of fusion over fission is easily understood. fusion, unlike its fission counterpart, does not necessarily produce long lived radioactive isotopes and therefore would greatly reduce the problem of the large quantities of radioactive waste currently being produced by fission reactors.[12] Also the fuel, deuterium, would be very cheap, widely available, and most importantly virtually limitless. It has been estimated that there is enough deuterium in the oceans of the world to provide energy at the current rate of usage for 1000 million years!

In nuclear fusion, two nuclei combine to form a heavier one whose binding energy per nucleon is greater. The difference in binding energies is liberated in the process. To bring about a nuclear fusion reaction, the initial nuclei must be moving rapidly when they collide to overcome their electrical repulsion. Nuclear fusion is the source of energy in the sun and stars, where the high temperatures in the interiors mean that nuclei there have sufficiently high velocities and the high pressures and large volumes mean that nuclear collisions occur frequently. In the operation of a hydrogen bomb, a fission bomb is first detonated to produce the high pressure and temperature necessary for fusion reactions to occur. The problem in constructing a fusion reactor for controlled energy production is to contain a sufficiently hot and dense mixture of suitable isotopes for long enough to produce a net energy output.

The least difficult to achieve reaction for terrestrial use appears to be the deuteron-triton reaction,

$$^{2}D^{+} + ^{3}T^{+} \rightarrow He^{2+}(3.53MeV) + n(14.06MeV)\ \text{(D-T)}, \qquad \textit{Equation 1.1}$$

The cross-section for this fusion reaction is appreciable only for incident energies above 10 keV. One route to establish controlled nuclear fusion on earth is to create a dense and well-confined plasma in which the thermal energies are in the 10 keV range. The problem of heating and containing such a plasma is responsible for the rapid growth in the science of plasma physics since the early 1950's.

There are two main solutions proposed for this problem, inertially confined fusion and magnetically confined fusion. The latter consists of an extremely hot and dense plasma confined by magnetic fields where the most popular configuration is the doughnut shaped TOKAMAK.[13]

1.2 The TOKAMAK

TOKAMAK, a Russian acronym for "toroidal magnetic chamber" refers to a thermonuclear fusion device, first developed in the USSR. It is thought to be a promising way of achieving a self-sustaining thermonuclear fusion reaction.

In a TOKAMAK the charged particles that make up the hot plasma are confined by a particular magnetic field configuration to the geometry of a doughnut or torus. As Fig. 1.1 suggests, the confining magnetic sheath of helical lines of force, of which only one is shown in this schematic, spiral around the plasma "doughnut". The magnetic forces acting on the moving charges of the plasma keep the hot plasma from touching the walls of the vacuum chamber.

Fig. 1.1 **Representation of TOKAMAK for Use in Neutral Beam Injection (NBI).**

The helical magnetic field is the resultant of two component fields; the toroidal field component B_t is generated by a current i_p in windings that wrap around the toroidal vacuum chamber. The so-called poloidal field component generated by a toroidal current i_t that is induced in the plasma itself by an alternating current in the windings of the transformer-magnet arrangement (not shown). This induced toroidal current is also used to heat the plasma ohmically up to a temperature limited by the electrical conductivity increasing with temperature. Additional heating may be provided by firing one or more beams of energetic neutral particles into the plasma, neutral beam injection (NBI) or by electromagnetic wave heating.[14] There are three main forms of wave heating:

electron cyclotron resonance heating (ECRH): An electromagnetic wave is coupled into the plasma at a frequency identical to the electron cyclotron resonance frequency, (around 200GHz, for the magnetic fields typically applied). By this means the energy of the electrons can be increased resulting in a higher plasma temperature.

Lower hybrid resonance heating (LHRH): The frequency (~2 GHz) of these electromagnetic waves is such that they will not penetrate to the axis of the fusion plasma.

Ion cyclotron resonance heating (ICRH): This method involves coupling of an electromagnetic wave to the plasma, but in this case the frequency is equal to that of the ion cyclotron resonance frequency or higher harmonics, (applied frequency range 35 - 100 MHz). Coupling of ICRH power turns out to increase the ion temperature.[15]

1.3 Neutral Beam Injection Heating

The basis of neutral beam injection is straightforward. Fast high power neutrals are injected into a magnetically confined plasma. These neutrals penetrate the plasma unaffectedby the magnetic field, and deposit their energy through collisions with the ionised gas. This transfer of energy results in the heating up of the fusion plasma. The neutral beams with the energy, power and collimation required for these injection systems are only achievable through the neutralisation of high power positive or negative ions beams. [16]

Dense, high-energy ion beams are generally produced at low energy by electron attachment in or ionisation of a source gas. They are extracted and accelerated most frequently in an electrostatic field. These beams are then passed through a neutraliser usually a gas or plasma target and the resultant neutral beam is used to heat the fusion plasma. The neutrals being used are hydrogen or deuterium, and so most of the research is being carried out on these sources.

1.4 Negative Ions versus Positive Ions

The proposed fusion reactors require the neutralisation of charged particle beams of currents of several amperes and energies of 1MeV. To produce an energetic beam for neutral beam injection the ions must be accelerated to the required energies. Positive ions prove to be not suitable for this operation, which is explained in the following graph Fig. 1.2 . [17]

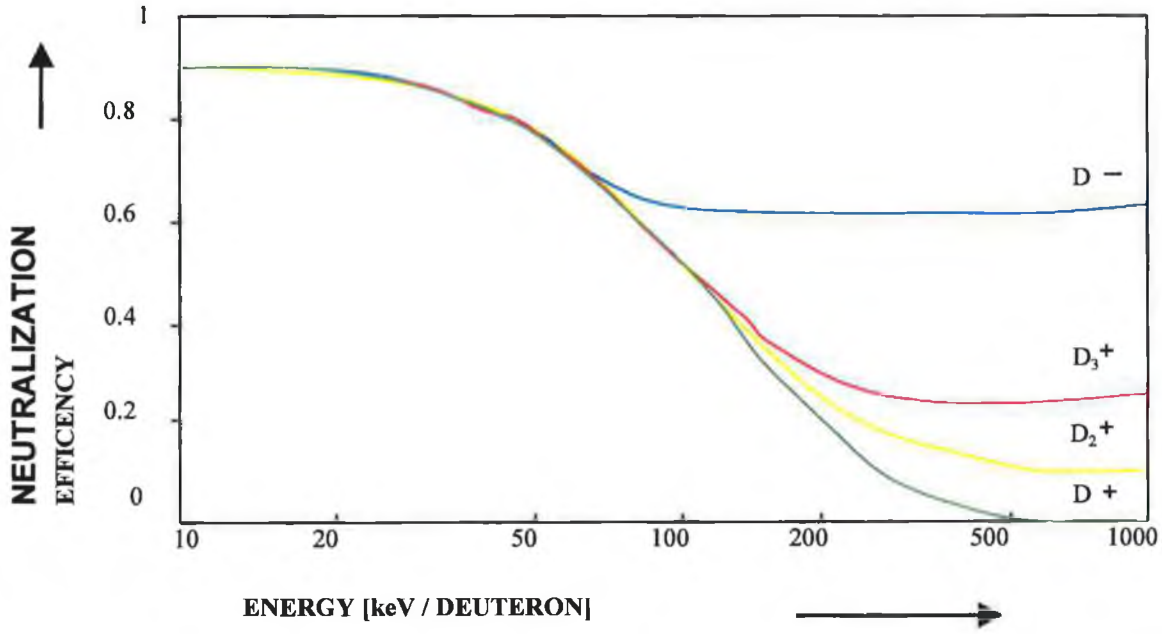

Fig. 1.2 **Graphical Representation of Neutralisation Efficiency versus Energy (at optimum gas target density).**

Even though it is easier to produce a high current beam of positive deuterium ions than negative deuterium ions, from the graph it can be seen that at 1 MeV the positive deuterium ions are not efficiently neutralised. At these high energies the neutralisation drops away dramatically, so for the proposed nuclear fusion reactors the neutralisation would be too small to be seriously considered. With 60% the neutralisation efficiency of the negative ions at these high energies is much better.

The conversion rate of D^- ions as a function of gas target density is redrawn in Fig. 1.3 using the corrected cross sections of [18]. It can be seen that for 1 MeV particles the optimum neutralisation of ~60% is obtained at a gas target thickness of $n \times l \sim 10^{20}\ m^{-2}$.

As much as a good conversion is welcome for neutralisation as much it is undesirable in the extraction and accelerator region, where electron stripping may lead to substantial beam losses and undue electron power loads. It should be noted that stripping can "happen" relatively easily, as the electron affinity of D^- is only 0.75 eV. It is therefore essential to keep the pressure in those regions as low as possible, e.g. by operating the negative ion source at very low pressure.

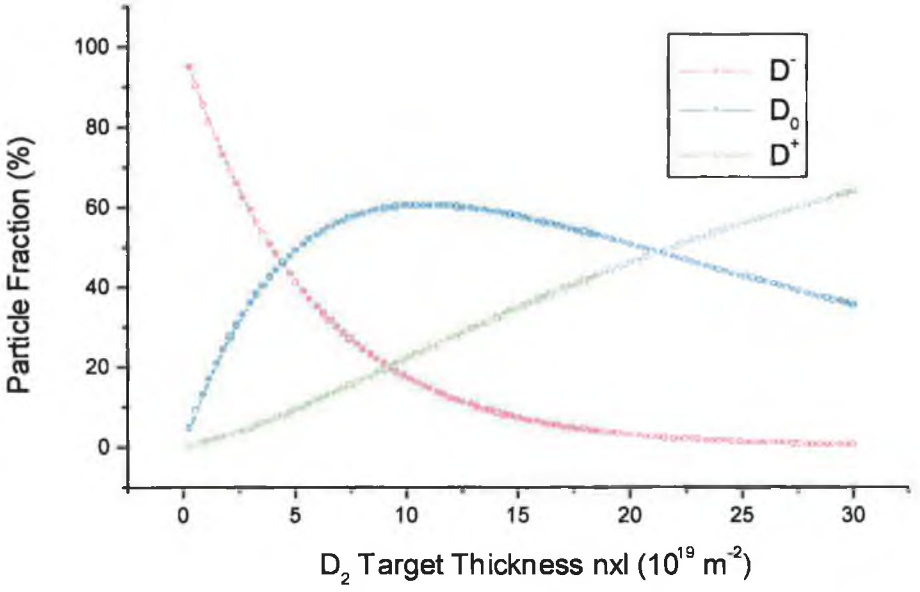

Fig. 1.3 **Conversion of D^- Ions as a Function of D_2 Gas Target Density**[18]

Thus the need for high power low-pressure negative ion sources for NBI becomes apparent. It is thought e.g. that the ITER tokamak may require NBI powers of up to 100MW. This means a negative ion current of 150 A, if conventional gas neutralisers are used.

Two different mechanisms for the production of negative ions for NBI are being explored. These are volume production and surface conversion.

1.5 Surface Conversion Sources

Surface conversion sources have been under investigation as a source of production for negative ions[19,20]. In these sources the negative ions are produced on the surface of a metal target. Electrons of energy of-0.75 eV are required to populate the affinity level of the hydrogen atom. Electrons like these are found in the conduction bands of metals in the form of electron gas. The work function of the metal determines the bonding strength of the electrons, typically 2 - 5 eV. When an atom is brought close to the surface of a metal the affinity level drops and broadens as the attractive interaction of the energy levels in the metal become stronger. When the electron states of the metal are equal or above the affinity level of the hydrogen atom, charge transfer can occur, hence resulting in a negative ion. A positive ion approaching the surface can easily become neutralised as the ionisation potential is usually far below the metal electron levels. The surface ionisation potential depends on the metallic surface work function, increasing as the work function decreases. This effect is used to generate negative ions by scattering a positive ion beam from a low work function metal target. The incident beam is neutralised and the hydrogen atom has the possibility of being ionised in the reflected beam. Beam currents have been already been shown with a negative ion formation probability of up to 60 %. [21].

A typical surface conversion source consists of a plasma chamber in which the low work function metal target is situated. The plasma is brought into contact with the target, which is negatively biased w.r.t. the plasma. The target attracts the positive ions, which can then be either reflected from or embedded into the surface. The incoming proton beam could also sputter adsorbed particles off the target and the beam of backscattered or sputtered atoms can be ionised to form negative hydrogen ions. Because the target is negatively biased, the negative ions produced are repelled away from the target into the extractor region.

One of the advantages of the surface conversion sources is the fact that the process is dependent on the density of atoms rather than on the density of molecules, this source then can operate without the need of high background gas pressures. The disadvantage of this type of source however lies in the fact that the ions produced are generated by the process of sputtering or backscattering, and because the temperature is quite high the extracted beam is more divergent than one generated by a volume production source (see below).

1.6 Caesiated Sources

Most of the work carried out on caesiated sources was concentrated on the use of the surface conversion sources explained in Section 1.5 above. [22,23]. Since hen however the addition of caesium to a volume ion source (see below) has been investigated, and it has been found that the caesiated sources have the effect of enhancing the negative ion density in the source.

There are a number of ways in which the Cs is thought to increase the H^-density in the volume ion source. [24] Because Cs has a high ionisation rate at low electron energies in comparison to hydrogen, the Cs is more easily ionised and therefore there is an increased plasma density. The Cs ions can also drift more easily than the hydrogen through the magnetic fields that separate the driver from the extractor regions of the source, and therefore the electron density in the extractor region will increase. Increasing the electron density in this region will result in the increased production of H^- through increased dissociative attachment of slow thermal electrons to hydrogen molecules. This is explained in greater detail in Section 1.7.

In addition to this the Cs atoms may further cool the electrons in the extraction region through collisions and therefore there is a possibility of the Cs reacting with H^{3+}, resulting in the enhanced density of vibrational levels which are then available for H^-production.[24]

In surface conversion sources, the Cs is adsorbed onto the target surface. This lowers the work function of the target, which increases the probability of the transfer of charge from the metallic surface to the hydrogen atoms near the surface. It has been reported that the addition of Cs can give enhancements of a factor of four to the negative ion density and also reduce the operating pressure of the source.[25]. The disadvantage of caesiated sources however is that the Cs may reach the accelerator region and therefore can cause voltage breakdown when extracting and accelerating the ion beam.

1.7 Volume Production of Negative Ions

The existence of negative ions in a plasma was established long ago; around 1959.[26] Positive hydrogen and deuterium ions are easily extracted form a multicusp ion source. On reversing the extraction potentials, electrons and negative ions present in the source may be extracted. It was shown by Bacal et al. [27] that large densities of negative hydrogen ions exist in a hydrogen discharge or so called volume source. The possibilities of extracting high densities of negative hydrogen ions from a volume ions source for neutral beam heating applications has been shown by Holmes [28] Leung et al. [29], and Hiskes and Karo.[30]. Improvements have been made to this system since this observation, and the ratio of electrons to negative ions has been greatly reduced giving a subsequent larger negative ion current yield.[31,32]

It is generally accepted that the dominant production mechanism of negative hydrogen ions in these sources is a two step process.[33,34] The hydrogen molecule is brought to a vibrationally excited state by an energetic electron [35,36] and the ions produced by dissacociative attachment of a slow electron to this vibrationally excited molecule [37]. The processes used in the formation of the H^- in a volume ion source are explained here.

Several processes can result in the formation of Hin volume ion sources, i.e. dissociative attachment of low energy electrons to metastable molecules [38], and polar disociation of molecules by fast electrons.

Dissociative Attachment (DA) of slow thermal electrons to molecular hydrogen results in the formation of negative hydrogen ions. This process can be seen in the following equation:[38]

$$H_2 + e^- \rightarrow H_2^-\left({}^2\Pi_U\right) \rightarrow H^- + H(2p) \qquad \textit{Equation 1.2}$$

Polar dissociation by fast energetic electrons also results in the formation of negative ions:

$$H_2 + e_p \rightarrow H^- + H^+ + e^- \qquad \textit{Equation 1.3}$$

It appears that the dominant process for the production of these ions is DA of slow, low energy thermal electrons to highly vibrationally excited molecules, $H_2(v'')$.

$$e^- + H_2(v'' > 3) \rightarrow H_2^- \rightarrow H^- + H^+ \qquad \textit{Equation 1.4}$$

which requires a two stage process. Initially the ground state hydrogen molecule must be excited to a vibrationally excited state, where then the attachment of slow electrons produce a negative hydrogen ion.

This excitation to a vibrationally excited level can happen in one of two ways, the **e-V** process, where a thermal electron and a vibrationally excited level of hydrogen combine as follows:[39,40]

$$e^- + H_2(v'') \rightarrow H_2(v'' < 3) + e^- \qquad \textit{Equation 1.5}$$

The problem with this method is that the vibrational levels populated are predominantly < level 3 and from equation (3) above it is seen that the population of higher levels is required.[41]

The second method is the **E-V** process where energetic electrons excite the ground state hydrogen molecule to an electronically excited singlet state.

$$H_2(v''=0)+e_p \rightarrow e^- + H_2^*(B^1\sum u^+) \qquad \textit{Equation 1.6}$$

These electronically excited states then radiate back to a vibrationally excited state due to the Frank Condon principle, by the following equation:[38]

$$H_2^*(B^1\sum u^+) \rightarrow H_2(v'')+hv \qquad \textit{Equation 1.7}$$

There are also other methods of generating vibrationally excited states, one is the recombination of atom on the walls,

$$H^+ + H^- \rightarrow H_2(v'') \qquad \textit{Equation 1.8}$$

and the other is the Auger de-excitation of molecular ions on the walls:[42]

$$H_2(^3\Pi_u) \rightarrow H_2(v'') \qquad \textit{Equation 1.9}$$

It is generally accepted that the dominant negative hydrogen ion production mechanism is that a fast energetic electron excites a ground state hydrogen molecule to an electronically excited state, in the singlet method. This state then decays radiatively due to the Frank Condon principle and that DA of a slow thermal electron to this state will then produce a negative hydrogen ion.

There are limitations to this model, in positive ion generation, the ion is produced as a direct result of energetic electrons, and therefore the positive ion density increases as a function of the plasma temperature and density.

$$H_2 + e_f \rightarrow H_2^+ + 2e \qquad \textit{Equation 1.10}$$

However, in negative ion production this is not the case. A major loss mechanism to negative hydrogen ions is **collisional detachment (CD)** by fast electrons [43]

$$e_f + H^- \rightarrow H + 2e \qquad \textit{Equation 1.11}$$

electrons of energies greater than 3 eV can destroy the negative ion.

Therefore, although fast energetic electrons are required to produce the vibrationally excited state, they would also destroy the negative ions generated. It is for this reason that a lot of study is carried out on magnetic filtering.

1.8 Magnetic Filtering

The limitations described above in the formation of H^-have been overcome successfully by two main methods, the tandem source [44,45] and the hybrid source [46]. Both of these sources work on the concept of separating the ion source chamber into two separate regions. In the first region a hot, dense plasma is contained, typical kT_e>2 eV. In this region the excitation of vibrational levels occurs via the E-V process described above. The second region contains a cooler plasma, typical kT_e<1 eV. Here the disassociative attachment results in the production of negative ion production. The two regions are separated by a magnetic field. The first region is called the driver region and the second region, which contains the cooler plasma, is called the extraction region. The effect of the magnetic field in between is the prevention of the energetic electrons from passing into the extraction region, but the vibrationally excited levels and the cooler, slower electrons and the ions drift through [47].

The use of such filters has been proven successful on positive ion sources [48]. Ehlers et al.showed enhanced proton yield from a positive ion source by only allowing low energy electrons to drift through to the extraction region of the ion source. This resulted in a more quiescent plasma near the extraction electrode. Leung et al. [48] also showed that the filter increased the negative ion current extracted and also decreased the electron current extracted. The tandem source and the hybrid source are each described here.

1.9 The Tandem Source

The tandem source uses the principle of magnetic filtering to enhance the production of H^-

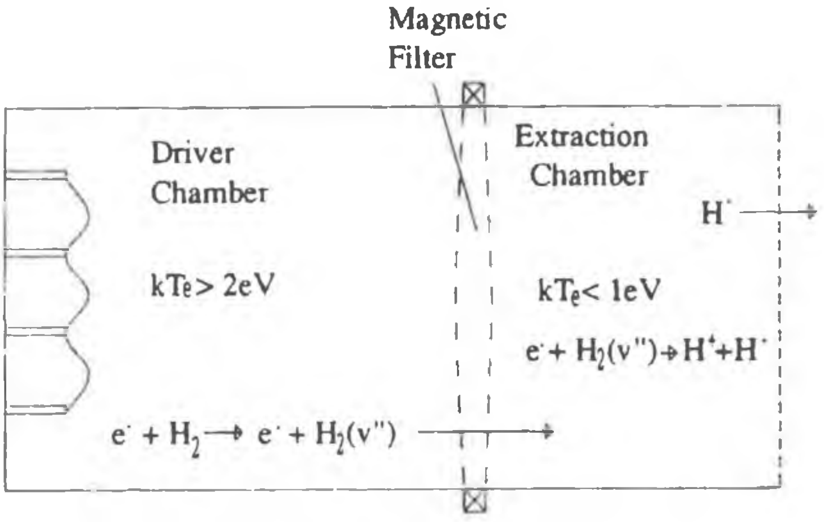

Fig. 1.4 Schematic of the Tandem Source.

The schematic of the tandem source above shows the layout of the source and the separation into the extraction and driver regions. The magnetic filter used to produce this separation can be achieved in several ways. Mullan and Graham [44] used a filter field created by breaking the geometry of a multipole field on two opposite sides of the chamber. Leung et al. produced the same effect using a rod filter, where permanent magnets were placed in rods in the chamber. The driver region is at the front of the chamber where the filaments are heated. The plasma in this region is hot and dense, with temperatures typically of kT_e>2 eV. The electron energy distribution function (EEDF) is non maxwellian with a fast electron tail as shown by Hopkins et al. [50]. In this region there are high numbers of fast hot electrons. Here the excitation of vibrational states occurs by means of the E-V process. Once these vibrationally excited states are produced they can then drift through the magnetic filter field produced into the extraction region of the chamber. Negative ions can be produced in the driver region; these too can drift through the magnetic field into the extraction region. The number of H^-produced is obviously of low density as the rate of dissociative attachment will be low due to the number of hot electrons, and also then the rate of collisional detachment will be very high. The rate of DA in this region can be as low as $1x10^{-8}$ cm^3/s in a $kT_e = 2$ eV discharge.

The extraction region contains a much cooler plasma, typical temperatures, kT_e <1 eV. The fast electrons are retained in the driver region of the chamber due to the magnetic field. Hopkins et al. have shown here that the EEDF collected in this region would have a maxwellian shape and no fast electron tail. In this region the negative ions can be produced by the dissociative attachment process of the low energy electrons to the vibrationally excited states produced in the driver region. In the cooler plasma the DA process is enhanced and can be optimised for temperature less than 1 eV, the reaction rate for DA in this region can reach a peak of $2.8x10^{8}$ cm^3/s due to the low electron temperature. This then results in an enhanced H^- production. The reaction rate for the collisional detachment rate in this region can be an order lower than that of the driver region, meaning that the H^- produced has little chance of being destroyed. It has been shown that CD is the main loss mechanism [43] in a volume ion source and hence this order of magnitude difference between the driver and the extractor can have a dramatic effect on the H production in the chamber. Leung, Bacal and Ehlers have reported increases form 2μA to 23μA by the use of a strong magnetic filter dividing the chamber.[51]

1.10 The Hybrid Source

The hybrid source also uses the concept of magnetic filtering to enhance the production mechanisms required to generate H^-.

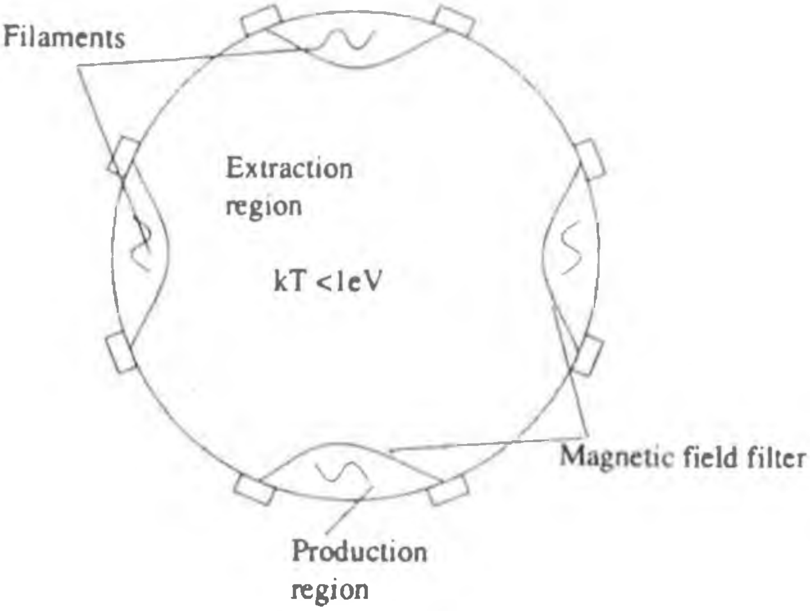

Fig. 1.5 Schematic of the Hybrid Source Configuration (extraction plane out of the paper).

The schematic above shows the chamber configuration of the hybrid source. Bacal [46] uses such a source successfully to optimise the production mechanism of H^-. In this system the chamber is not divided in two as such. The filaments are mounted inside multicusp fields achieved by mounting a series of permanent magnets with alternating poles facing the plasma. This effectively acts the same as the tandem source. The region inside the cusps, where the filaments are, is the driver region, and the main area in the centre of the chamber acts as the extraction region. The cusp fields at the wall act as the magnetic filter preventing hot, energetic electrons to drift form the production region into the extraction region. As in the tandem source, the cusp fields enhance electron confinement and therefore the plasma densities.

Hopkins et al. [51] have shown that the EEDF's collected in the regions close to the heated filaments have a fast-electron component in the distribution. On moving further into the central chamber this fast-electron component disappears. Having filtered out the hot electrons the rate of CD in the main part of the chamber will have greatly reduced, and now the main destruction mechanism is mutual neutralisation (MN) of the H^- with positive ions and associative detachment (AD) of the H^- with electrons. In the central region typical temperatures are kT_e<1 eV, Bacal [46] has reported high densities and a high proportion of H^-.

In both of the previously described sources, the same concept was used to enhance the production of the H^-. The two-stage process of H^- formation, E-V followed by DA, were separated up into two separate regions where conditions were specified and optimised for each specific reaction. The separation of the regions by the magnetic filed allowed the spatial control of the EEDF and the temperature, kT_e in the chamber. Control of the EEDF and the electron temperature can be achieved by varying the plasma parameters, gas density or discharge current, the effectiveness of the magnetic field is basically that it allows two distinct plasma regimes to co-exist in the one chamber under the same operating conditions. What is achieved is a hot, dense plasma exhibiting a non-maxwellian EEDF with a fast-electron tail, existing in the same chamber as a colder plasma exhibiting a maxwellian distribution, both plasmas however are not segregated when considering the other plasma parameters. The vibrationally excited states and the thermal electrons and ions can drift between both regions and are not distinct to either one.

The effectiveness of separating the chamber into two regions, one for each process of the production mechanism is the essence of both the hybrid and the tandem source. Control of the EEDF and the electron temperatures in two different regimes can also be achieved temporally, where the two regions are separated by time rather than space, i.e. temporal filtering. The concept of temporal filtering is explored in Chapter 4.

1.11 Filament Driven Volume Ion Sources

In the volume ion source, which is a hot cathode discharge, the filaments frequently made of tungsten act as the cathode, while the chamber walls act as the anode. The tungsten filaments are heated and biased typically between 50 and 100 V negative with respect to the anode. The electrons emitted by thermionic emission are accelerated towards the (anode) walls. The walls have permanent magnets affixed in an arrangement known as a multicusp configuration. This means that each magnet alternately faces north or south towards the inside of the chamber. It is because of this configuration that the name magnetic multicusp source originates. The result is that a magnetic field is generated which extends into the chamber near the anode surface.

It is thought that the field has the effect of confining the primary electrons, which are emitted from the filaments due to thermionic emission, in the discharge. This in effect increases the characteristic length of the source and reduces the effective anode loss area.

Buzzi et al. [53] have shown that the increase in the plasma density is due to the reflections of the primary electrons by the magnetic wall. They also showed the difference in the travel length of the primary electrons with and without the magnets affixed. Without the magnets the distance travelled by the primaries is the same as the filament to wall distance, while the distance is increased quite substantially by the magnets. The background gas becomes ionised as these fast electrons are accelerated towards the anode. For efficient operation the mean free path of the primaries must be comparable to the characteristic length of the source or else the electrons may be lost to the walls. It may be concluded that the effective increase in the source length caused by the magnetic confinement adds considerably to the efficient operations of the source.

1.12 RF Driven Volume Ion Sources

RF driven discharge can operate in one of two modes, capacitive or inductive. The mode of interest for this work is an inductive discharge where the discharge is electrodeless, i.e. the power is coupled to the discharge via a helically wound antenna. The flow of RF current through the antenna gives rise to a time-varying electromagnetic field in the area surrounding the antenna. This altering electromagnetic field then results in the ionisation of the surrounding gas forming the discharge and also gives rise to an induced current in the plasma, which heats the discharge. The method of operation is similar to that of a transformer. A number of different configurations are utilised, some sources use an internal antenna housed in a quartz tube in the discharge while others use an external antenna to the source.

1.13 Outline of Proposed Research

Filament driven negative ion sources have been investigated extensively as a means of enhanced production of negative hydrogen ions for use in the application of negative ions for NBI systems for future TOKAMAK's. Filaments have a limited operational lifetime and for high power continuous operation in a radiation environment, as required for future negative ion sources, a source with reliable and sustainable long life is required. RF is an obvious choice for such a source. However, RF driven discharges have a higher electron temperature and therefore a high optimum operating pressure. The temporal filtering of such a source is of much interest as large enhancements may be expected at the low operating pressures required. The concept of a temporally filtered filament driven volume ion source for low pressure, high power operation has been investigated in the past [54]. Negative ion densities are seen to increase dramatically in the post-discharge of low-pressure plasma.

The purpose of this thesis is to present an experimental study of low-pressure filament driven (DC) and RF inductively coupled plasma (ICP) discharges and to compare the operational efficiency of both sources in the production of negative hydrogen ions. Both sources are temporally modulated to determine the negative ion densities in the afterglow. The diagnostics utilised in this work include a Langmuir probe and a laser photodetachment technique.

An in-depth characterisation of both the RF and DC systems was carried out, operating in both continuous and pulsed modes, these results are presented in Chapter 4. Radial and fixed position measurements were taken at various powers and pressures and the effect of the application of an applied external magnetic filed was also determined with respect to improving plasma density.

The negative ion densities in the continuous and pulsed DC discharge were determined by the use of the laser photodetachment technique and compared to results measured in the afterglow of a pulsed RF ICP discharge. The production and destruction mechanisms for negative ion generation in the afterglow of an RF ICP discharge was modelled to interpret the measured data. These results are presented in Chapter 5.

In an effort to increase the production of negative ions in both volume ion sources the effect of addition of argon to a hydrogen discharge was investigated in Chapter 6. Previous reports have indicated an increase in negative ion densities in an argon seeded discharge.[55]

Collaborative work performed on other systems is also presented in this chapter. An enhancement in negative ion densities was recorded in the discharges with an admixture of argon and a possible explanation for this increase given.

Finally, an overall discussion and conclusion of the comparative results from this project are made. There is still much research to be carried out in this field and some proposed areas for improving understanding in these sources suggested.

References:

[1] Boilson, D
"Automation of a multicusp Volume Ion Source DENISE"
M.Sc. Thesis, 1997.

[2] Halliday , Resnick,
"Modern Physics Chapters for Physics", Third edition

[3] Coburn, J.W.,
IEEE Trans. Plasma. Sci. 19(6), 1991, 1048-1062

[4] Shothet, J.L.
IEEE Trans. Plasma. Sci. 19(5), 1991, 725-733

[5] Graves, D.B.
IEEE Trans. Plasma. Sci. 22(1), 1994, 31-42

[6] Chapman, B.
Glow Discharge Processes, Wiley New York, 1980.

[7] Pearton, S.J. and Hobson, W.S.
Journal of Applied Physics, 66(10), p5009 -5017, 1989

[8] Van den Hoek, W.G.M., De Vries, L.A.M and Heijman, M.G.J.
J. Vac. Sci. Technol. B (3), P647 -651, 1987.

[9] Pearton, S.J. and Hobson, W.S.
Journal of Applied Physics, 66(10), p5018 -5025, 1989

[10] Kersten, H., Snijkers, R.J.M.M., Schulze, J., Kroesen, G.M.W., Deutsch, H., and De Hoog, F.J.
Appl. Phys. Lett. 64 (12), p1496 - 1498, 1994.

[11] Lin, Y. and Overzet, L.J.,
Appl. Phys. Lett. 62 (7), p675- 677, 1993.

[12] Hunt, S.E.
"Fission, Fusion and the energy crisis"
2nd edition, Pergamon Press, Oxford, 1980.

[13] Bickerton, R.J.
Physics Bulletin, 39, 1988.

[14] Fielding, P.J.
"Plasma Physics and Nuclear Fusion Research"
Academic Press, London, 1981.

[15] Van Os, R.
"Negative Ion Sourcery" PhD Thesis 1989

[16] Hemsworth, R.S.
"Plasma Physics and Nuclear Fusion Research", Academic Press. London 1981.

[17] Van Os, R.
"Negative Ion Sourcery" PhD Thesis 1989.

[18] Hemsworth, R.S.
"Conceptual Design of an ITER (EDA) Injector", Proceedings JDC 2/93, JET, 28-30 Sept. 1993

[19] Van Os, R., Heeren , R.M.A. and Van Amersfoort, P.W.
Appl. Phys. Letts, 51(19), p1495, 1987.

[20] Hiskes, J.R., Karo, A, and Gardner, M.
Journal of Appl,. Phys, 47 (9), p3888, 1976

[21] Kaye, G.W.C. and Laby, T.H.
Tables of Physical and Chemical constants,
14th edition, Longman, London and New York, 1973.

[22] Belchenko, Y.I., and Dudnikov, V.G.
4th European Workshop on the Production and Application of Light Negative Ions, March 26-28, 1991.

[23] Hagena, O.F., and Henkes, P.R.
4th Int Symp. on Production and Neutralization of Negative Ions and Beams, Brookhaven, NY, 1986

[24] Peterson, J.R.
4th Int Symp. on Production and Neutralization of Negative Ions and Beams, Brookhaven, NY, 1986

[25] Okumura, Y
4th Int Symp. on Production and Neutralization of Negative Ions and Beams, Brookhaven, NY, 1986

[26] Moak, C.D., Banta, H.E., Thurston, J.N., Johnson, J.W.,King, R.F.
Rev. Sci. Instrum. 30, 694 (1959)

[27] Bacal, M. and Hamilton, G.
Phys. Rev. Lett. 42, p1538, 1979.

[28] Holmes, A.J.T., Green T.S. and Newman, A.F.
Rev. of Sci. Instrum, 58(8), p1369, 1987.

[29] Leung, K.N., Ehlers, K.W.and Pyle, R.V.
Rev. of Sci. Instrum., 56(3) March 1985.

[30] Hiskes, J.R. and Karo, A.M.
J. Appl. Phys, 56, 1927 (1984).

[31] Ehlers, K.W., Gravin, B.F., Hubbard, E.L.
Nucl. Instrum. Methods 22, 87 (1963)

[32] Belchenko, Y.I., Dimov, G.I.,Dudnikov, V.G.
Novosibirsk Report No. 66-72 (1972)

[33] Kuchinskii, V.V., Mishakov, V.G., Tibilov, A.S., Shutkin, A.M.,
Opt. Spectrosc. 39, 598 (1975)

[34] Allan, M., Wong, S.F.,
Phys. Rev. Lett. 41, 1791 (1978)

[35] Gorse, C., Capitelli, M., Bretagne, J.,Bacal, M.,
Chem. Phys. 93, 1 (1985)

[36] Hiskes, J.R., Karo, A.M., Willman, P.A.
J. Vac. Sci. Technol. A3, 1229 (1985)

[37] Hiskes, J.R.
At. Mol. Phys. 19, 59 (1987)

[38] Eenhuistra, P.J., et al.
Journal of Applied Physics, 69, (1), p85, 1990

[39] Hiskes, J.R, et al.
Journal of Applied Physics, 53 (5), p3409, 1982

[40] Bacal, M.
Phys. Scr, T2/2, P467, 1982

[41] Eenhuistra, P.J. et al.
Physical Review A, 40 (7), p3613, 1989

[42] Hiskes, J.R.
"4th International Symposium on the Production and Neutralisation of Negative Ions and Beams". Brookhaven, New York, 1986.

[43] Bacal, M
Nuclear Instruments and Methods in Physics Research, B37/38, p28-32, 1989.

[44] Mullan, A.A, and Graham, W.G.
Review of Scientific Instruments, 61 (1), p451, 1990

[45] Holmes, A.J.T., et al.
Review of Scientific Instruments, 53 (2), p223, 1987.

[46] Bacal, M., Bruneteau, A.M., and Nachman, M.
Journal of Applied Physics, 55(1), p15, 1984

[47] Holmes, A.J.T.
Review of Scientific Instruments, 53 (10), p1517, 1982.

[48] Ehlers, K.W. and Leung, K.N.
Review of Scientific Instruments, 52 (10), p1452, 1981

[49] Leung, K.N., Ehlers,K.W., Bacal, M
Review of Scientific Instruments, 54 (1), p54, 1983

[50] Hopkins, M.B. and Graham, W.
Journal of Physics D, Appl, Phys, 20, p838, 1987.

[51] Leung, K.N. et al.
Review of Scientific Instruments, 54, p56, 1983.

[52] Hopkins, M.B. et al.
Journal of Physics D, Appl, Phys, 24, p268, 1991.

[53] Buzzi, J.M., Snow, J.,Hirshfield J.L.
Physics Letters vol54 no.4 p344 1975

[54] Mellon, K.N.
PhD Thesis, Dublin City University 1991.

[55] Leung K, Ehlers, K, Pyle R,
Rev. Sci. Instrum. 56, p2097, 1985

Chapter Two

Basic Plasma Theory

2.0 Introduction

This chapter will go through the basic theory of plasmas and provide an understanding of the processes within the plasma and the important characteristic behaviour in the discharge. An outline of the operation of RF inductively coupled plasmas; their heating mechanisms and modes of operation are also discussed.

2.1 Definition of a Plasma

Although a large percentage of the universe, said to be ~99% [1, 2], is quoted as being in the plasma state, the Earth is one small corner of the universe where plasma state is very rare. The reason for this is explained by the Saha equation given below:

$$\frac{n_i}{n_n} = 2.4 \times 10^{21} \frac{T^{3/2}}{n_i} e^{\frac{U_i}{kT}} \qquad \textit{Equation 2.1}$$

this equation dictates the amount of ionisation to expect in a gas in thermal equilibrium. where n_n is the gas density, U_i is the ionisation potential of the gas, T is the temperature and k the Boltzmann constant. A plasma is then specifically defined as a quasineutral gas of charged and neutral particles which exhibit collective behaviour.

Quasineutrality is the term used to imply that the density of the positive charges is approximately equal to that of the negative charges. Since both type charges coexist in the gas, coulombic forces exist between the particles. Elements of force exerted on a particle will effect not only the immediate particles in the immediate field but other particles further away. This is the condition of collective behaviour, where motions depend not only on a local region but also on regions further away.

Within a plasma there exists a range of particles with different velocities and therefore different energies. The distribution of the velocities is statistically said to be a Maxwellian distribution which is given by the following equation.

$$f(v) = A\exp\left[\frac{-mv^2}{2kT}\right]$$

Equation 2.2

where, A is a constant defined by the following equation:

$$A = n\left(\frac{m}{2\pi kT}\right)^{\frac{1}{2}}$$

Equation 2.3

and $f\ dv$ is the number of particles per m^3 with velocities ranging between v and $v + dv$. The density of the particles is given as the sum over all the available velocities,

$$n = \int_{-\infty}^{\infty} f(v)dv$$

Equation 2.4

The temperature then is the term used to characterise the energy of the particles in a maxwellian distribution. The average energy of the particles in the plasma can then be determined from equations x and x above.

$$E_{av} = \frac{\int_{-\infty}^{\infty} 1/2\, mv^2 f(v)dv}{\int_{-\infty}^{\infty} f(vdv)}$$

Equation 2.5

the average energy in the one-dimension equals $\frac{1}{2}kT$, for three dimensions this is extended giving an average energy value equal to $\frac{3}{2}kT$. As the temperature and energy are closely related the temperature in plasmas is is often given "somewhat casually" in electron-volts, eV.

Having seen that there are different velocity distributions in the plasma it must also be noted that there are also different temperatures. The electrons and the ions can have different temperatures. The electrons absorb energy from the field generating them but cannot share this energy efficiently with the heavier particles. When a fast electron collides with a slow atom in an elastic collision, only a small part of the electron energy is transferred to the atom. This makes heat conduction from the electrons to the ions or neutrals very poor. The electrons then remain hot while the ions and neutrals remain roughly at room temperature. This is one of the main advantages of using plasmas as this non-equilibrium of temperature leads to the fact that high temperature chemistry can happen at a low physical temperature.

2.2 Plasma Parameters

The plasma parameters are attributes, which allow a specific discharge to be characterised and compared with other discharges. These characteristics arise from the interacting charged and uncharged particles which make up the plasma. A plasma is said to be quasi-neutral, i.e. it is assumed that there are equal numbers of positively- and negatively-charged particles. Because of this quasi-neutrality, the discharge is also said to be field-free. This concept is best explained by use of Debye shielding, which is introduced in the following section. The most important plasma parameters, which define the discharge state, are the electron and ion densities, as it is the presence of these particles which make the discharge.

2.3 Debye Shielding

A fundamental characteristic of the behaviour of a plasma is its ability to shield out electric potentials that are applied to it. When a charged conductor is placed inside a plasma, it exerts an attractive and a repulsive force on oppositely and like charged particles, respectively. The oppositely charged particles generate a region around the conductor which cancels out the electric field around the conductor, preventing the conductor field penetrating into the quasi-neutral plasma. This shielding is known as Debye shielding and the depth of the imbalance around the conductor is known as the Debye length. The approximate thickness of the charge cloud, the Debye length, is computed from a solution to Poisson's equation,

$$\nabla^2\Phi = -\frac{e}{\varepsilon_0}(n_i - n_e), \qquad \textit{Equation 2.6}$$

First, it is possible to determine the electrostatic potential Φ, that is due to the conductor charge, Q. Using Boltzmann's equation [1],

$$n(E) = n_0 \exp\left(\frac{-E}{kT}\right) \qquad \textit{Equation 2.7}$$

where k is Boltzmann's constant , the potential, Φ, that is produced by the conductor charge, Q, that attracts the electrons and repels the ions can be described, as shown below,

$$n_e = n_0 \exp\left(\frac{e\Phi}{kT}\right) \qquad \textit{Equation 2.8}$$

$$n_i = n_0 \exp\left(-\frac{e\Phi}{kT}\right), \qquad \textit{Equation 2.9}$$

the charge density, ρ_e, can now be given by,

$$\rho_e = e(n_i - n_e) = -2en_0 \sinh\left(\frac{e\Phi}{kT}\right), \qquad \textit{Equation 2.10}$$

where, $\sinh(x) = \frac{1}{2}(e^x - e^{-x})$.

Knowing from Poisson's equation that,

$$\nabla.E = \rho_e/\varepsilon_0 \qquad \text{and} \qquad E = -\nabla\Phi, \qquad \textit{Equation 2.11}$$

following through gives,

$$\nabla^2\Phi = -\frac{\rho_e}{\varepsilon_0}, \qquad \textit{Equation 2.12}$$

substituting this result back into *Equation 2.10* gives,

$$\nabla^2\Phi = \frac{2n_0 e}{\varepsilon_0}\sinh\left(\frac{e\Phi}{kT}\right), \qquad \textit{Equation 2.13}$$

near the edge of the shielding cloud, and beyond, the electrostatic energy, $e\Phi$, associated with the charge from the conductor, Q, is much less than the electron thermal energy, kT. Approximating $\sinh(e\Phi/kT) \cong e\Phi/kT$, allows *Equation 2.13*, to become,

$$\nabla^2\Phi = \frac{2}{\lambda_D^2}\Phi, \qquad \textit{Equation 2.14}$$

λ_D, is defined as the Debye length given by,

$$\lambda_D = \left[\frac{\varepsilon_0 kT_e}{e^2 n_e}\right]^{1/2} \qquad \textit{Equation 2.15}$$

From the above equation it can be seen that as the density is increased, λ_D decreases. This is as expected since each layer of plasma would contain more electrons. As kT_e increases, then so does λ_D. Without thermal agitation, the charge cloud would collapse into an infinitely thin layer. It is the electron temperature that is used to define λ_D, as the electrons being so much lighter than the ions are more mobile, and it is the electrons that then generally do the shielding by moving to create a surplus or deficit of negative charge. The plasma approximation demands that the number of charged particles within a Debye sphere (a sphere of one Debye length in radius) must be substantially greater than one:

$$N_D >> 1$$

Also, to preserve the quasi-neutrality property of the plasma, the plasma size must be much greater than the Debye sphere:

$$L >> \lambda_D.$$

When the plasma is not subjected to external forces, it is madeup of the interactions of the charged particles inside moving about due to their own thermal velocities. When a force is applied or the plasma is perturbed in some way the plasma tries to compensate and preserve its quasi-neutrality and field free conditions. The rate that a plasma can react to these changes is related to the plasma frequency, which is described next.

2.4 Plasma Frequency

If a plasma is perturbed, the separation of positive ions and negative electrons will generate and electric field, E. This electric field will give rise to a restoring force, F_r, which works at returning the particles to their equilibrium position. In a collisionless regime, this force, F_r, is given by

$$F_r = m_e \frac{d^2 x}{dt^2} = -eE = -\frac{n_e e^2 x}{\varepsilon_0} \qquad \textit{Equation 2.16}$$

where, m_e, is the mass of the electron, e, is the electronic charge, ε_0 is the permittivity of free space and x, is the displacement of the electrons.

When the electron reaches its original position it has a finite velocity and continues past its position until its kinetic energy goes to zero, generating a new electric field, and hence a new restoring force. Thus the electron oscillates around its position. The frequency of this oscillation can be deduced by substituting the equation for simple harmonic motion into *Equation 2.16*, deriving the electron-plasma frequency as

$$\omega_p = \left(\frac{n_e e^2}{\varepsilon_0 m_e} \right)^{\frac{1}{2}} . \qquad \text{Equation 2.17}$$

Substituting the electron density and mass for the ion density and mass, generates a similar equation for the ion-plasma frequency. As the ion mass is much greater than the electron mass, the electron-plasma frequency is greater than the ion-plasma frequency, and hence it is usually the electron-plasma frequency that is quoted for a particular plasma.

2.5 Processes within a Plasma

When a plasma has been generated by whatever means, it must sustain itself until the power is removed. Since the plasma is made up of many different particles, positively and negatively charged particles and neutrals, collisions are then going to occur between them, many get lost to the walls and some recombine. An outline of some of the processes that may occur in the plasma are given here.

2.5.1 Collisions

A number of different collisions take place within the plasma, both elastic and inelastic collisions, where the particles undergo different processes, with each of the processes having a different effect and frequency in the plasma. To establish the frequency at which these collisions occur, we return to the concept of the mean free path.

As mentioned earlier, there are a number of particle velocities within the discharge, the velocity distribution. Therefore there is also a distribution of free path lengths, which is the distance that a particle travels before colliding. This is the mean free path and is given by:

$$\lambda_m = \sum_n \frac{1}{N_n \sigma_n} \qquad \text{Equation 2.18}$$

where N_n is the number of particles of species n per m^3, and σ_n is the cross-sectional area for collisions between electrons and particles of species, n. The time, therefore, between the collisions for a particle travelling at a velocity u can be evaluated to be

$$\tau = \frac{\lambda_m}{u} \qquad \text{Equation 2.19}$$

the frequency, ν, between the collisions is then the reciprocal of the mean time, τ.

If the velocity distribution governing the electrons is said to be maxwellian then the total collision frequency must be summed over all the velocities and therefore is given as

$$\nu = N_n \overline{\sigma u} \qquad \text{Equation 2.20}$$

The types of collisions that can occur include electron-impact collisions with neutral atoms, ion-neutral collisions, metastable collisions and many others. The outcome of these collisions can result in ionisation, recombination, excitation or relaxation of the particles. By combining these production and loss mechanisms, the plasma is maintained.

2.5.2 Ionisation

Electron impact ionisation is the most important mechanism by which the plasmas studied here are maintained. A free electron collides with a neutral atom removing an electron, producing a charged particle and two electrons. These two electrons can be accelerated within the plasma by the electric field or with the oscillating sheath if an RF plasma and then acquire sufficient energy to go on to ionise more neutrals in collisions. The minimum energy required to ionise a neutral is called the ionisation energy.

2.5.3 Enhanced Ionisation

In this process electrons can attain ionising potential in weak electric fields. If an electron undergoes an elastic collision at the appropriate time with respect to the phase of the applied field it may increase its energy. The electron collides with a neutral, reversing its direction at the same time as the field changes direction. By this increase in energy an RF plasma can be sustained for much smaller electric fields than for DC plasmas.

2.5.4 *Excitation and Relaxation*

Excitation is the process where an electron, bombarding a neutral, transfers its energy to a bound electron in the atom resulting in the jumping of that bound electron to a higher state in the atom. Relaxation is the opposite process where the excited electron drops back from the higher level to a lower energy level and emits a photon of light equal to the difference between the two energy levels. Optical emission spectroscopy uses this emission of light to detect the presence of various atoms.

The three main electron loss mechanisms in RF plasmas are recombination, diffusion and attachment [3, 4, 5]. In the following sections theses three mechanisms are described individually and their relevance to the plasmas studied in this thesis examined.

2.5.5 *Recombination*

Recombination occurs when an ion and electron collide, particularly at relatively low velocities and combine to form a neutral atom. Due to energy and momentum conservation requirements a third body is required in the recombination process. This third body can be a gas atom, the chamber wall, another electron or even an emitted photon. If the third body is an emitted photon, the process is called radiative recombination. If the third body is another particle, this recombination process is known as three-body recombination. The process of recombination can also occur when a negative and a positive ion collide, exchanging an electron and forming a neutral atom. The electron loss rate for a quasi neutral plasma is given by

$$\frac{dn}{dt} = -\alpha n^2 \qquad \textit{Equation 2.21}$$

where, α, is known as the recombination coefficient and has units cm^3/s. The solution is found to be

$$\frac{1}{n} = \frac{1}{n_0} + \alpha t \qquad \textit{Equation 2.22}$$

where n_0 is the initial density distribution. After the density has fallen far below its initial value, it falls of in a reciprocal manner as is shown in the following equation.

$$n \propto \frac{1}{\alpha t} \qquad \textit{Equation 2.23}$$

2.5.6 Diffusion

When the density of charged particles in a plasma is relatively low, the differently charged particles can diffuse independently of each other. This sort of diffusion is known as free diffusion. The electrons being lighter than the ions, have a higher mobility and therefore diffuse more quickly than the ions. If however, the charged particles densities are not so low, a space charge is generated as a result of the separation of the differently charged particles, resulting in a field called the ambipolar field. This field then prevents the further departure from charge neutrality. The field results in slowing down the fast moving electrons and speeding up the slower moving ions. The transition from free to ambipolar diffusion is gradual.

Ambipolar diffusion cannot exist when the number of neutral particles is so low that the collisions between ions and electrons exceed the collisions with the neutrals, i.e. when the ionisation rate is high. Hence there are two different transitions that separate the three different regimes of diffusion. This is illustrated in Fig. 2.1 below.[4]

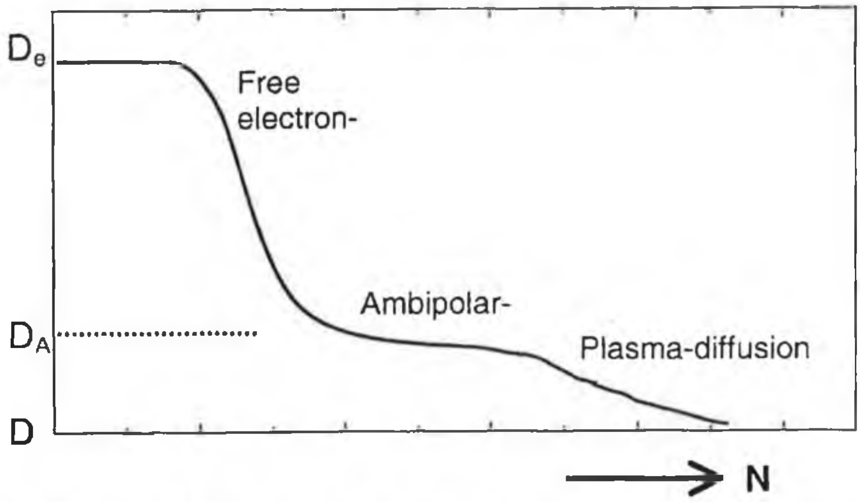

Fig. 2.1 **Schematic Representation of Diffusion Regimes in a Plasma.**

Densities decay exponentially in diffusion dominated discharges. The different loss processes can be distinguished between by observing the spatial dependence of the electron densities. In the diffusion process, the spatial distribution of the electron density results in a maximum in the centre of the discharge, while in the recombination and attachment processes a uniform density profile results. [5]

In a steady state plasma both electrons and ions must diffuse at the same rate, with an effective diffusion co-efficient given by:

$$D_a = D_i\left(1+\frac{T_e}{T_i}\right) \qquad \textit{Equation 2.24}$$

where D_i is the diffusion co-efficient for the ions alone and D_a is the ambipolar diffusion co-efficient.

2.5.7 *Attachment*

Another important loss mechanism in electronegative plasmas is electron attachment. In this process the electronegative atoms or molecules capture electrons, resulting in the formation of negative ions. The electron loss rate for this process is given by the following equation:

$$\frac{dn_e}{dt} = -v_a n_e = -hv_e n_e \qquad \text{Equation 2.25}$$

where, v_a is the collision frequency for attachment, v_e is the electron-neutral collision frequency and h is the co-efficient for attachment. Attachment resulting in negative ion formation may occur by different processes such as, radiative attachment, dissociative attachment and three-body attachment, similar to the recombination processes mentioned earlier. [5]

2.6 Radio Frequency (RF) Inductively Coupled Plasmas

The radio frequency inductively coupled plasma (ICP) is an electrodeless type of discharge in which the RF power is coupled to the plasma by means of an induction coil which acts like the primary coil in a transformer and the plasma is analogous to the secondary coil in the transformer. For this reason these plasmas are often referred to as transformer coupled plasmas (TCP's). The discharge sources currently being studied utilize a number of different coil configurations including the planer coil [6] and the extended coil. ICP's operate at frequencies below the self resonant frequency of the coil typically at 13.56 MHz where the inequality $\omega<\omega_p$ holds true in the electron density and temperature range in which the source is generally operated in (ω_p is the plasma frequency and ω is the RF driving frequency).

Radio frequency inductive discharges offer advantages over capacitive RF discharges. The ICP is capable of achieving high plasma densities at lower pressure and lower power. In an ICP the power is coupled through a dielectric window so the plasma is not in contact with a powered electrode. Since the power transfer in the inductive discharge is non-capacitive, low voltages are achieved across all plasma sheaths and the ion acceleration energy is low. The ion energy can be controlled in processing applications by placing the substrate on an electrode, which can be biased by a separate radio frequency power source. This enables the independent control of ion flux and ion bombardment energies [7]. This is important since a number of modern industrial plasma processes require a high ion flux density which is uniform over a large area. Therefore it is necessary to have a collisionless dense plasma ($n_e > 10^{11} cm^{-3}$) [8] . This is not possible with the capacitive systems currently being used in the industry.

The ICP source under consideration in this project is of the internal antenna type. This type of geometry, while not widely used in material processing applications, is under consideration as for ion sources in fusion experiments [9] and also for lighting applications [10].

2.6.1 The Inductively Coupled Plasma (ICP)

The ICP works on the basis that an azimuthal electric field is induced in the chamber according to Faraday's law, due to the time varying magnetic field generated by the radio frequency coil current.

$$\nabla \times \mathbf{E} = -\frac{d\mathbf{B}}{dt} \qquad \textit{Equation 2.26}$$

This azimuthal electric field penetrates the plasma falling off over a characteristic length δ called the skin depth. This phenomenon arises due to the generation of eddy currents which occur whenever an alternating current flows through a conductor, these eddy currents, by Lenz's principle, act to decrease the magnitude of E. Within this distance from the surface of the plasma, power is transferred from the electric field to the electrons by collisional (ohmic) heating and by a collisionless mechanism whereby the electrons gain energy by interacting with the electric field. Ampere's law determines the electric current in the plasma

$$\nabla \times \mathbf{B} = \mu_0 J + \mu_0 \varepsilon_0 \frac{d\mathbf{E}}{\mathrm{dt}} \qquad \textit{Equation 2.27}$$

If the plasma frequency is large compared to the driving frequency the displacement current can be neglected in Ampere's law [11], giving;

$$\nabla \times \mathbf{B} = \mu_0 J \qquad \text{Equation 2.28}$$

and

$$J(r) = \mu_0^{-1}\left(\frac{d\mathbf{B}_z(r)}{dr} - \frac{d\mathbf{B}_r(r)}{dz}\right) \qquad \text{Equation 2.29}$$

where j_θ is the azimuthal current density. The power dissipated in the plasma is given by

$$P(r) = E_\theta(r) J_\theta(r) \cos\phi_{EJ} \qquad \text{Equation 2.30}$$

where ϕ_{EJ} is the phase difference between E_θ and J_θ.

Power is supplied to the ICP from an RF power supply generally the output impedance of the source is 50 Ω. The maximum power theorem states that for maximum power transfer to occur in an AC circuit the load impedance must be equal to the complex conjugate of the source impedance. Since the antenna has an inductive and resistive component to its impedance and the source has a purely resistive impedance, a matching network must be added to the radio frequency supply in order to achieve maximum power transfer from the RF source to the antenna. The RF power supplied to the antenna can be expressed as

$$P_{ant} = VI\cos\phi_a \qquad \text{Equation 2.31}$$

Where V and I are the antenna rms current and voltage respectively andϕ_a is the phase difference between them.

The electron inertia inductance follows from the plasma conductivity formula [12]

$$\sigma = \frac{e^2 n_e}{m(\upsilon - j\omega)}$$ Equation 2.32

where e is the electronic charge m is the electron mass v is the electron collision frequency, L_e is the imaginary part of the plasma impedance and is related to the plasma resistance by

$$L_e = \frac{j\omega R_2}{\upsilon}$$ Equation 2.33

2.6.2 Heating Mechanisms in an ICP

In a cold plasma, i.e. where the electron thermal motion is negligible, the coupling between the current density J and the RF electric field E is local and given by Ohm's law J=σE. This is known as the normal skin effect and in such a case energy transfer to the electrons in the plasma can only occur by ohmic heating. This heating mechanism results from electron neutral collisions which breaks the regularity of the motion of theelectrons leading to a net gain in the energy of the electrons. However if the electron neutral collision frequency is much less than the RF period then the plasma is cold and collisionless. In this case an electron will sample the electric field at one location in space and since the field has a harmonic time variation it averages to zero and any energy gained in one half of the RF cycle will be lost in the other half. Thus there will be no net energy gain for the electrons. In the case where the thermal motion of the electrons is significant, i.e. if an electron can traverse the skin depth in a time less than an RF period, the electron samples the field along some trajectory over which the field will, in general, not average to zero. Electrons may therefore gain energy from the electric field. This power absorption mechanism is known as the *warm plasma effect.* A direct consequence of the warm plasma effect is that the electric field at one point in the plasma can affect the current at all other points and at all other times later in the plasma. Therefore the local relation J=σE(r) dose not apply and instead the relation is non local and given by:

$$J = \int_r \int_t \Sigma(r) E(r,t) dr dt$$ Equation 2.34

where $\sum(r)$ is the spatially distributed conductivity. The RF current diffusion due to the thermal motion of the electrons is responsible for the anomalous skin effect [13].

2.6.3 Operation Modes in an ICP

When a radio frequency current passes through the induction coil of an ICP, the current, by Faraday's law, induces an oscillating electric field which is capable of maintaining the discharge in the metal chamber. The power deposition and heating mechanisms relating to this model are described in section 2.6.2. But in practical plasma chambers a large RF potential difference (several kilovolts) exists, between the ends of the induction coil and between the adjoining loops of the coil in the case of multi-turn coil, in order to drive the RF current required to maintain the discharge. This potential difference gives rise to electrostatic fields in addition to the induced electric field, the electrostatic fields allow for the possibility capacitive coupling mechanism which could also sustain the discharge.

The two power coupling mechanisms always coexist in practical ICP chambers although it is possible to limit the effect of capacitive coupling by placing a Faraday shield between the antenna and the dielectric window [14]. The two power coupling mechanisms are responsible for the operation of the discharge in two distinct modes [15], a low power mode, in which capacitive coupling dominates, generally referred to as the E mode and a high power mode in which inductive coupling dominates. This mode is referred to as the H mode. The E mode is characterized by a low luminosity and a low electron density (10^8-10^{10} cm^{-3}). A high luminosity and a high electron density (10^{11}-10^{12} cm^{-3}) characterize the H mode. It is generally found that, as the RF power is increased from zero, the gas breakdown to an E mode discharge occurs at a well defined, pressure dependent point. As the power is increased further the discharge changes abruptly, again at a well defined, pressure dependent point, to the H mode regime. Reducing the power will cause the reverse transition (from H to E mode) to take place although generally not at the same power as the E to H mode transition.

2.7 Summary

The basic theory of plasma has been reviewed. Various processes within the plasma have also been highlighted for the benefit of understanding the results presentedin Chapters 4 –

6. The theory of RF ICP has been discussed with respect to the operation modes and heating mechanisms in the discharge.

References

[1] Chen, F.F.,
Introduction to Plasma Physics and Controlled Fusion.
Vol. 1, Plasma Physics, 2nd Edition, Plenum Press, New York, 1990.

[2] Elizer, Y. and Elizer, S.
The 4th State of Matter.
I.O.P. Publishing, England, 1989.

[3] Chapman, B.A.,
Glow Discharge Processes, New York, Wiley, 1980

[4] Von Engel, A.,
Ionised Gases, AIP Press, New York, 1994

[5] Cherrington, B.E.
Gaseous Electronics and Gas Lasers, Pergamon Press, London, 1979

[6] J. Hopwood.
Plasma Sources Sci.Technol **3** 460 1994

[7] M.A. Lieberman and A. J. Lichtenberg,
Principles of Plasma Discharges and Material Processing
(Wiley New York, 1994).

[8] J. Hopwoop *et al*
J.Vac.Sci.Technol A **11** 152

[9] McNeeley, P, Boilson, D, Curran N.,Vender, D. Hopkins, M.
Rev. Sci. Instrum., 69 (2)II, p983, 1998.

[10] M. A. Lieberman and V. A. Godyak,
IEEE Transactions on Plasma Sci. Report No. UCB/ERL M97/65 (1997).

[11] I.M.El-Fayoumi and I.R. Jones
Plasma Sources Sci.Technol 7 162 1998

[12] M.M Turner
Plasma Sources Sci.Technol **5** 159, 1996

[13] M.J. Kofoid
J. Phys.Fluids. **12** 1290 1969

[14] J.A. Meyer, R.Mau , A.E. Wendt
J.Appl.Phys.**79** 1298 1996

[15] K Susuki *et al*
Plasma Sources Sci.Technol 7 **13** 1998

Chapter Three

Diagnostic Tools

3.0 Introduction

The purpose of this chapter is to describe the experimental system used, the Deuterium Negative Ion Source Experiment (DENISE). Two different modes of operation were employed, a DC filament driven discharge and an RF inductively coupled discharge. Both system set-ups are described here. The different diagnostic tools used in the course of this work are also introduced. Each diagnostic is introduced, its theory of operation and purpose to this work explained in detail. The diagnostics used included a Langmuir probe and a fast injection probe; both used to determine various plasma parameters and electron energy distribution functions (EEDF's). A laser photodetachment technique is used to determine negative ion densities. Each diagnostic has its own specific theory, which is explained in detail in this chapter.

3.1 The DENISE Experimental System

A photograph of the DENISE system is shown below in Fig. 3.1. The main elements of the DENISE experimental system consist of an ion source body, a large vacuum chamber (base pressure 10^{-5} mbar provided by turbo pumps) which houses the extraction region and an attached collector region, the Faraday cup. The original apparatus [1] was modified so as to facilitate easier access to both the ion source and the extraction region for diagnostic purposes. For the experimental work discussed in this thesis, the region of interest is focussed mainly on the volume ion source. The DENISE system is PC interfaced to allow automated control and monitoring of the pumping system, the gas and water flow and the power. The automated system is set-up so as to facilitate both manual and computer control of the parameters, and is run with watchdog lines to maintain safety.

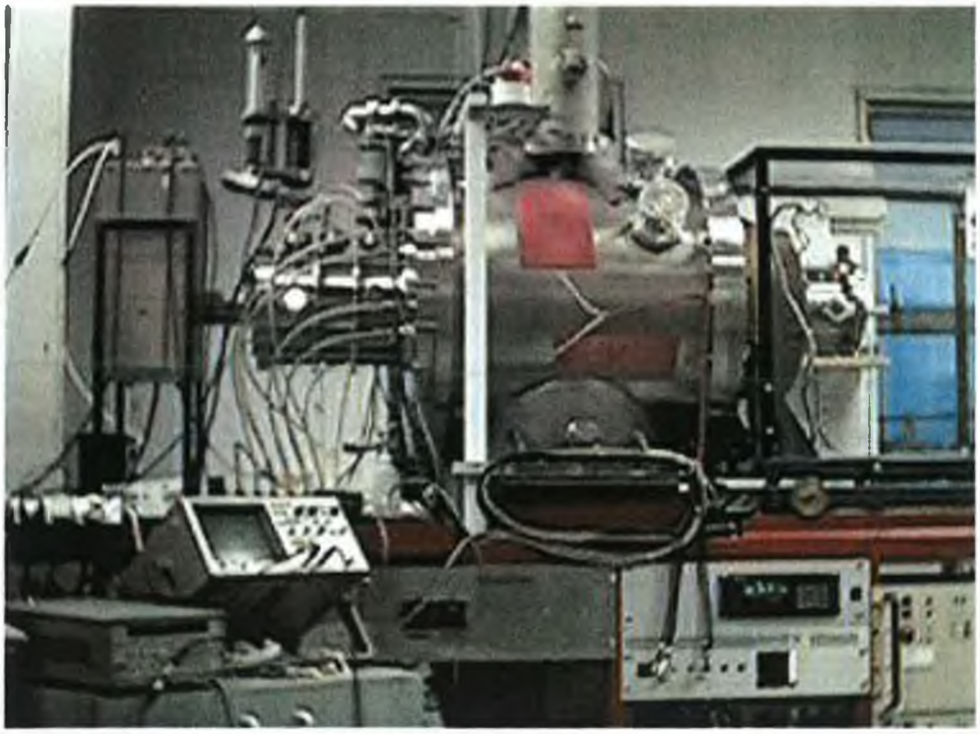

Fig. 3.1 **The DEuterium Negative Ion Source Experiment (DENISE).**

3.2 The Volume Ion Source

The new ion source designed for the DENISE system is externally modified from the original source [2]. The source body was built by Caburn-MDC. It is a water-cooled double-walled cylindrical vacuum chamber, of diameter 20.0 cm and length of 31.2 cm. There are three probe ports located on top of the chamber. Four additional ports, two on either side are provided at the midline for other diagnostics. This source was built so it would facilitate both filament and RF driven discharges, with minimum inconvenience for change-over.

3.2.1 The DC Volume Ion Source

The DC plasma is heated by a series of tungsten filaments located at the front of the source on a stainless steel endplate on the cylindrical system. The configuration is shown below in Fig. 2.3. This plate has 8 high power electrical feed-throughs rated to 100 V and 100 A which allow the connection of up to four filaments. The filaments are made of tungsten wire of diameter 1 mm and are approximately 120 mm in length. These filaments may be connected to operate in series or parallel. The plate has water-cooling channels, and the electrical feed-throughs are also water-cooled to prevent any damage to the ceramic isolation supports.

The discharge (duration typically 100 ms per shot) occurs between the filaments, the cathode and the chamber walls, the anode. A discharge of 70 V is generally applied between the filaments and the wall.

Power to the filaments is supplied with a Wayne-Kerr AP20-80 power supply unit. The source was operated by biasing the filaments negative to –70 V with respect to the anode using a Wayne-Kerr AP 70-30 power supply unit.

3.2.2 *Pulsing the DC Source*

The experimental set up is the same as described previously for the continuous discharge. However in order to modulate the discharge the discharge voltage is pulsed so as to generate an on-period and an off period, the discharge and post-discharge respectively. The discharge voltage can be modulated up to 10 kHz using a square-wave signal from a signal generator. This square-wave signal supplies a trigger for the diagnostics. A delay generator is used to determine the exact time in the discharge and post-discharge at which the diagnostics are triggered. The delay generator used is a Stanford Research Systems DG535 digital pulse generator.

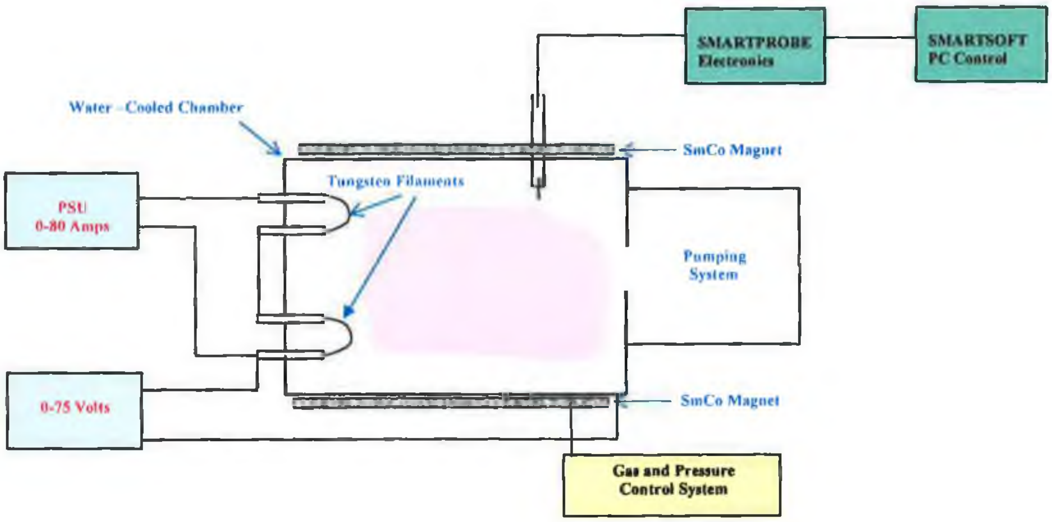

Fig. 3.3 Schematic of the Filament Driven Ion Source.

3.2.3 *The Extraction System*

The plasma electrode , made of stainless-steel, is a 3 mm thick plate with an aperture of 8 mm diameter. This extraction system is illustrated in Fig 3.4. The extraction electrode is mounted 3 mm behind the plasma electrode, and also has an aperture of 8 mm diameter. This electrode can be biased up to 8 kV with respect to the plasma electrode. The extraction electrode is 12 mm thick and is made up of two separate plates, with magnets arranged in an octopole arrangement which act as a filter to electrons, preventing them from reaching the detector. The magnetic field strength measured in this region is approx. $B > 1000$ G. The two plates are connected by a 10 kΩ resistor. Arriving electrons at the second plate cause the potential to become negative with respect to the first plate and also help to suppress further electron collection. Behind the second plate an end plate is mounted and 30 mm behind this the Faraday cups are mounted. There are 6 Faraday cups which are isolated from each other by means of ceramic strips, allowing for beam profile measurements. Extraction voltage and acceleration voltage can be up to 25 kV.

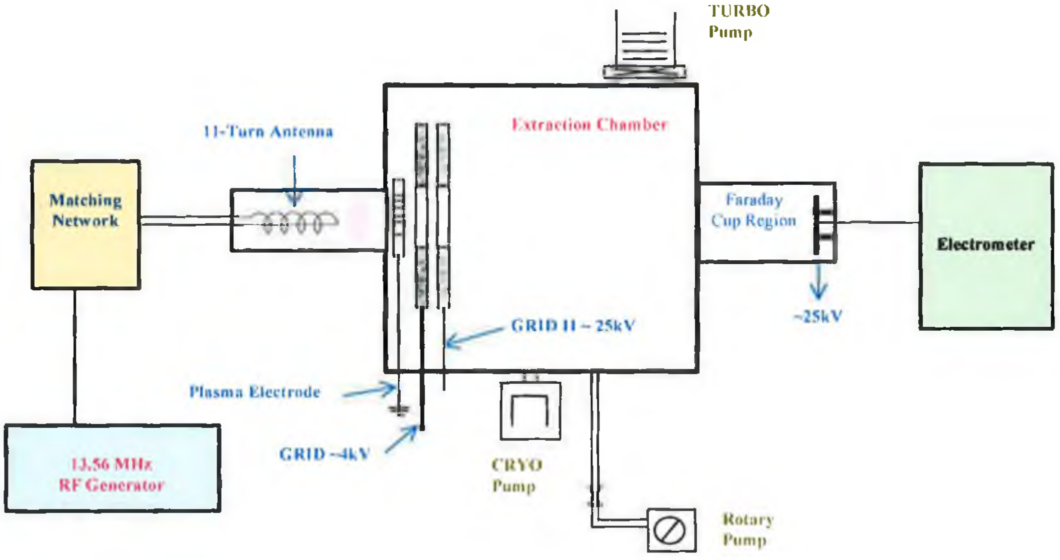

Fig. 3.4 Schematic of Ion Source and Extraction Chamber.

3.3 The RF Volume Ion Source

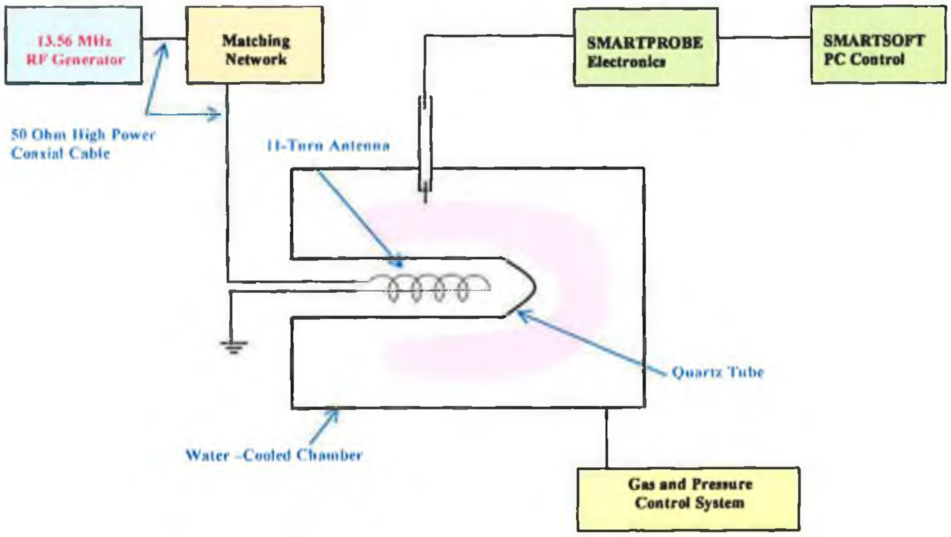

Fig. 3.5 The RF Ion Source.

The RF experimental system is an ICP with an internal antenna positioned along the axis of the cylindrical discharge chamber. A schematic of this system is seen above in

Fig. 3.5. A second stainless steel endplate exists which is designed to hold the RF antenna vacuum feed-through. The antenna consists of helically wound water-cooled copper tubing with eleven turns The antenna is driven by a 13.56 MHz RF power supply capable of generating up to 3.5 kW.

To generate the power to the plasma the problem of feeding the power from the RF generator to the discharge needs to be overcome. A circuit that transfers maximum power to the plasma has been applied by the use of an automatic matching network.

3.3.1 The Antenna

The antenna consists of 2mm diameter copper tubing wrapped in the form of a coil with 11 turns, with an inner diameter of 3.5 cm, and a length of approx. 6 cm. The resistance of the coil is measured to be 2 Ω and the inductance found to be 2 μH in a CW inductive mode.

The antenna sits in the centre of the volume ion source chamber, see Fig.3.5. It is housed in a quartz tube of thickness 4 mm, which keeps the antenna from direct contact with the plasma, and also keeps it at atmospheric pressure therefore reducing the possibility of arcing. Quartz glass is used as it is a good insulator and would not be heated by the induced electric field from the antenna. The antenna is water cooled through the inner diameter of the copper tubing which is done to prevent damage and also to minimise changes to the antenna resistance.

3.3.2 Pulsing the RF Ion Source

The probe used in this work is a Scientific Systems SmartProbe [3] and is operated within the pulsed discharge in boxcar mode. The RF power supply in use allows for pulsing of the discharge with a frequency of up to 1 MHz. The modulation frequency of the discharge is sent through delay electronics to produce an external trigger to the SmartProbe system and therefore data of an I-V characteristic and EEDF can be collected at a specific point in the pulse train of the discharge or afterglow. A schematic of the set-up is shown here in Fig. 3.6

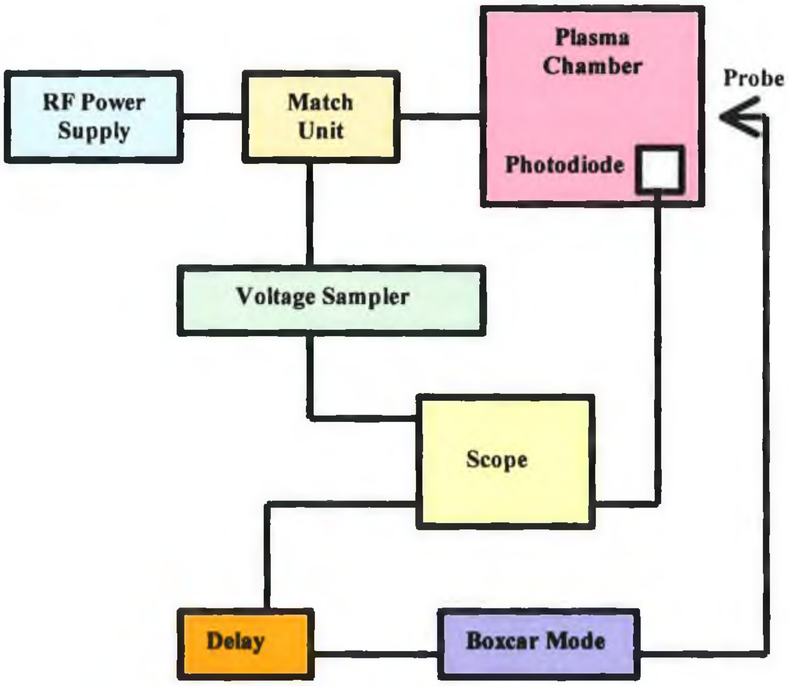

Fig.3.6 **Schematic of Logic for the Pulsing of the RF Ion Source.**

The pulsing of the RF generator is controlled by a LABVIEW® programme. This programme allows forward power to be set, pulse length to be determined and the modulation requency to be decided. Fig. 3.7 below shows the graphics user interface (GUI) for this programme.

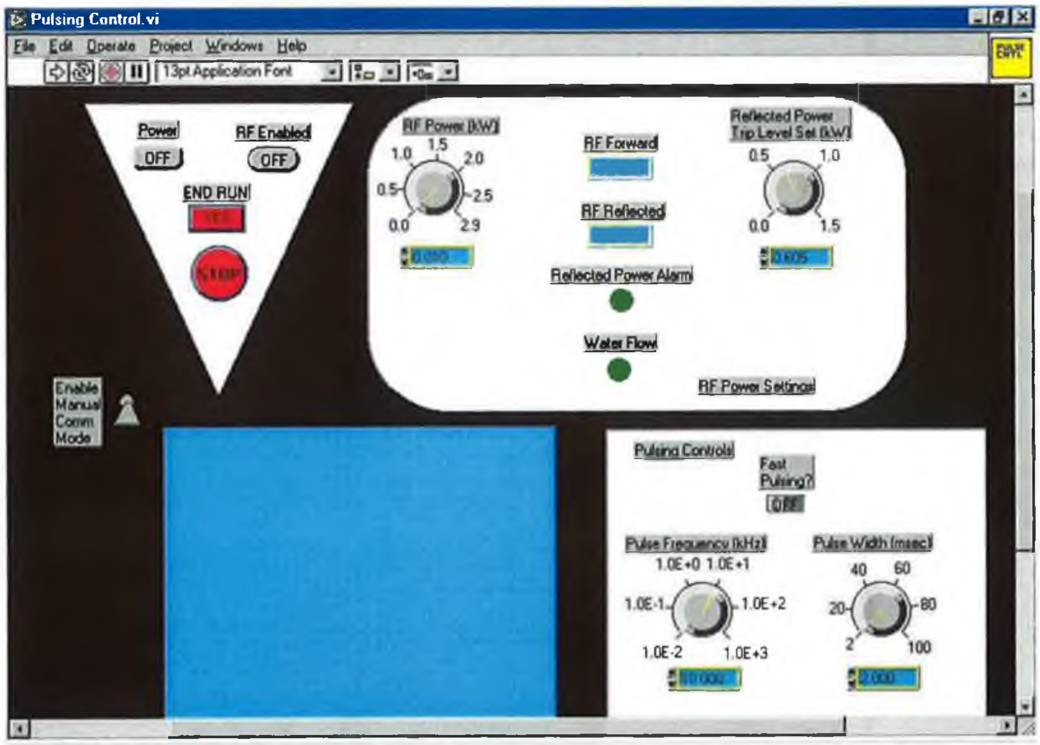

Fig. 3.7 **GUI for RF Pulsing Control.**

3.3.3 The Bird Power Meter

A directional power meter, BIRD Model 43, is used to measure the RF power. It has a power range of 1 W to 1 kW and a frequency range of 0.45 MHz to 2300 MHz. The meter allows both forward and reverse sensing of powers by means of a rotatable element. The element contains a loop that detects the magnetic field in the nearby section of the RF current carrier. A potential difference appears across the loop proportional to the current in the carrier and the mutual inductance between the loop and the current carrier.

The voltage seen by the meter is the voltage across the resistor R and the voltage across the inductor with mutual inductance M with the RF line.

$${}_{probe} = jwCRV \pm jwMI \qquad \textit{Equation 3.1}$$

The values are chosen so that they satisfy the equation:

$$CR = \frac{M}{Z_0} \qquad \textit{Equation 3.2}$$

Where Z_0 is the characteristic impedance of the line carrying the RF current, which is 50 Ω. The equation for the probe voltage now becomes

$${}_{probe} = jwM(\frac{V}{Z_0} \pm I) \qquad \textit{Equation 3.3}$$

The sum of the forward and reflected voltages gives the voltage at any point on the transmission line. The current is given by:

$$I = \frac{V_f}{Z_0} - \frac{V_r}{Z_0} \qquad \textit{Equation 3.4}$$

Thus the voltage on the probe when in the forward direction and the voltage when rotated by 80° are then given by the following equations respectively:

$${}_{probe} = \frac{j2wMV_f}{Z_0} \qquad \textit{Equation 3.5}$$

3.4 Langmuir Probe

The Langmuir Probe is commonly regarded as one of the most important and versatile plasma diagnostic tools, due to its simplicity of design and in-situ measurements, providing local information of the various plasma parameters. Because of its ability to measure the various parameters over a wide range of experimental conditions and to measure the electron energy spectrum, the probe is regarded as one of the superior plasma diagnostic techniques.[4] The parameters measured include electron density, ion density, electron temperature, plasma potential, floating potential and the electron energy distribution function. The probe diagnostic consists of placing a conductor into a plasma, applying a voltage and measuring the resulting current drawn. The resultant plot is that of an I-V characteristic of the plasma. The theory of probes is reasonably well established, allowing it to become the very popular tool that it now is [5], [6], [7]. The probe used in this work is a Scientific Systems SmartProbe [8]. It is a cylindrical probe, so it may easily be employed in both radial and spatial measurements, and has a small surface area so as to minimise disturbance to the plasma.

When the probe is biased, the sheath that surrounds it increases in width, and so the particle collection changes from being radial to orbit motion limited. When this happens all particles entering the sheath are not collected [9]. The Laframboise theory is used to account for the expansion of the sheath with biasing of the probe [10]. As this theory does not take collisions into account it only holds valid for low pressure discharges or small sheaths. This theory is described in this section in detail.

3.4.1 Probe Theory

A typical I-V probe characteristic is shown here in Fig. 3.8.

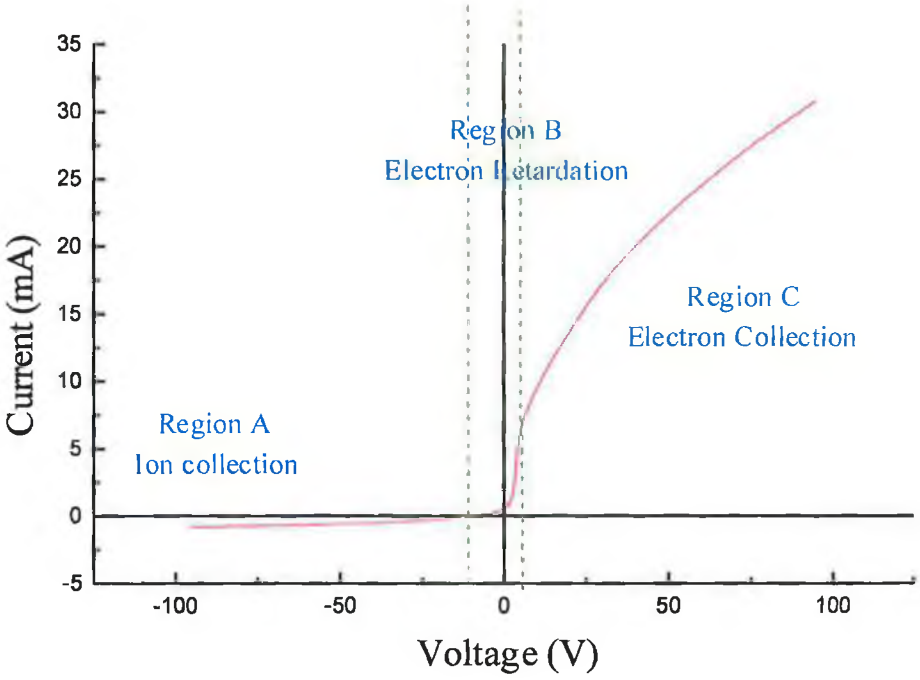

Fig. 3.8 **Example of a Typical Langmuir Probe I-V Characteristic.**

The characteristic can be broken down into three sections, as illustrated. In region A, the probe is biased strongly negative with respect to the plasma, therefore repelling all contributing electrons and attracting only positive ions. The current collected here is the ion saturation current, $I_{i_{sat}}$, and is expressed as

$$I_{i_{sat}} = \frac{1}{4} n_{i0} e A \bar{u}_s \qquad \textit{Equation 3.6}$$

where, A is the probe sheath area, n_{i0} is the ion density and $\bar{u}_s$ the ion acoustic velocity, or Bohm velocity [8], given by:

$$\bar{u}_s = \left(\frac{kT_e}{m_i}\right)^{1/2} \qquad \textit{Equation 3.7}$$

This velocity is defined as the minimum velocity required by the ions to enter the sheath.

In region B, the probe bias is becoming more positive. This is known as the electron retardation region. As the bias is made less negative, fast electrons start to be collected. At a certain probe bias the flux of electrons and ions equal each other and the net collected current is zero. The potential is known as the floating potential, V_f. As the probe bias becomes more positive, the probe starts collecting the faster electrons which are able to overcome the retarding potential. As the bias increases the slower electrons of the velocity distribution are collected.

In conjunction with this, the thickness of the ion sheath decreases. The density of the electrons in this ion sheath is governed by Boltzmann's Law [9]

$$n_e = n_{e(0)} \exp\left(\frac{eV_p}{kT}\right)$$ *Equation 3.8*

where $n_{e(0)}$ is the electron density in the plasma, V_p is the plasma potential, and T the temperature in Kelvin. The random current at the sheath edge, like that for the ions saturation current equation Eqn.3.1, is given by

$$I_{e(0)} = -\frac{1}{4} n_0 e A \overline{u}_e$$ *Equation 3.9*

In this equation $\overline{u}_e$ is the average electron velocity, calculated from the Maxwell-Boltzmann velocity distribution and found to be

$$\overline{u}_e = \left(\frac{8kT_e}{\pi m}\right)^{½}$$ *Equation 3.10*

The total collected current in region B of retarding potential is then [6], [10],

$$I_{probe} = I_{i_{sat}} + I_{e(0)} \exp\left(\frac{eV_p}{kT_e}\right)$$ *Equation 3.11*

On increasing the probe voltage further, a potential is reached where there is no sheath around the probe tip. Here the probe is at the same potential as the plasma and hence is called the plasma potential and denoted by V_p. With no sheath around the probe tip electrons and ions migrate to the tip by their own thermal velocities. Electrons being lighter than ions have a higher mobility and hence the current collected at this potential is electron-dominated.

In region C, the probe bias is increased further, becoming more positive. The ions are not collected due to the fact that they can not overcome the potential drop within the sheath around the probe. The current collected is just electrons, and this region is called the electron saturation region. The current collected by the probe here is given by

$$I_{e_{sat}} = -\frac{1}{4} n_{e(0)} e A \bar{u}_e \qquad \textit{Equation 3.12}$$

From the above analysis it can be seen that much can be deduced about the plasma parameters by means of the probe. However this analysis only holds true for low pressure plasmas where,

$$r_p < \lambda \qquad \text{and} \qquad \lambda_d < \lambda \qquad \textit{Equation 3.13}$$

where r_p is the probe radius, λ the electron collisional mean free path, and λ_d the Debye length which is given by:

$$\lambda_d = \left(\frac{\varepsilon_0 k T_e}{e^2 n_e} \right)^{1/2} \qquad \textit{Equation 3.14}$$

Other assumptions are also made, these include [10][11]:

- That the plasma is assumed infinite, homogeneous and quasineutral in the absence of a probe.
- That all charged particles striking the probe are assumed to be absorbed.
- That no magnetic fields are present.
- That velocity distributions for both electrons and ions are assumed to be Maxwellian distributions.
- That electrons and ions of temperatures T_e and T_i, hold the condition that $T_e >> T_i$.

It is recognised that the above assumptions do not always hold true and some discussion of this is included in this text.

It is obvious from the above probe theory that the acquisition of an I-V characteristic provides a lot of information about the plasma, but in order to determine specific plasma parameters further analysis is required. This is explained in the following section.

3.4.2 Determination of Plasma Parameters

In order to reduce perturbation to the plasma by the probe a cylindrical, small area probe is used. This also has the advantage of having a definitive theory describing the behaviour of the sheath [5], [7]. Once the sheath behaviour, and therefore the ion current expansion is known, the ion density, n_+, can be determined. Using a small area probe also has the advantage of reducing the depletion of low energy electrons, which is beneficial for low-density plasmas or weak magnetic fields [5]. The probe theory used in analysing the characteristic is that of Laframboise [7].

The expansion of ion current to the probe may be described as a function of applied voltage, V, as shown here:

$$\frac{I_+}{I_{+_{th}}}(V) = f\left(\frac{r_p}{\lambda_d}, \chi\right), \qquad V < V_p \qquad \textit{Equation 3.15}$$

$$\frac{I_e}{I_{e_{th}}}(V) = F\left(\frac{r_p}{\lambda_d}, \chi\right), \qquad V > V_p \qquad \textit{Equation 3.16}$$

where χ is the non-dimensional probe voltage, $I_{+_{TH}}$ is the thermal ion current and $I_{e_{th}}$ is the thermal electron current. These are given as

$$\chi = \left(\frac{e(V - V_P)}{kT_e}\right) \qquad \textit{Equation 3.17}$$

$$I_{+_{th}} = n_+ r_p e\left(\frac{2\pi k T_e}{m_+}\right)^{1/2} \qquad \textit{Equation 3.18}$$

$$I_{eth} = n_e r_p e\left(\frac{2\pi kT_e}{m_e}\right)^{1/2}$$ *Equation 3.19*

The function $f\left(\frac{r_p}{\lambda_d},\chi\right)$ is the expansion factor as calculated by Laframboise in the zero ion temperature limit $T_+ < T_e$, n_+ and n_e are the ion and electron densities, respectively, and r_p the probe radius. The function f is derived from numerical fits to Laframboise curves where the ion and electron thermal currents are used as scaling factors [10].

On examining the above equations it is seen that a knowledge of some of the plasma parameters is required to use the above theory. A value for the plasma potential, V_p, the electron temperature, kT_e, and the Debye length, λ_d, are needed. To overcome this iteration is required. An I-V probe characteristic is taken, and using simple Langmuir theory V_p, kT_e and λ_d are estimated [5]. A value for the plasma potential is easily calculated by determining the first derivative of the I-V and the slope of the exponential section produces a value for kT_e. Determination of $\chi(V)$ then provides the most suitable value for r_p/λ_d by fitting the observed current, $I(\chi)$, to the theoretical predictions of Laframboise [12]. This fit takes place at a very negative voltage where no fast electrons are included in the collected current.

Calculations of the other plasma parameters, the floating potential, V_f, the electron and ion densities, n_e and n_+ respectively, can now be made from the approximations already made of V_p, kT_e and r_p/λ_d. n_e The ion density is found by combining *Equation 3.14* and *3.17* and the electron density is found by combining *Equation 3.15* and *3.18* such that

$$n_+ = \frac{I_+(\chi)}{er_p\left(\frac{2\pi kT_e}{m_+}\right)^{1/2} f\left(\frac{r_p}{\lambda_d},\chi\right)}, \chi < 0$$ *Equation 3.20*

$$n_e = \frac{-I_e(\chi)}{er_p\left(\frac{2\pi kT_e}{m_e}\right)^{1/2} f\left(\frac{r_p}{\lambda_d},\chi\right)},\chi > 0$$ *Equation 3.21*

where $I_+(\chi)$ is the current measured at a very negative voltage to remove any contribution from electrons, and $I_e(\chi)$ is the current measured at some positive potential with respect to the plasma potential, V_p. It has been found that the determination of the plasma potential from the first derivative of the I-V characteristic yields a value for the maximum that always occurs below the point of saturation. It can be corrected by means of the intersecting slope method. This new value for V_p is then determined by the following equation,

$$V_p = V_{\max} + kT_e \ln\left(\frac{I_{sat}}{I_{\max}}\right)$$ *Equation 3.22*

where $V_{\max}$ and $I_{\max}$ are the voltage and current, respectively, at the maximum of the first derivative and I_{sat} is the electron saturation current.

A new value for the electron temperature, T_e, is then calculated from the new value of the electron current as shown here,

$$I_e(\chi) = I_{\max}(\chi) - I_+(\chi)$$ *Equation 3.23*

Figures 3.9(a) and 3.9(b) below show the characteristic I-V's and EEDF's measured by the SmartProbe.

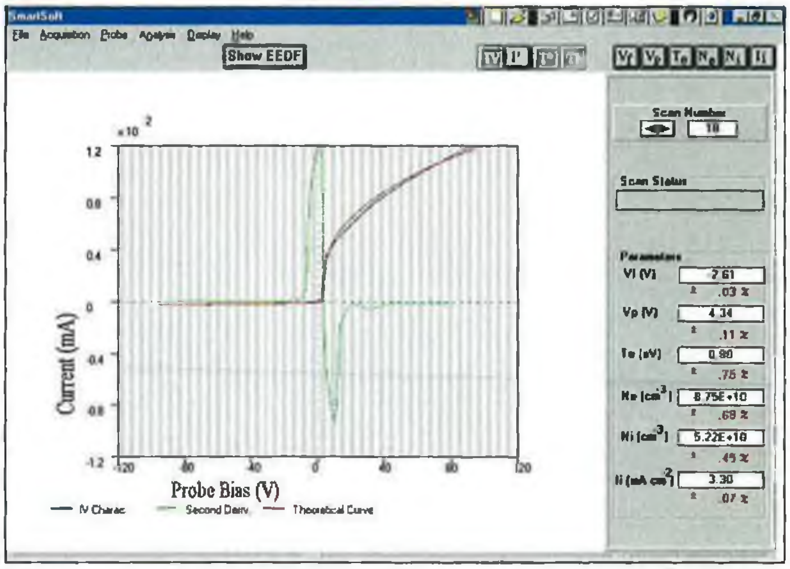

Scan Number: 10

Scan Status

Parameters

Vf (V): -2.61 ± .03 %

Vp (V): 4.34 ± .11 %

Te (eV): 0.90 ± .75 %

Ne (cm^{-3}): 8.75E+10 ± .69 %

Ni (cm^{-3}): 5.22E+10 ± .45 %

Ii (mA cm^{-2}): 3.30 ± .07 %

Fig. 3.9(a) **Typical I-V Characteristic Collected by the SmartProbe.**

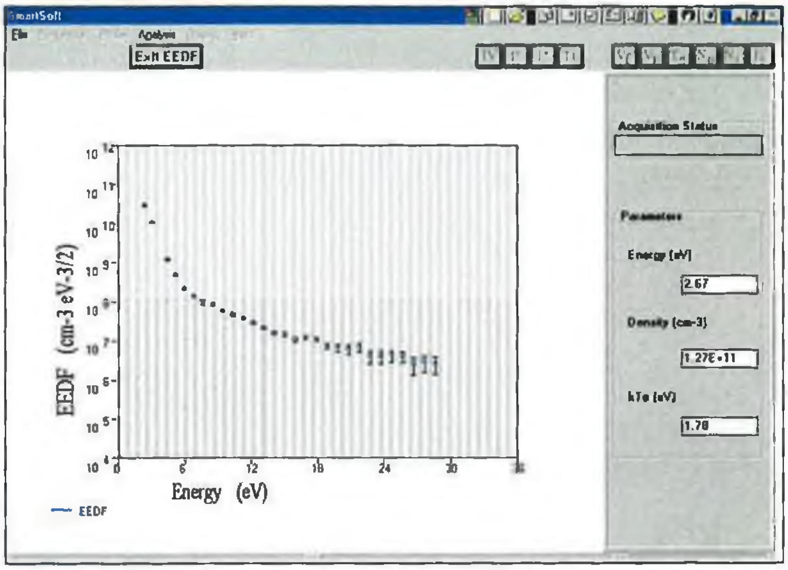

Acquisition Status

Parameters

Energy (eV): 2.67

Density (cm-3): 1.27E+11

kTe (eV): 1.78

Fig. 3.9(b) **Typical EEDF Collected by the SmartProbe.**

3.4.3 Determination of the Electron Energy Distribution

The electron energy distribution function (EEDF) provides fundamental and important information about the plasma, how it is heated and how it is sustained. It is also necessary in calculating the rate coefficients for ionisation and excitation. Calculating the integral over the EEDF provides values for both the electron density, n_e, and the reaction cross-sections, $\langle \sigma u \rangle$, as shown here,

$$\langle \sigma u \rangle = \int_{threshold}^{\infty} f(\varepsilon)\sigma(\varepsilon)u(\varepsilon)\,\mathrm{d}\,\varepsilon \qquad \textit{Equation 3.24}$$

Here, $f(\varepsilon)$ is the normalised EEDF, σ is the reaction cross-section, and u is the electron velocity. The second derivative of the I-V probe characteristic is proportional to the EEDF provided it is isotropic [13], giving,

$$n(\varepsilon) = n_e f(\varepsilon) = \frac{2}{eA}\frac{d^2 Ie}{dV^2}\left(\frac{2m\varepsilon}{e}\right)^{1/2} \qquad \textit{Equation 3.25}$$

where the energy, $\varepsilon = V - V_p$.

So by differentiating the probe current twice with respect to the probe bias the EEDF is obtained.

3.5 Laser Photodetachment Technique

One of the most successful methods of measuring negative hydrogen ion densities to date is that of photodetachment by a pulsed laser [16, 17]. Other methods such as mass spectroscopy [18] and Langmuir probes [19, 20] have been used to carry out measurements of H^- in the discharge. The photodetachment technique described here is used to spatially resolve the H^- density throughout the discharge, and therefore give a better insight into the behaviour of the plasma.

The photodetachment reaction is a light-matter interaction where a photon is used to remove an electron from a negative ion when the photon energy is greater than the electron-hydrogen ion binding energy, E = 0.75 eV. This reaction equation is shown in equation 3.26

$$H^- + hv \Rightarrow H + e^- \qquad \textit{Equation 3.26}$$

In the 1950's, experiments using a well-collimated beam of light from a carbon arc lamp to detach electrons from the negative ions in the beam path were carried out by Branscomb [21].

In the experiments carried out and described here in this work, a laser pulse beam is used to detach the electron, making the technique more versatile and simpler. Detaching an electron from the negative ion obviously results in an increase in the electron density, which may then be detected by the Langmuir probe described earlier. The probe must be located in the light-plasma interaction volume.

A Nd-YAG laser can be used for the photodetachment because the photon energy of 1.1 eV is enough to detach the electron as required, and yet not result in photoionisation, photoemission or photodetachment of other species.

The fraction of negative ions in the beam path detached by a pulse of laser light can be determined by the following equation, *Equation 3.27*. [16].

$$\frac{\Delta n^-}{n^-} = 1 - \exp\left[\frac{-E}{A} * \frac{\sigma^{ph}}{h * v}\right] \qquad \textit{Equation 3.27}$$

where A is the cross-sectional area of the laser beam, E is the laser beam Energy, h is Planck's constant, v is the frequency of the laser light and σ^{ph} is the cross-section for photodetachment at the photon energy being used, in this case it is $3.6 * 10^{-17}$ cm^2 [22]. If the laser energy is large enough to saturate the photodetachment signal then the cross-section becomes insignificant. The negative ion density to the probe can then be estimated by *Equation 3.28* [23, 24] Once the signal is saturated this density is proportional to the amplitude of the photodetachment signal, ΔI_{e^-}. H$^-$ values may then be determined once the electron density and continuous current to the probe is known.

$$\frac{n^-}{n_e} = \frac{\Delta n_e}{n_e} = \frac{\Delta I_{e^-}}{I_{e^-}} \qquad \textit{Equation 3.28}$$

3.5.1 Experimental Set-up and Apparatus for Laser Photodetachment Technique

The experimental set-up of the laser photodetachment measurement tool requires the orientation of the detecting probe to be co-axial to the laser beam path. The configuration is shown in Fig. 3.10

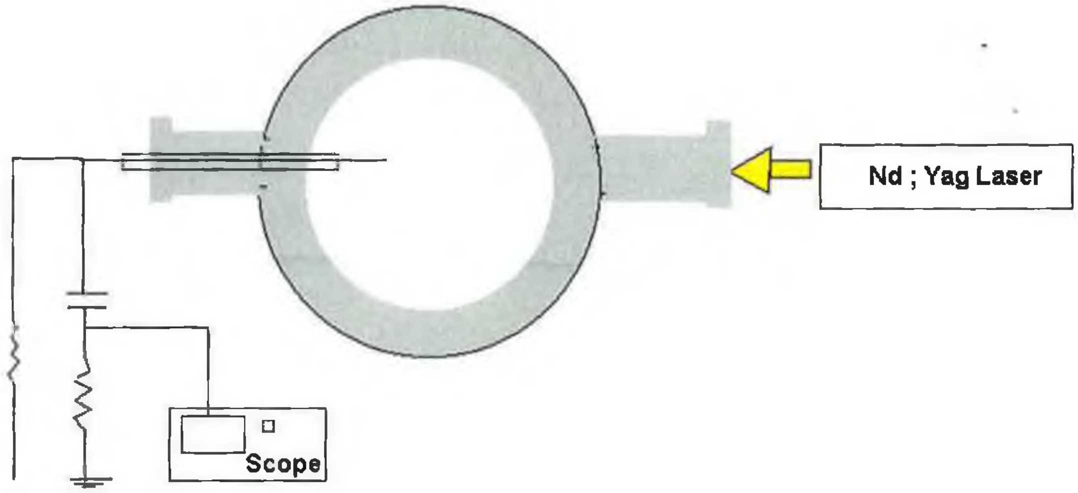

Fig. 3.10 Schematic Representation of the Photodetachment Apparatus.

The probe used consists of a tungsten wire of diameter 1 mm and length 10 mm, supported by a ceramic sleeve and housed in a quartz tube inserted to the chamber with a Wilson Seal, thus allowing movement of the probe in the spatial plane co-axial to the beam path.

It is important to note that the ceramic sleeve did not touch the tungsten wire and therefore the surface area of the probe was not altered by deposition of carbon or other contaminants.

The laser pulse is generated by a spectron SL400 pulsed Nd:YAG laser, capable of delivering 300 mJ, with a pulse length of 9 ns. It was operated at its fundamental mode at 1064 nm, as the photodetachment cross-section at this wavelength is near its maximum[22]. This laser pulse is aligned with a HeNe CW laser at 632.8 nm. The DC electron current signal generated from the plasma electrons is filtered from the AC signal generated by the collected electrons due to the photodetachment by means of the circuit shown in Fig. 3.11. The signal is captured on a fast-recording oscilloscope.

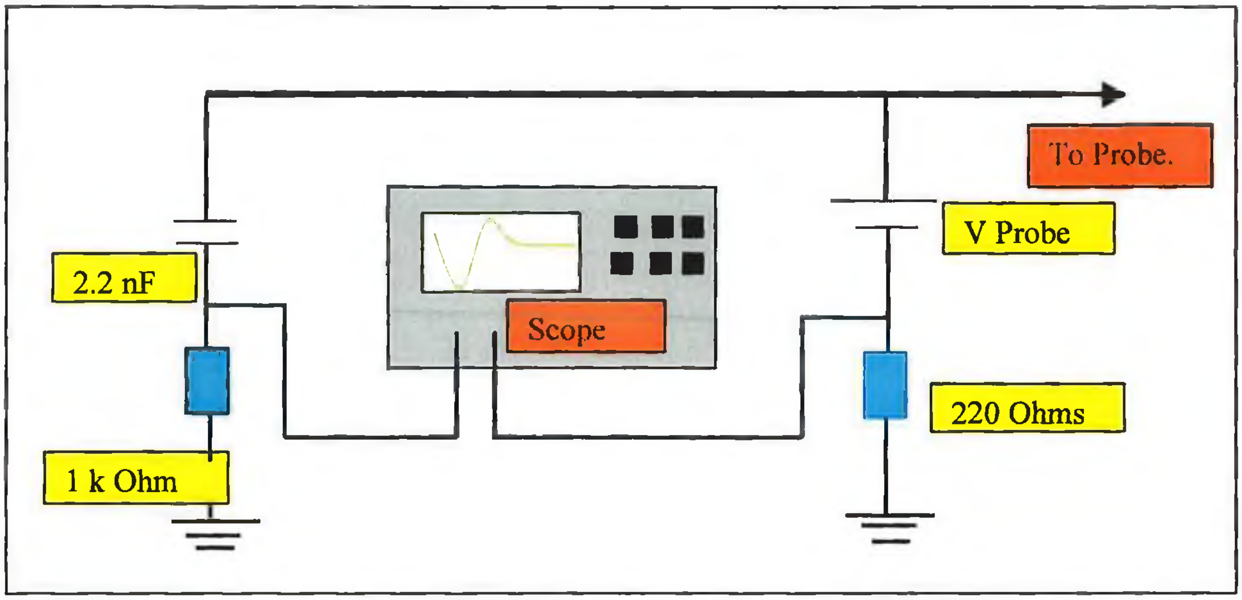

Fig. 3.11 **Electrical Circuit for photodetachment probe**

3.5.2 Determination of Optimum Operating Conditions for Photodetachment Measurements.

A typical photodetachment characteristic signal, as shown in Fig. 3.10, is collected with the above apparatus. As the laser light enters the interaction volume the hydrogen ions are dissociated as indicated in *Equation 3.26*, creating electrons and hydrogen atoms. The increase in electrons does not initially lead to a change of charge density in the region as the numbers of positive and negative particles is not affected by the photodetachment reaction, and no potential difference exists between the interaction region and the bulk plasma.

The positively biased Langmuir probe collects the detached electrons. These collected electrons cause a potential difference across the 1 kΩ resistor, giving a drop in the potential until a minimum is reached. This potential is proportional to the total extracted electron current, ΔI_{e^-}. A flux imbalance occurs between the detached electrons leaving the interaction region and the negative ions entering this region. The reason for this is that the electrons leaving are more energetic and mobile than the negative ions entering, thus a charge imbalance results, causing a positive potential as the negative charges are depleted. This then leads to the generation of an electric field, accelerating negative charges into the reaction region.

As stated previously, the electron-hydrogen binding energy, or electron affinity of hydrogen is 0.754 eV, the photon energy is 1.2 eV. This results in the photodetached electrons having an energy of 0.455 eV. The electron energy distribution evolves quickly to a near-maxwellian distribution, so a Boltzmann relation may be applied. as in *Equation 3.29.*

$$\Delta V = \left(\frac{kT_e}{e}\right)\ln\left(\frac{n_e + \Delta n_e}{n_e}\right) \qquad \textit{Equation 3.29}$$

The electrons in the bulk are denoted by n_e, the photodetached electrons given by Δn_e in the reaction area and kT_e is the electron temperature.

As the characteristic signal goes from the minimum back to its equilibrium value, the flux of negative ions into the volume exceeds the positive ion flux, and so a negative potential develops, generating an electric field which then accelerates the electrons out of the reaction region and pulls the positive ions in.

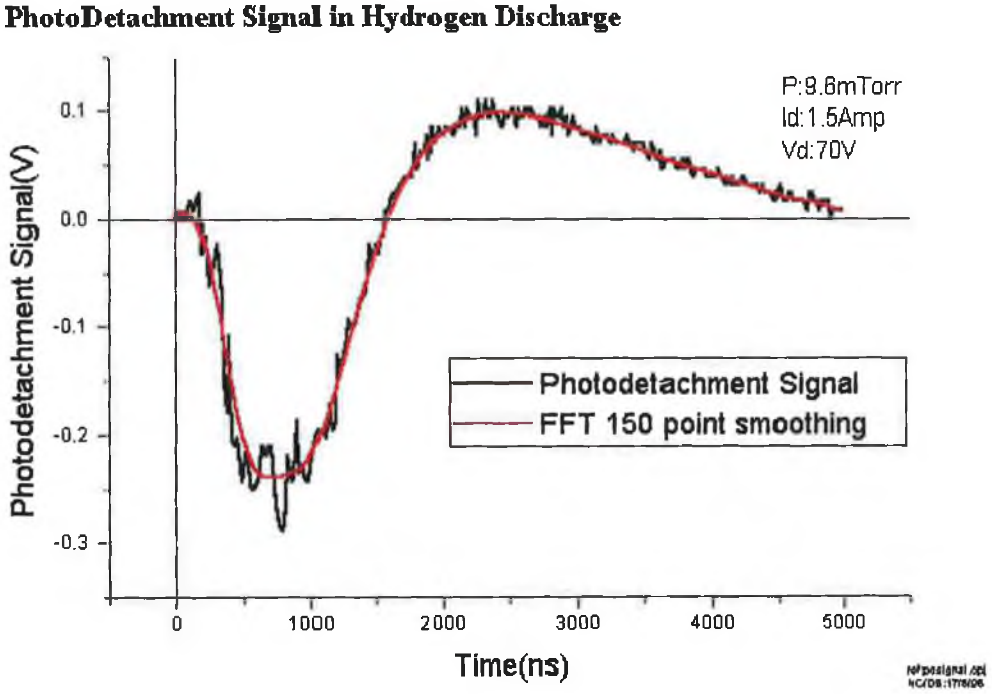

Fig. 3.12 **Typical Photodetachment Signal.**

As mentioned previously, *Equation 3.27* gives the fraction of negative ions detached for a given energy

$$\frac{\Delta n^-}{n^-} = 1 - \exp\left[\frac{-E}{A} * \frac{\sigma^{ph}}{h * v}\right] \qquad \textit{Equation 3.30}$$

An experimental plot to characterise the variation of the photodetachment signal with the laser energy is carried out. This is then compared with the theoretical value obtained by calculations with *Equation 3.27*. This experimental versus theoretical plot is shown in Fig. 3.13. Correlation between the theoretical and experimental curves ensures that the detached signal is indeed a negative ion effect.

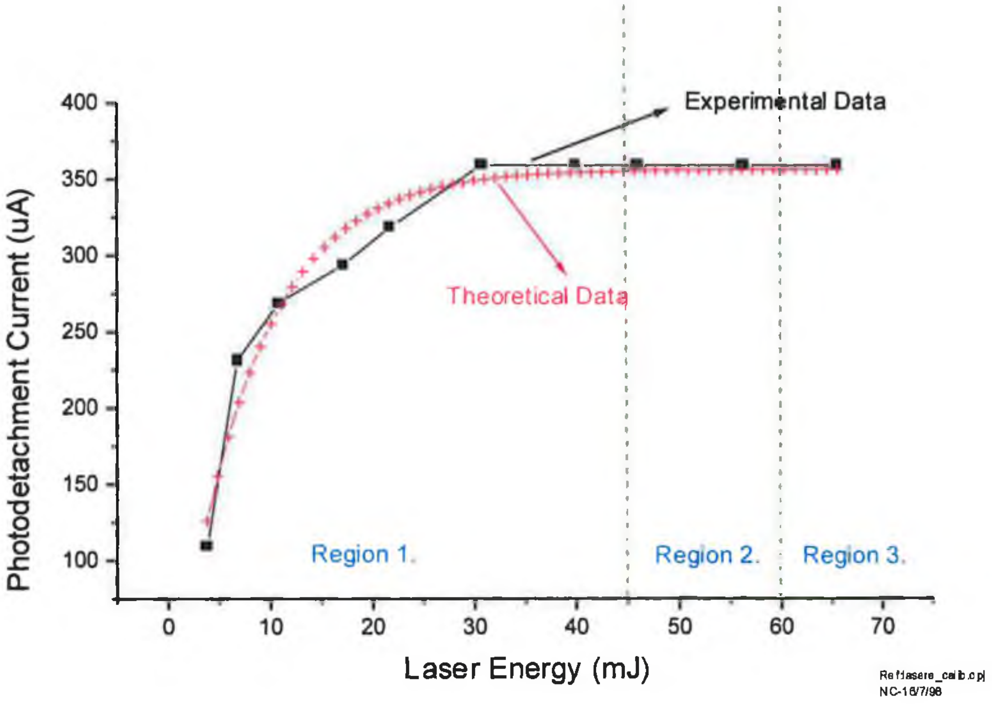

Fig 3.13 **Theoretical and Experimental Dependence of Photodetachment Current on Laser Energy.**

As can be seen from the above diagram, the correlation between the two curves is quite good. The curve can be broken down into three regions. In the first region the photodetachment signal rises. This is due to the increasing number of negative ions undergoing photodetachment as the laser energy is increased. In the second region, between 45 mJ and 65 mJ, the signal saturates. This happens when all the negative ions in the interaction volume are being photodetached, and all the electrons are being collected. In region three, there is a further increase in the signal. This increase is not in fact due to further photodetachment. As the laser light rises above this level, the light begins to interact with the tungsten tip, causing ablation of the tip. Electrons emitted by this interaction are then also collected, causing the increased signal observed.

The assumption that all the negative ions detached are negative hydrogen ions also holds valid, as any other ions that may be detected in the signal would be mainly due to oxygen. Species such as O^-, O_2^-, OH^-, may be detached at the energy being used, but the photodetachment cross-sections, σ^{ph}, for these are orders less than for H^- [21].

To determine the optimum operating voltage at which to bias the Langmuir probe, a photodetachment signal variation with probe voltage is plotted in Fig. 3.14. This eliminates the possibility of probe voltage effects on the measured signal. Fig 3.14 shows an increase in photodetachment signal with increasing probe voltage. This signal saturates at about 45 V. It is at this voltage that all further photodetachment measurements are taken with the Langmuir probe.

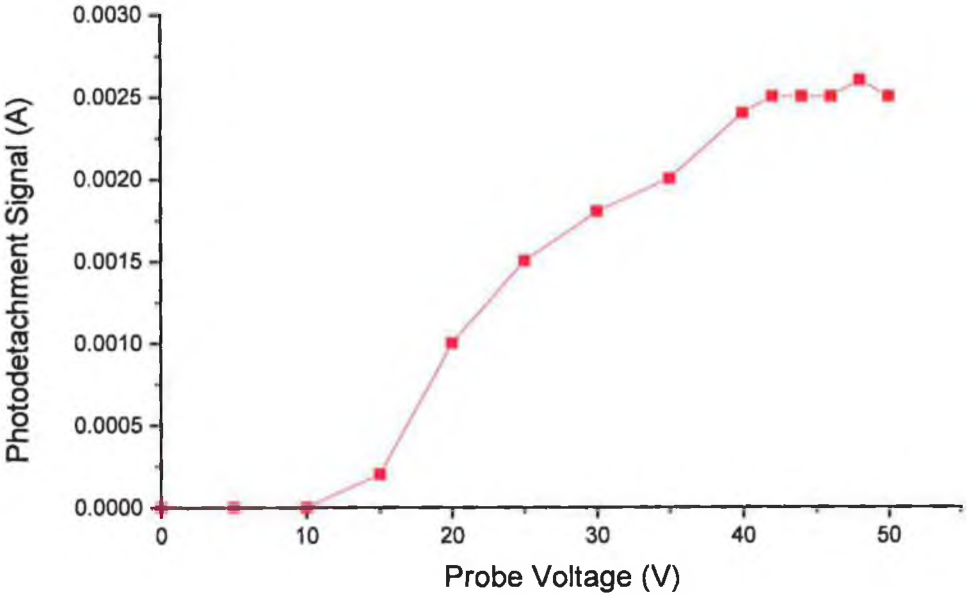

Fig. 3.14 **Photodetachment Dependence on Probe Voltage.**

To determine the effect of modification of the beam diameter, therefore varying the cross-sectional area, A, in *Equation 3.27*, various apertures were constructed and placed in the laser beam path. Aperture diameters of 3 mm, 5 mm, 8 mm and 12 mm were constructed and tested. It was found that the signal saturated with the 8 mm aperture diameter beam. All further photodetachment measurements were taken with this beam diameter.

Finally the photodetachment technique was tested on an argon discharge which generates no negative ions. This eliminated the possibility of effects due to positive ions or electrons.

3.6 Summary

A description of the filament driven and RF ICP volume ion sources under investigation on the DENISE system has been presented. The diagnostics used are the Langmuir probe and a laser photodetachment technique, both of which have been described in detail in this chapter. Using these diagnostic techniques, both sources can be characterised, revealing much information about the plasmas generated and information on negative ion densities determined when operating in continuous and pulsed modes.

References

[1] Mellon, K.N.
PhD Thesis, Dublin City University, 1991.

[2] McNeeley, P, Boilson, D, Curran, N, Vender D, Hopkins, M.B.
Rev. Sci. Instrum., 69 (2)II, p983, 1998.

[3] SmartProbe Manual., Scientific Systems, Unit 3 Howth Junction Business Park, Kilbarick, Dublin 5.

[4] Godyak, V.A., Piejak, R.B., and Alexandrovich, B.M.
J. Appl. Phys., 73(8), p3657, 1993.

[5] Chapman, B.
"Glow Discharge Processes"
Wiley and Sons, New York, 1980.

[6] Bernstein, I.B. and Rabinowitz, I.N.
Physics of Fluids, 2 (2), p112, 1959.

[7] Scanlan, J.V.
PhD Thesis, Dublin City University, 1991.

[8] Hopkins M, Graham W
Rev. Sci. Instrum., 57, p2210, 1986

[9] Chen, F.
"Plasma Diagnostic Techniques",
Huddlestone and Leonard, Academic Press, New York, 1965.

[10] Laframboise, J.G.
UTAIS Report No. 100, 1966.

[11] Lieberman, M. and Lichtenberg, A.
"Principles of plasma discharges and materials processing"
John Wiley & Sons Inc., New York, p158, 1994.

[12] Lipschultz, B., Hutchinson, B., LaBombard, B. and Wan, A.
J. Vac. Sci. A., 4(3), p1810-1816, 1986

[13] Schott, L.
"Plasma Diagnostics"
Holtgreven, W.L., North Holland, Amsterdam, 1968.

[14] Hopkins, M.B., Graham, W.G. and Griffin, T.J.
Rev. Sci. Instrum. 58(3), p475, 1987.

[15] Druyvesteyn, M.J,
Z. Phys., 64, p781-798, 1930.

[16] Bacal, M. Hamilton, G.W.
Physical Review Letters, 42, p1538, 1979.

[17] Devynck, P, et al.
Review of Scientific Instruments, 60(9), p2873, 1989.

[18] Nicolopoulou, E, Bacal, M. and Doucet, H.J.
Journal de Physique, 38, p1399, 1977.

[19] Katsch, H.M. and Quandt, E.
"4th European Workshop on the Production and Application of Light Negative Ions", Belfast, 1991.

[20] Ameniya, H.
Journal of Physics D: Applied Physics, 23, p999, 1990.

[21] Branscom, L.M.

Atomic and Molecular Processes, Academic Press 1962.

[22] Smith, S. J. and Burch, D.S.
Physical Review Letters, 116, p1125, 1959.

[23] Mellon, K.N., Coonan, B.P. and Hopkins, M.B.
Journal of Physics D: Applied Physics, 27, p2480, 1994.

[24] Eenhuistra, P.J., et al.
Journal of Applied Physics, 67 910, p85, 1990.

Chapter Four

Plasma Parameter Measurements

4.0 Introduction

This chapter is devoted to the presentation and discussion of Langmuir probe measurements carried out in H_2 discharges on both the RF and DC systems described previously in Chapter Two. Determination of the plasma parameters, the electron density, ion density, electron temperature, plasma potential, floating potential and EEDF's are carried out in a CW mode of operation of both the filament generated and RF generated plasmas. The applied magnetic field is modelled and examined, and its effects, in particular, on the spatial dependence of the electron densities and temperatures investigated.

The concept of temporal filtering is examined, and the effect of pulsing the discharge investigated with respect to the plasma parameters. These values were determined over a range of pressures and powers.

Having generated both types of plasmas in the same system, the discharges are examined without any geometrical complications. The parameters measured are presented and discussed here.

4.1 Experimental Apparatus

The probe configuration consists of a small tungsten wire, 0.18 mmdiameter and 10 mm in length, supported in a ceramic tube. It can be moved radially in the ion source chamber. The operation of this probe has been described previously in Section 3.4. In short, a voltage varying between -95 V to 95 V is applied to the probe and the current drawn is measured.

The resultant current and voltage points are plotted giving the characteristic I-V curves. These characteristics can be spatially and temporally resolved throughout the discharge. The I-V characteristics are then analysed as explained previously, Section 3.4, to determine the plasma parameters.

4.2 Measurement of Plasma Parameters in the DC Ion Source

Typical I-V characteristics are shown in Fig. 4.1 and Fig. 4.2. Fig 4.1 shows the increase in current collected by the probe for a 10 mTorr H_2 discharge in a filament driven discharge when the discharge current is increased. Fig. 4.2 shows electron density variation for 0.5 A to 3.5 A discharge currents at 10 mTorr, with a discharge potential of 70 V, taken 15 cm from the front plate in the centre of the discharge. The electron density is seen to increase linearly with the increasing discharge current. More importantly, Fig. 4.3 shows the effect of increased pressure on the electron density and the electron temperature.

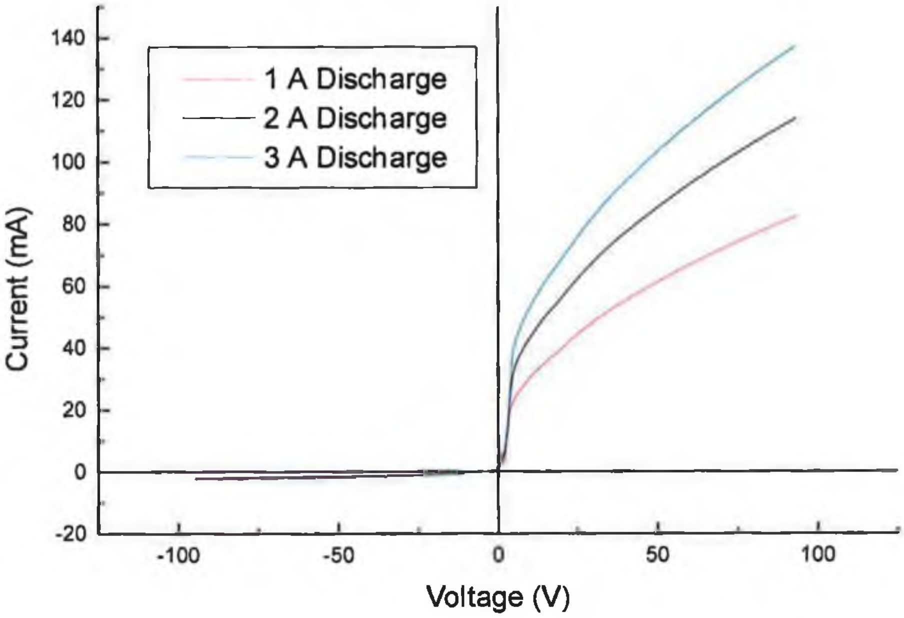

Fig. 4.1 **I-V Characteristics for Different Discharge Currents in a 10 mTorr Hydrogen Discharge.**

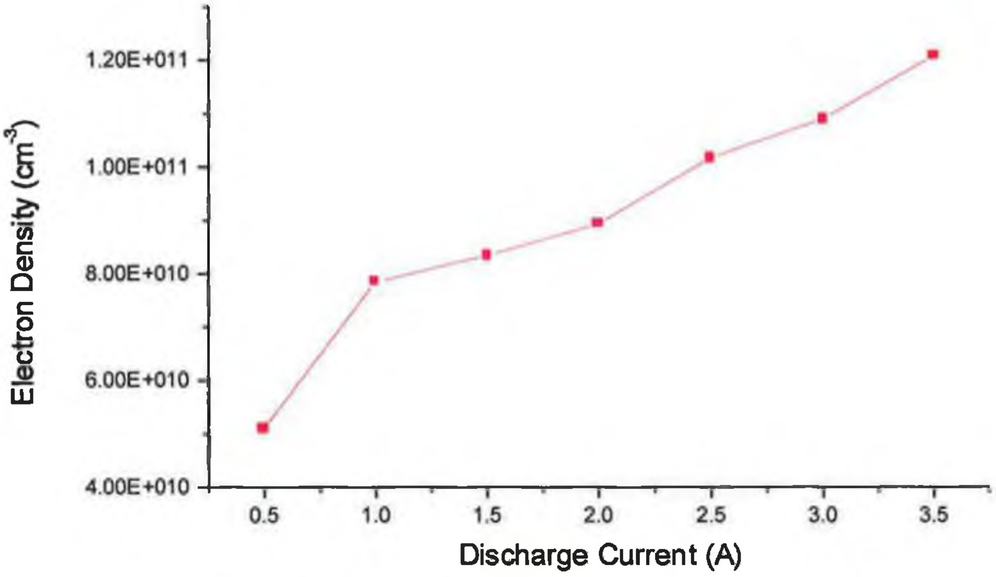

Fig.4.2 **Electron Density Variation with Discharge Current for a 10 mTorr, 70 V Discharge**

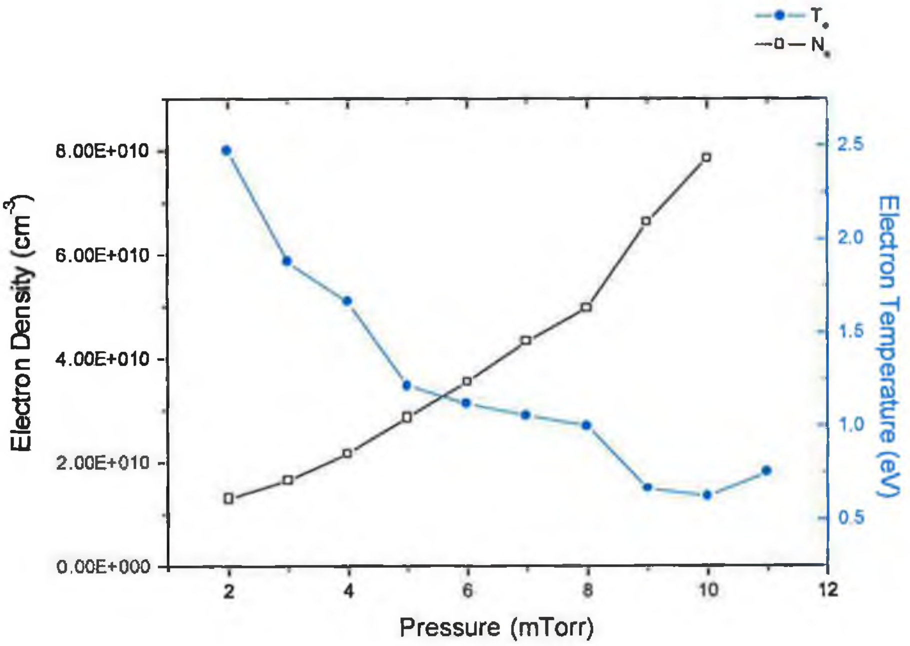

Fig. 4.3 **Variation in Electron Density and Electron Temperature with Pressure in a 1 A Discharge.**

As can be seen from the above graph in Fig. 4.3, the electron density increases with increasing pressure. This is due to the fact that there is an increased number of ionising collisions between electrons and neutral molecules as the neutral molecule density increases. This is easily observable from the following equations.

The gas density can be computed directly from the filling pressure, where

$$n_g = 3.5 * 10^{13}\, molecules / cm^3 \quad per \quad mTorr$$

The primary electron density is given by

$$n_p = \frac{I_d}{eV}\left[\frac{1}{n_g\langle\sigma_\varepsilon u_p\rangle + \frac{1}{\tau_w}}\right] \qquad \textit{Equation 4.1}$$

where, I_d is the discharge current, V is the volume of the discharge, $n_g\langle\sigma_\varepsilon u_p\rangle$, is the loss rate due to inelastic collisions, τ_{in} and τ_w is the characteristic loss time due to wall collisions

For low source pressure, where losses to the wall dominate, i.e.$\tau_w < \tau_{in}$, n_p is proportional to the discharge current and can be approximated to

$$n_p = \frac{I_d}{eV}\tau_w \qquad \textit{Equation 4.2}$$

Therefore it is possible to determine the value of τ_w by plotting n_p against I_d. As the pressure is increased, τ_{in} begins to dominate over τ_w. In this region the density and EEDF of the primaries are dependent on n_g. As n_g increases, n_p decreases, and as the mean free path for collisions becomes smaller the primary electron energy decreases to lower energies resulting in an increase in the bulk electron density, n_e. The bulk electron density can be computed by,

$$n_e = n_g n_p \langle \sigma_{ion} u_p \rangle \tau_e$$ *Equation 4.3*

or in terms of the discharge current and pressure,

$$n_e = \frac{I_d n_g \langle \sigma_{ion} u_p \rangle \tau_e}{eV \left(n_g \langle \sigma_\varepsilon u_p \rangle + \frac{1}{\tau_w} \right)}$$ *Equation 4.4*

where τ_e is the characteristic loss time for electrons.

The electron temperature also falls rapidly with increasing pressure. This decrease is due to the increasing density of neutral molecules. As the ionisation rate increases, the electrons undergo more collisions therefore transferring their energy to the ions and neutrals and hence lowering the electron temperature.

A radial scan of the electron temperature and density show the effect of the magnetic field distribution on the radial profile of the discharge. As can be seen in Fig. 4.4 the electron density rises slowly until at 3 cm from the chamber wall and then falls rapidly on moving closer to the grounded chamber wall. The decrease in the electron density in this region of the plasma is due to the sheath at the chamber wall and also the confining effect of the magnetic field. The applied field has the effect of confining the hot electrons in the centre of the discharge.

The electron temperature is also seen to fall on approaching the grounded wall from the centre of the discharge. This again is an effect of the confining field of the permanent magnets placed on the outer walls of the chamber. As only the colder, slower electrons can traverse the magnetic field the overall electron temperature is lower in this region

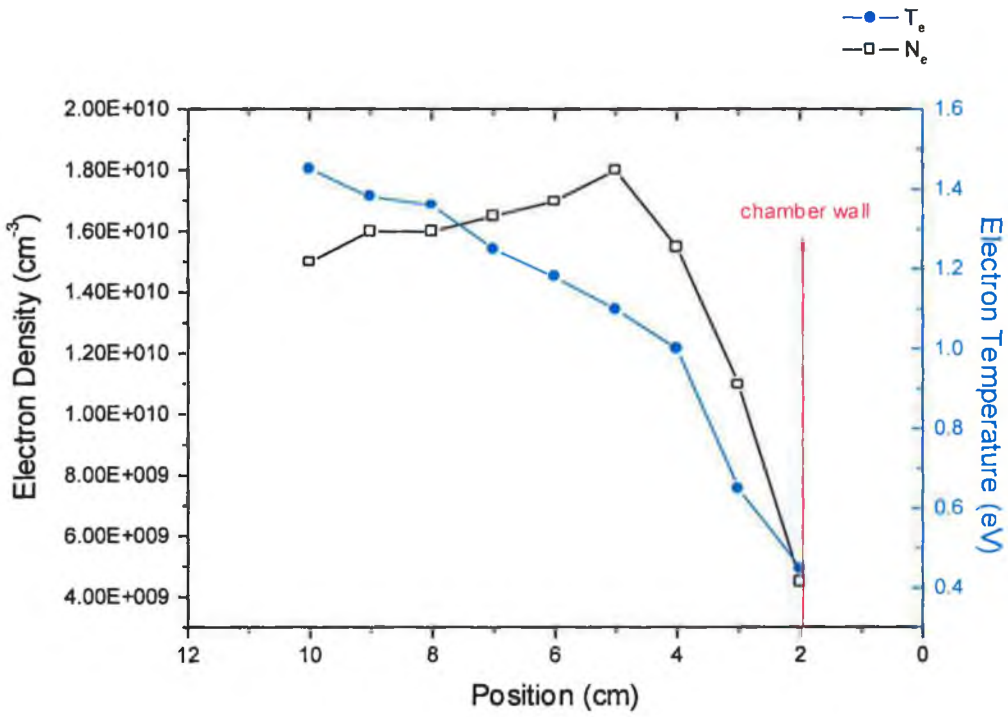

Fig.4.4 **Variation of Electron Temperature and Electron Density with Radial Position in the Source for a 70V, 1 A, 5 mTorr Discharge.**

(note: center of discharge at 12 cm on x-axis.)

4.3 EEDF Measurements in the DC Ion Source

Electron energy distribution functions were determined also by use of the Langmuir probe technique described earlier. Fig. 4.5 below shows the EEDF collected for a 5 mTorr hydrogen discharge with a discharge current of 1.5 A and a discharge voltage of 70 V.

The EEDF shows a strong bi-maxwellian tendency, which can be considered as the sum of two different maxwellian distributions given by the following equation:

$$f(v) = n\left(\frac{m}{2\pi kT_e}\right)^{3/2} \exp\left(-\frac{mu^2}{2kT_e}\right) \qquad \textit{Equation 4.5}$$

Each of the distributions is characterised by a different electron temperature, T_1 and T_2. The two different temperatures correspond to a colder distribution of electrons and a hotter distribution of electrons. On the graph shown in Fig. 4.5 the value of the two different temperatures are calculated. This is done by fitting a line to each component of the graph with a natural logarithimic scale. The temperature is then determined by calculating the slope of the line, where the slope is the reciprocal of the temperature.

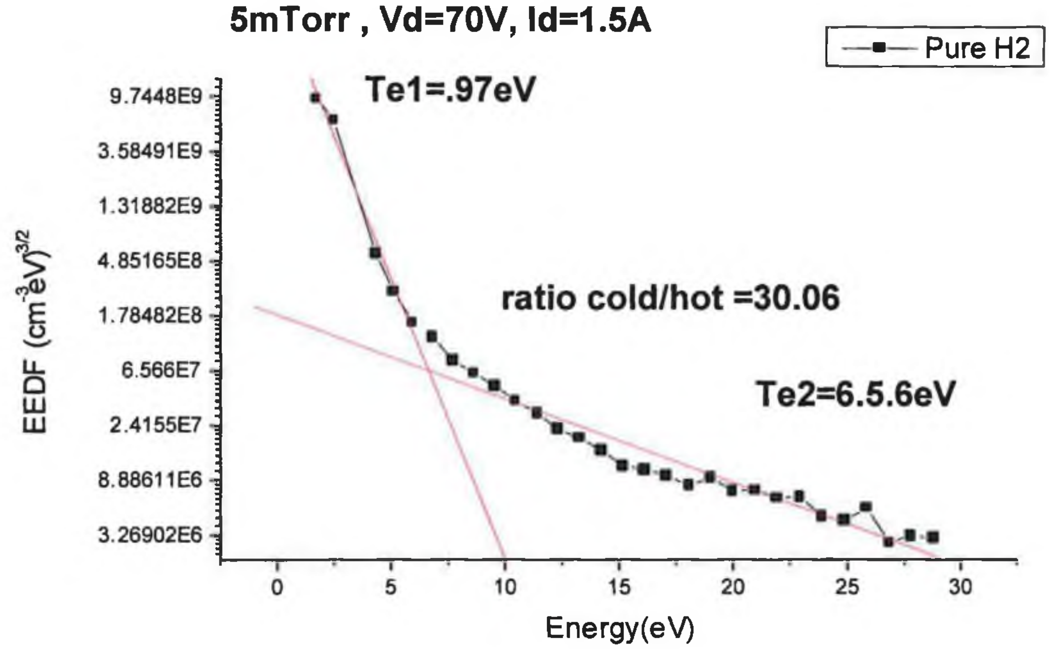

Fig. 4.5 **EEDF Measurements in a 5 mTorr, 1.5 A discharge.**

In this discharge (5 mTorr, 1.5 A) the colder distribution is calculated to have an electron temperature of 0.97 eV as T_1 and the hotter distribution, T_2, is calculated to have an electron temperature of 6.56 eV. The electron density in each distribution can also be calculated by integrating under each separate distribution. This then leads to the determination of the ratio for the density of the hot to cold electrons. In the discharge above, the cold distribution has an electron density of about 2×10^{11} cm^{-3} and the hot distribution has an electron density of approximatively 1.3×10^{9} cm^{-3}. The ratio of densities is found to be 30:1 for the "cold to hot" ratio.

4.4 Measurement of Plasma Parameters in the RF Ion Source

Typical I-V characteristics are shown in Fig.4.6 from the discharges generated in the RF ion source. These characteristics are collected from a plasma source without the permanent Co-Sm magnets on the outer wall of the source. To determine the effect of the magnetic field on the discharge, all the source plasma parameters were first measured without an external field and then re-determined when the magnetic field was re-applied,.

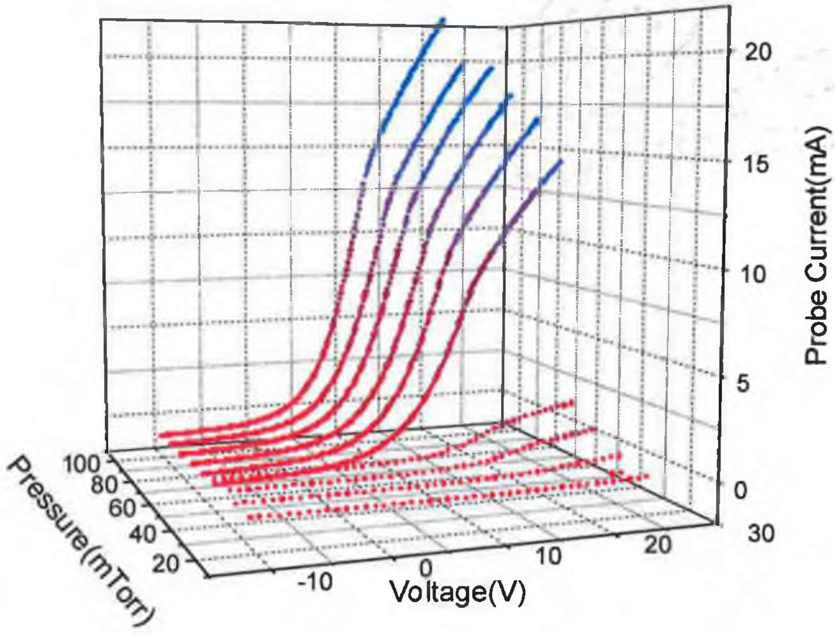

Fig. 4.6 **Variation of I-V Characteristics Collected in the RF Ion Source as a Function of Pressure (RF Power 550 W).**

The variation in the electron density as a function of the source pressure and the source RF power is shown in the following graph in Fig. 4.7. From this graph the transition from the capacitive (E-mode) to the inductive mode (H-mode) can be clearly seen. The transition is seen from the increase in the electron density, approximately a factor of 10 increase. This transition occurs however only at pressures above 30 mTorr. For the powers used, it was not possible to generate the inductive discharge for pressures below 30 mTorr.

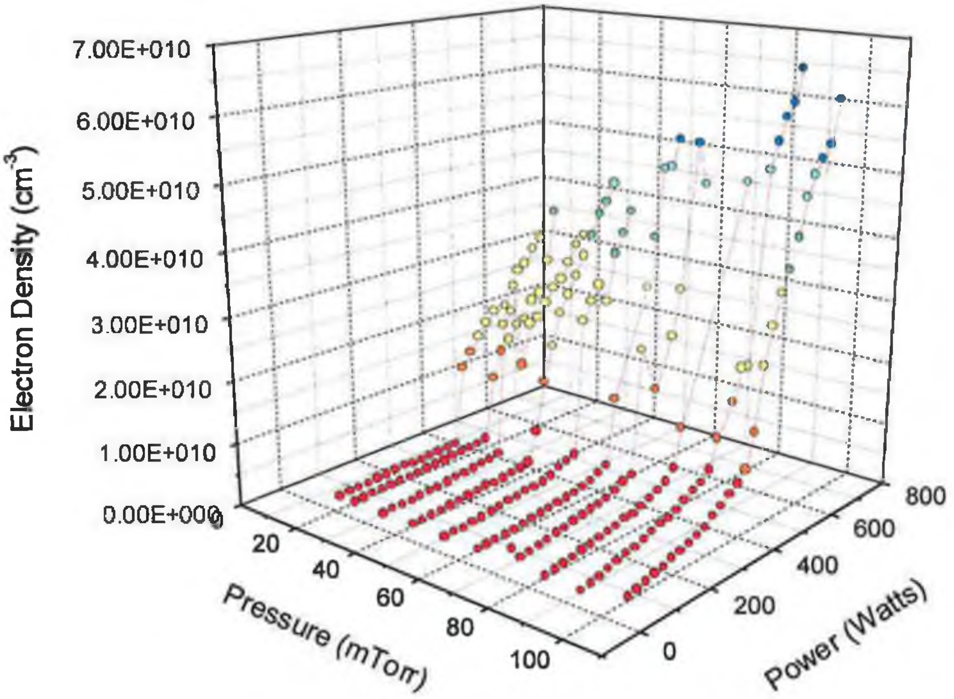

Fig. 4.7 **Variation of the Electron Density with RF Power and Pressure.**

The electron density increases with increasing gas pressures as there are more neutrals available for ionisation.

The variation in the electron temperature with pressure can be seen in the following graph in Fig.4.8 below.

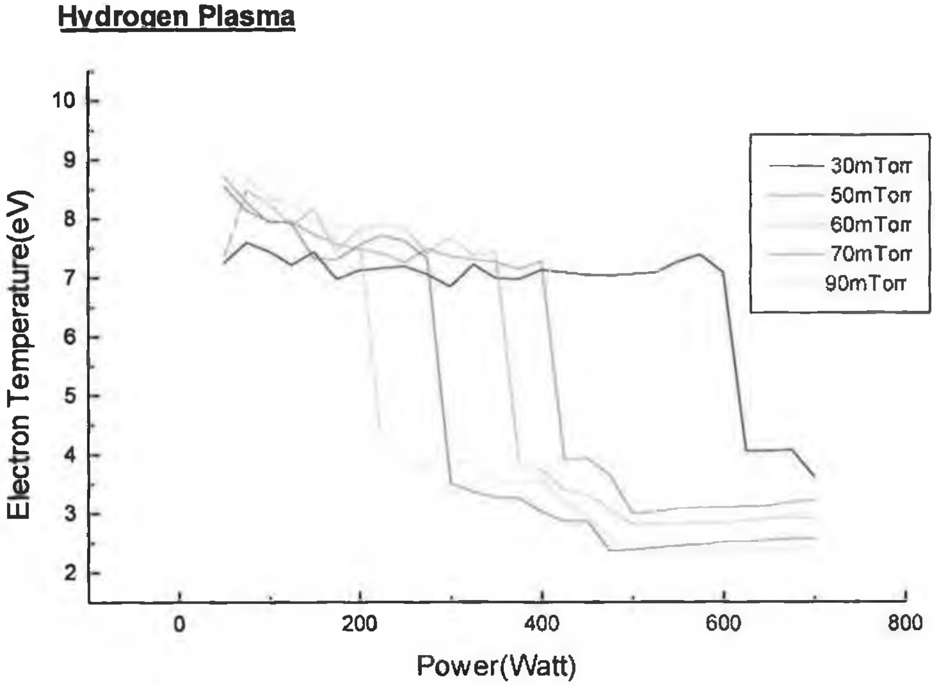

Fig. 4.8 Variation in the Electron Temperature with Power and Pressure.

As can be seen in Fig. 4.8, on transition from the E-mode to the H-mode the electron temperature decreases dramatically.

Fig. 4.9 shows the EEDF's collected and their variation with pressure. The distributions show little variation with pressure. The profile obtained at 20 mTorr is different as the discharge has not transversed to the inductive mode and remains capacitive.

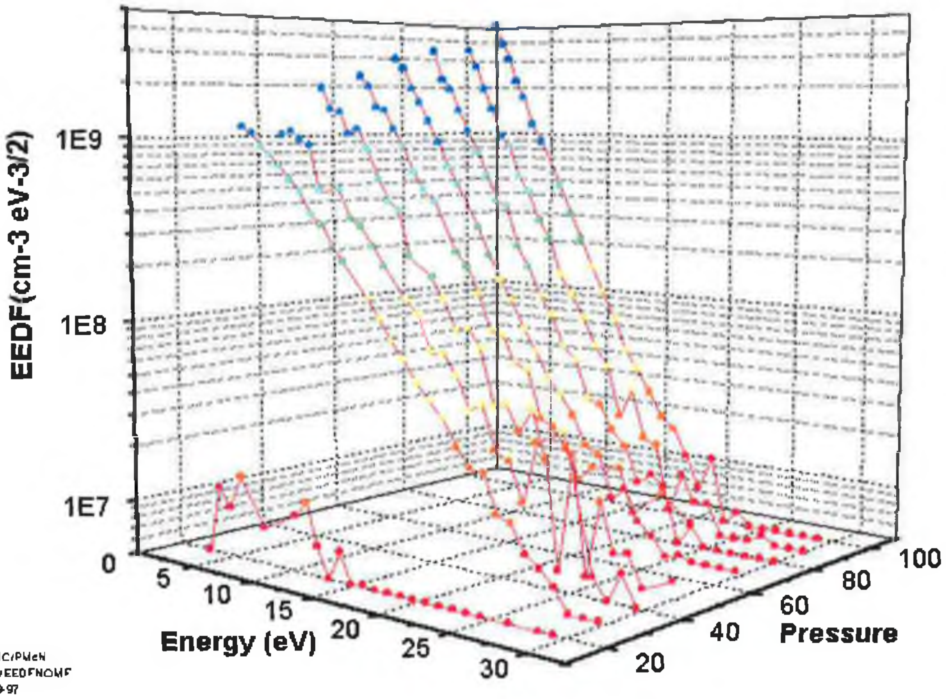

DB/NC/PMcN
700WEEDFNOMF
23-09-97

Fig. 4.9 **Variation in EEDF Profile with Pressure for a 700 W Discharge**

4.5 Magnetic Confinement of Plasmas

Multicusp-like geometries have been proposed and studied since the early days of fusion research, when cusp and picket fence geometries were proposed and analysed. [1] The initial motivation was a search for magnetic field configurations with "good" curvature, i.e. the radius of curvature is antiparallel to the pressure gradient rather than parallel. Magnetic fields are often used to both confine and increase ionisation within the discharge. In multicusp ion sources, fast electrons are prevented from recombining with the chamber walls by a strong multipole arranged magnetic field.

Electrons travelling with velocity u parallel to the field will be unaffected since the product of $u \times B$ will be equal to zero. However electrons ravelling at an angle, θ, will be subject to a force perpendicular to the field. This force is determinedby

$$F_{\perp} = Beu \sin\theta \qquad \textit{Equation 4.6}$$

If the electron makes no collisions it will move with circular motion around the magnetic field with a radius of

$$r = \frac{m_e u \sin\theta}{Be} \qquad \textit{Equation 4.7}$$

combining this motion with its velocity, $u\cos\theta$, parallel to the magnetic field results in helical motion of the electron. This effect serves to increase the electron mean free path, m.f.p., and therefore decrease the net velocity of the electrons towards the walls, thus decreasing the rate of recombination losses. The other advantage of increasing the m.f.p. is that there is more ionisation and excitation of the neutrals through the increased collisions which, in turn, allows the operating pressure of the system to be reduced. This section serves to examine experimental results on the effect of the application of a multipole field to a low pressure RF hydrogen generated plasma, in particular the effect on the density and electron temperature.

4.5.1 Experimental Setup

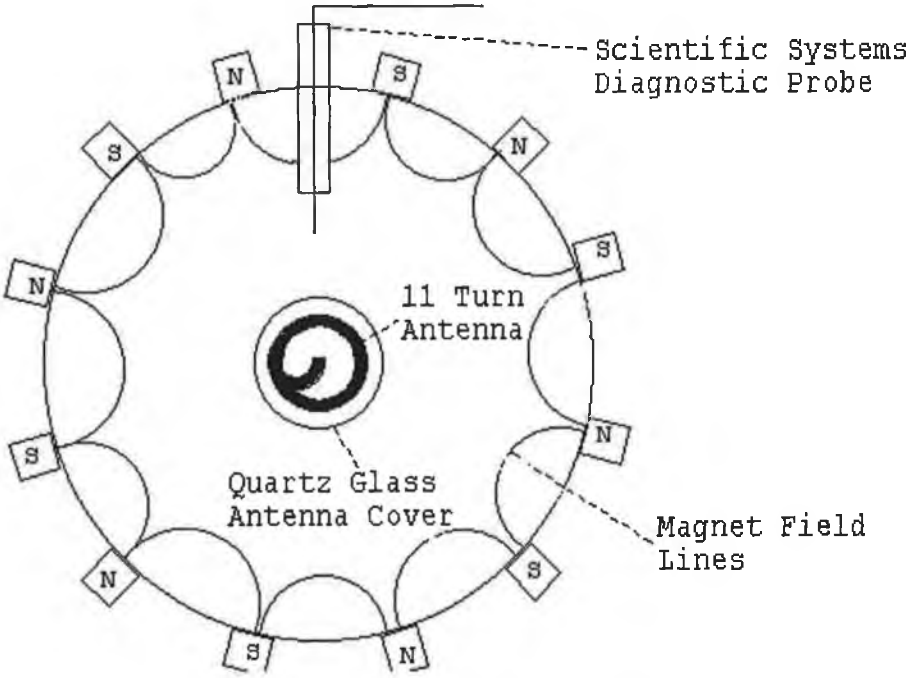

Fig. 4.10 Magnetic Field Configuration of the Ion Source.

The magnetic field configuration is shown in Fig. 4.10 above. Twelve Sm-Co bar magnets were aligned around the outside of the ion source chamber. The twelve magnets were evenly spaced around the circumference of the chamber. The multipole field was generated by facing the bar magnets alternatively north and south towards the plasma giving the multipole cusp geometry. A Hall effect magnetometer was used to measure the magnetic field strength within the chamber and the tuned Langmuir probe described previously used to measure the plasma parameters and the EEDF's. The Larmor radius of the electrons was verified to be greater than the probe radius allowing for the validity of the probe analysis. The plasmas investigated were generated in the RF ion source chamber that was described previously in Chapter Two. The field strength was found to be B>500G. The magnetic field generated by the externally aligned permanent bar magnets was modeled with the POISSON and SUPERFISH progams. These were the main solver programs used out of a collection of codes for calculating static magnetic and electric fields or radio-frequency electromagnetic fields in either 2-D Cartesian coordinates or axially symmetric cylindrical coordinates. The programs generate a triangular mesh fitted to the boundaries of different materials in the problem geometry. [2, 3]

The resultant magnetic multipole cusp geometry modeled from the POISSONSUPERFISH programs are shown here in Figs. 4.11. Listings of the source code used to model the magnetic field geometry are given in Appendix A.

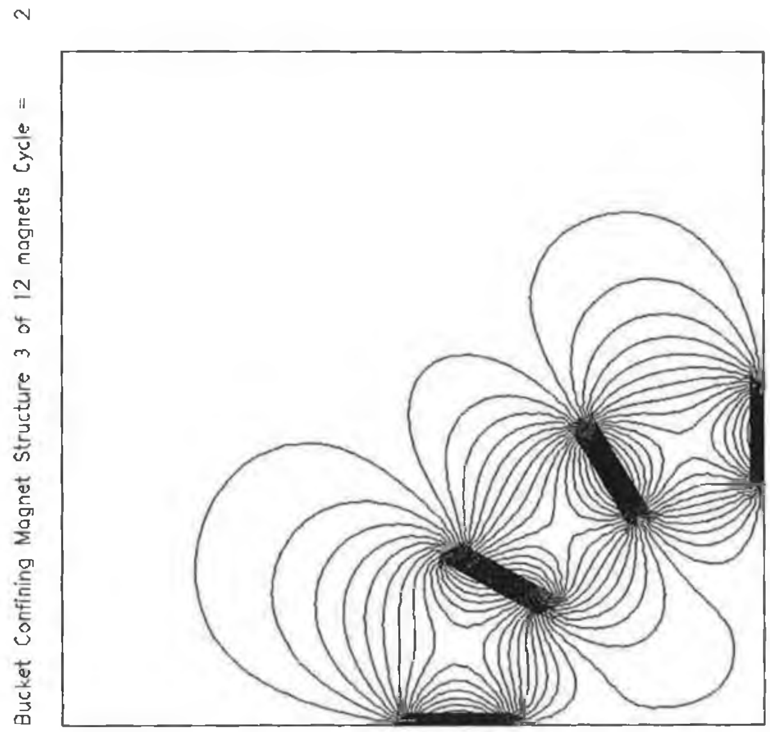

Fig. 4.11 **Model of Magnetic Field Generated by the POISSON-SUPERFISH Programme for one Quadrant of the Ion Source Chamber.**

In Fig. 4.11 the magnetic fields are shown for the second quadrant of the cylindrical ion source. A photograph of a hydrogen plasma generated in the RF powered source illustrates the effect of the magnetic field. The cusps generated by the modeled code can be readily seen from this photograph shown in Fig. 4.12. The photograph Fig. 4.13 illustrates the shape of the discharge when a magnetic filed is not applied.

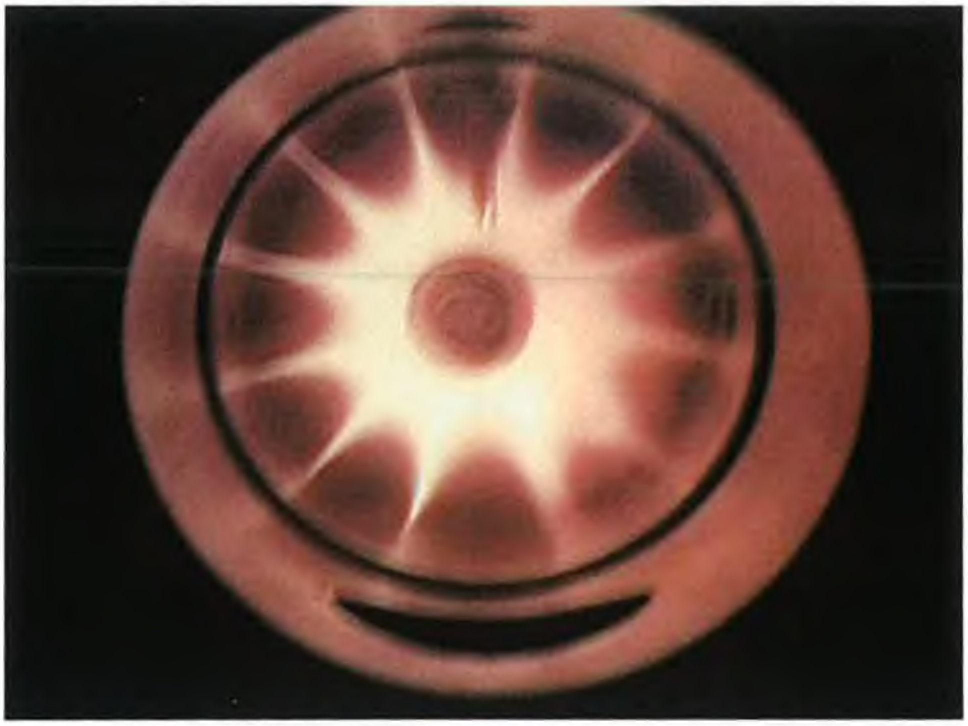

Fig. 4.12 Photograph of a D_2 ICP with External Magnetic Field Applied Generating a Multicusp Geometry.

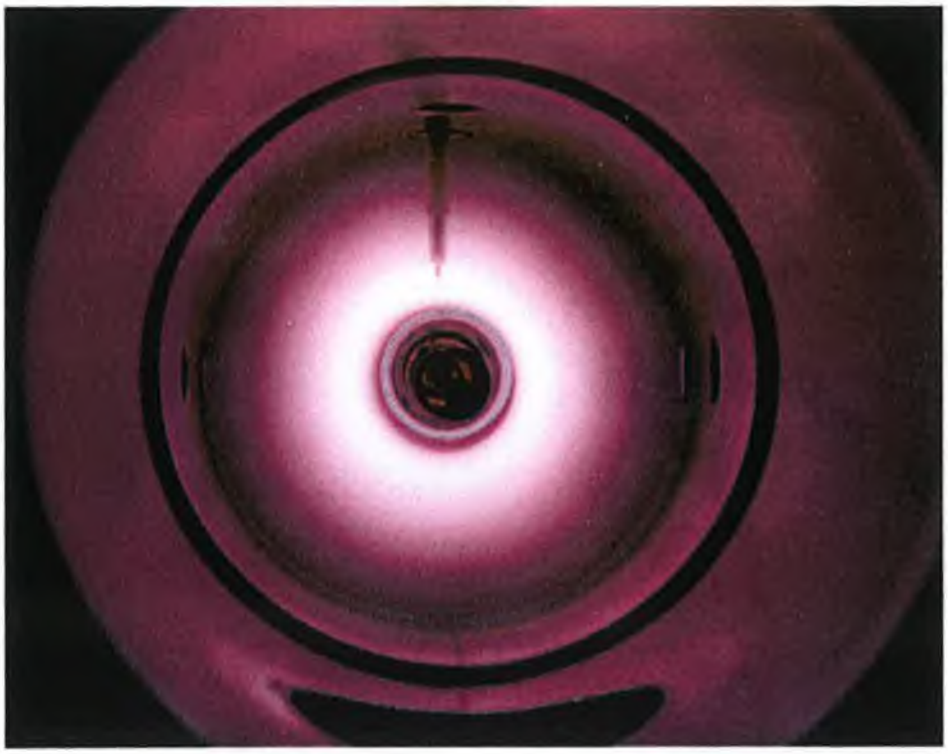

Fig. 4.13 Photograph of a H_2ICP without External Magnetic Field.

4.6 Plasma Parameter Measurements in a Magnetically Confined RF Discharge.

The effect of the magnetic field on the discharge is quite significant as can be seen from the following results. A dramatic increase in the electron density can be seen in the electron density when compared to the same discharge with no applied field. This can be seen in Fig. 4.14 below.

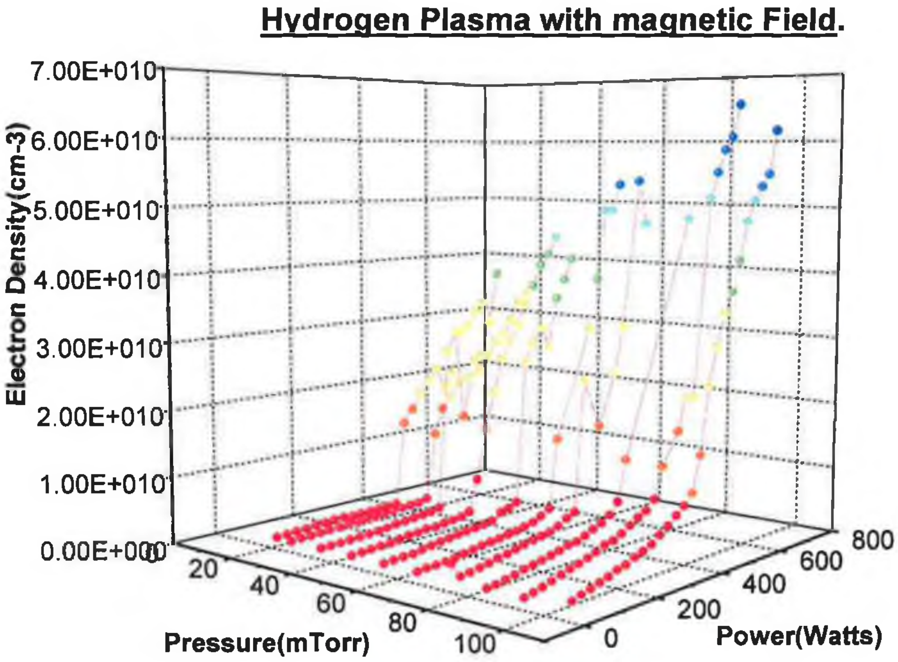

Fig. 4.14 **Variation in Electron Density with Source Pressure in a Magnetically Confined Discharge.**

From this graph it can be seen that the electron density values have increased. In the case of the 80 mTorr discharge the electron density increases from 3 x 10^{10} cm^{-3} when there was no magnetic confining field to 6.8 x 10^{10} cm^{-3} when the field was applied. This is an increase in density of a factor of 2. For the 40 mTorr discharge the density rises from 1.7 x 10^{10} cm^{-3} to 4.42 x 10^{10} cm^{-3}. For the 20 mTorr discharge the increase is from 3.7 x 10^{10} cm^{-3} to 4.7 x 10^{10} cm^{-3}.

As can be seen, it now was possible to generate an inductive discharge under 30 mTorr when the confining field was applied. This was not the case previously and the plasma remained capacitive. From the above graph it is also obvious that the transition from capacitive to inductive occured at about 400 W, while when there was no external field the transition occured over a range of powers, i.e. from 450 for 100 mTorr up to 750 W for the lower pressure of 30 mTorr. Hence it can be said that the effect of the magnetic field results in requiring lower powers to generate an inductive discharge. The transition between E and H modes is seen as a function of power in the following graph when a magnetic filed is applied, Fig. 4.15

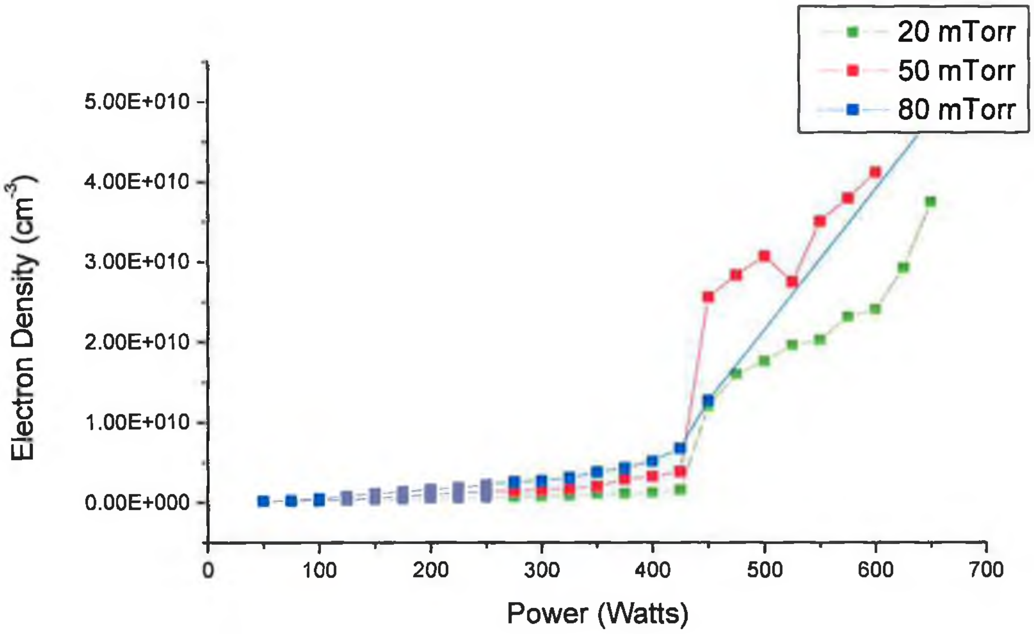

Fig.4.15 **Transition Between E and H Modes as a Function of Power with an External Magnetic Field.**

4.6.1 Radial Measurements

The magnetic field also alters the radial profile of the electron temperature and the electron distribution. In the center of the discharge there are a lot of hot electrons but on moving towards the chamber walls, only the slow, cooler electrons may traverse the magnetic filed into the strong field regions. This is clearly visible in the following Fig. 4.16. The fall-off in the electron density on approaching the wall can be seen in this graph. The hot energetic electrons are confined in the center of the discharge and the cooler electrons traverse the field into the high field regions. The effect of the magnetic filed on the ion density is also illustrated in Fig. 4.16: the ion density follows the electron density until approximately 40 mm from the antenna cover, where an increase is observed. It is assumed that the ion density should follow the decay of the electron density and that the difference is due to magnetic field effects on the probe, resulting in an overestimation of the ion density.

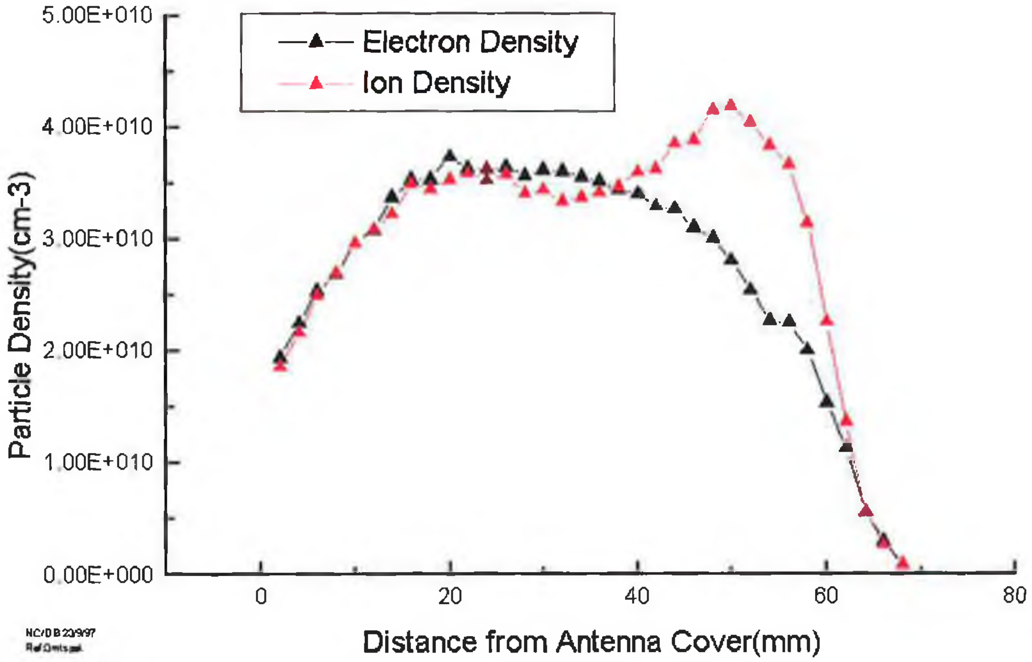

Fig. 4.16 **Radial Variation of Particle Densities in a 3 mTorr 1200 W Hydrogen Discharge with Magnetic Confinement.**

A radial variation of the EEDF collected in this discharge is also shown below in Fig. 4.17. A ratio of hot / cold electrons is estimated and plotted in Fig. 4.18. Hot electrons were taken to be approximately 18 eV and cold electrons about 6 eV. The variation in this ratio as a function of the radial position from the antenna is shown.

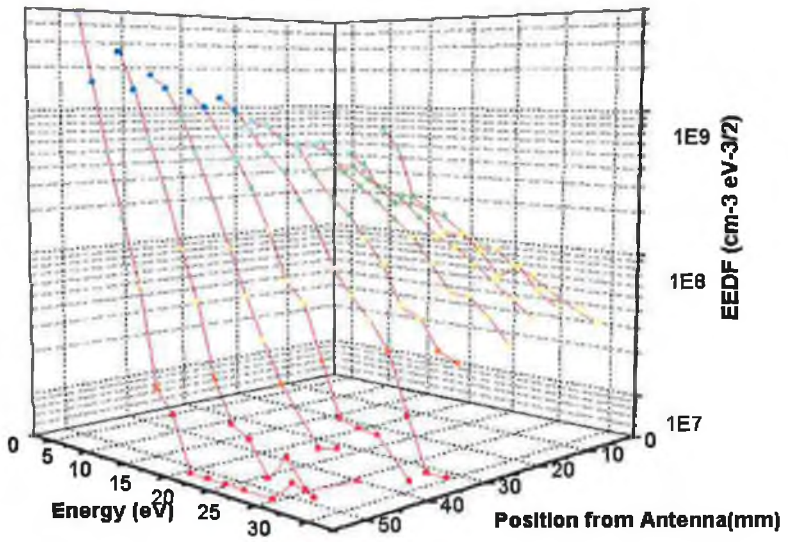

Fig. 4.17 **Variation of EEDF with Radial Distance in the Source with a Magnetic Confining Field (1200 W , 50 mTorr discharge).**

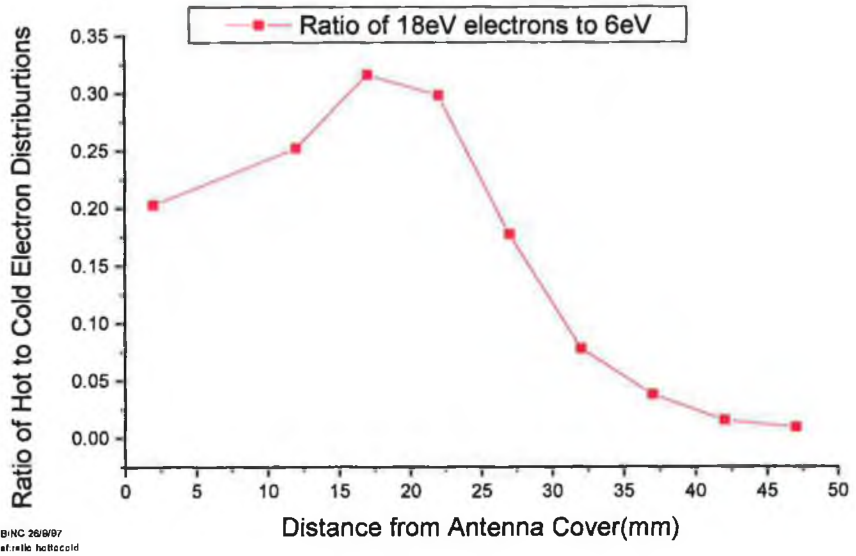

Fig. 4.18 **Radial Variation of the Ratio of Hot to Cold Electrons in a 3 mTorr, 1200W Discharge with External Confining Magnetic Field.**

4.7 Pulsed Plasma Parameter Measurements

As discussed previously in Chapter One, it has been found that the main destruction mechanism of negative ions is caused by fast, energetic electrons in the electron detachment reaction, which is found to have a reaction rate of approx. 10^{16} cm^2. [4, 5, 6] In order to suppress the energetic electrons which can destroy the H, the discharge was temporally pulsed. An outline of the concept of a temporal filter is discussed here.

When the power to a discharge is turned off the fast electron density has been shown to decay away in less than 1 μs [7]. This is due to the short confinement time of fast electrons [8]. However, the vibrationally excited molecules have a relatively long life time and are destroyed only after several wall collisions [9] which means that they survive well into the post-discharge. It has also been presented that the thermal electrons survive well into the post-discharge, typically 30 μs. [8] This leads to the conclusion that H^- can be produced even in the post discharge. A pulsed discharge can be compared to the tandem source, where the discharge is divided into two distinct regimes, the driver region is when the plasma is on and the extraction region is when the discharge is off.

It has been shown that for low pressure discharges, with a filter field placed close to the plasma electrode, that during the discharge the conditions are similar to that in a tandem driver region. [7]. There are two populations of electrons, a thermal group (~90 %) and a high energy group (~10 %). The E-V process takes place , but because of the high energy electrons and the rate coefficient for CD , given as 1.8 *10 -7 cm3/s, there are a lot of losses to the negative ion density. Because the electron temperature is high the DA rate coefficient is quite low, given as $1.3*10^8$ cm^3/s. These conditions are similar to those described in Chapter One for the tandem driver region. When usinga temporal filter the on period can be termed as the driver region of the cycle.

When the discharge is switched off, the extraction period of the cycle comes into play. Hopkins et al have shown that the EEDF have cooled significantly, $kT_e = 0.44$ eV afer 50 μs into the post-discharge. The fast electrons disappear and the EEDF becomes maxwellian. In this temporal area the electron density does not decay significantly and assuming that the vibrational states have a long lifetime as shown by Lefebvre to be typically 1ms [10]. The population of the vibrationally excited molecules is similar to that of the steady state discharge, the production of H is expected to continue in the post-discharge. Having no fast electron the main destruction mechanism of CD will decrease dramatically. The rate coefficient for DA increases with decreases kT_e and reaches a peak of $2.9*10^{-8}$ cm^3/s in the post-discharge. Therefore an increase in the density of negative ions is expected to be detected. The temporal filter operates in much the same way as the tandem source except the filter is produced by pulsing the discharge on and off rather than by the application of a magnetic confining filter field.

The temporal filter can be operated more efficiently at lower pressures than the tandem source, especially at lower pressures where the electron temperatures are very high in this region and therefore the cooler post-discharge will result in larger enhancements in the negative ion yield. The temporal filter also gives control over the EEDF's.

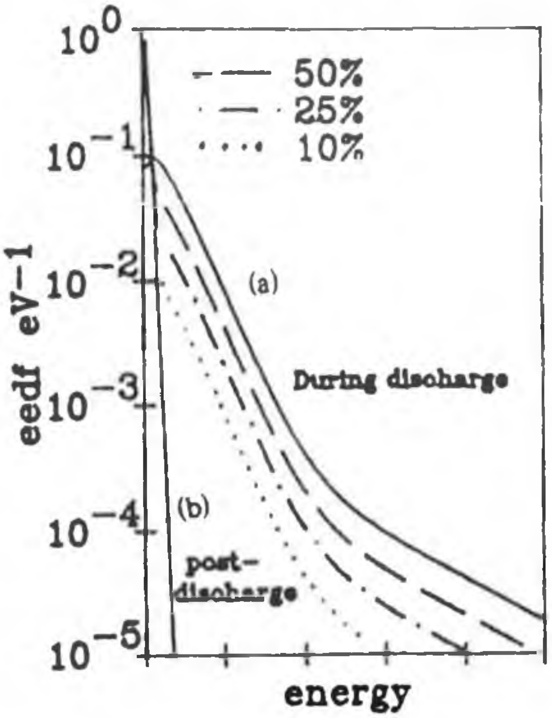

Fig. 4.19 **Control of the Time Averaged EEDF by Variation of the Duty Cycle [11].**

Fig 4.19 above shows the EEDF for a typical continuous discharge [11]. As the duty cycle is decreased from 100 % to lower percentage "on times", the high energy part of the time averaged EEDF will decay away almost linearly, while the low energy portion will increase as the bulk electrons become even more predominant. Thus by variation of the modulation frequency and the duty cycle the appropriate time averaged EEDF can be chosen for the parameter régime required.

4.7.1 Temporally Modulated RFDischarge Plasma Parameter Measurements

In this section the RF, 13.56 MHz discharge is power pulsed at high frequencies, up to 5 kHz, leading to the determination of the plasma parameters by use of a Langmuir probe. Electron temperatures, densities and EEDF's are investigated in both the discharge and the afterglow. It is found that a relatively high particle density, 10^{10} cm^{-3} is sustained in the afterglow, while the electron temperature decreases dramatically, <1 eV, on switching off of the RF power. EEDF's collected thermalize in a maxwellian distribution even in the late afterglow. These measurements were collected by the use of the Langmuir probe discussed in Chapter Three.

4.7.2 Experimental Set-up

The probe used in this work is a Scientific Systems SmartProbe[12]. The probe is operated within the pulsed discharge in boxcar mode. The RF power supply in use allows for pulsing of the discharge with a frequency of up to 1 MHz. The modulation frequency of the discharge is sent through delay electronics to produce an external trigger to the SmartProbe system and therefore I-V characteristics and EEDF's can be collected at a specific point in the pulse train of the discharge or afterglow.

Some care needs to be taken when using electrostatic probes in pulsed plasmas,in particular during the post discharge. The Debye length increases as the time in the afterglow increases. In the studies presented here, the electron density drops from 10^{11} cm^{-3} at the beginning of the post-discharge to about 10^{10} cm^{-3} in the late afterglow. At the same time the electron temperature decreases from 5 eV to 0.5 eV. From this the Debye length can be determined and it is found that it varied from 4.4 x 10-7 m up to 3.5 x 10-6 m in the early afterglow. This indicates a limit of validity for the probe measurement in the afterglow when working on a pulsed plasma at 20 mTorr.

In this study the probe is placed 2 cm from the quartz tube. The variation of the electron density and electron temperature during the discharge and the post discharge are plotted as a function of time and shown in Fig. 4.20.

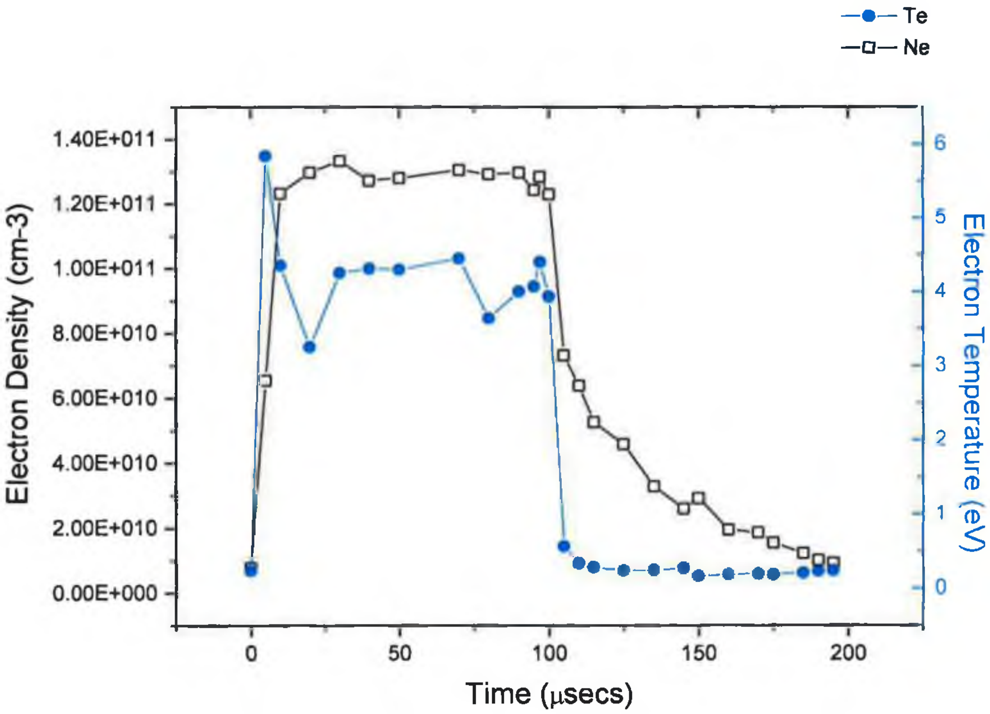

Fig. 4.20. **Variation in the Electron Density and Electron Temperature in the Discharge and Post-Discharge of a 1500 W, 20 mTorr H_2 Plasma (200 μs pulse).**

It is observed that the electron density in the discharge régime reaches a stationary value, about 10 μs after the discharge breakdown. This is independent of the applied power.

Under these experimental conditions, 20 mTorr, 50% duty cycle, 5 KHz pulsed discharge, with powers ranging form 1 kW to 2 kW, the stationary values ranges from1×10^{11} cm^{-3} up to 1.8 x 10^{11} cm^{-3} and increases with increasing applied forward power.
The variation of the electron density in the afterglow is shown in Fig. 4.21.

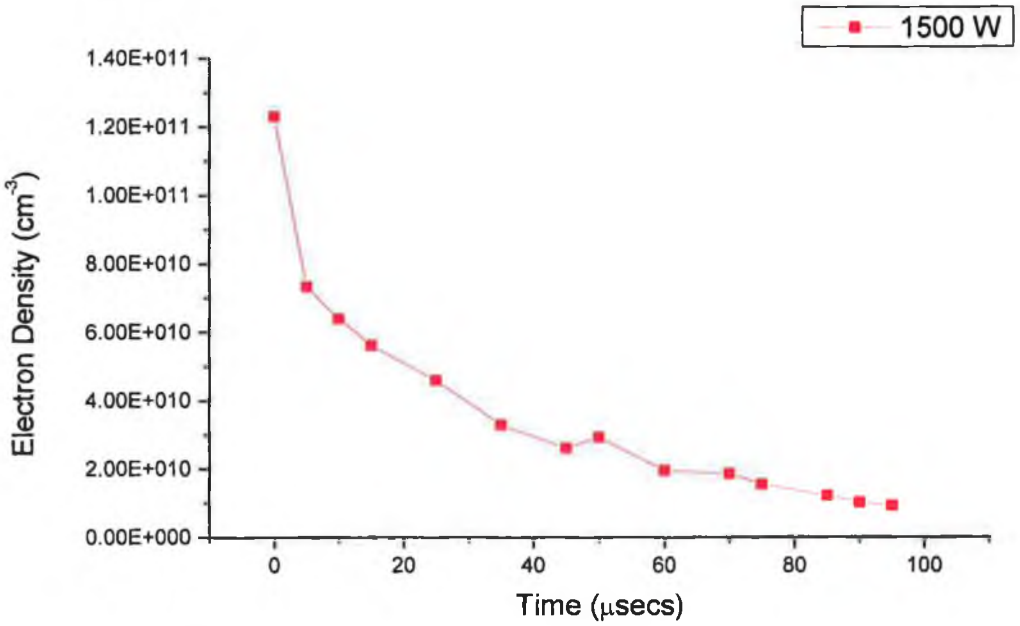

Fig. 4.20 **Decay of Electron Density in the Afterglow as a Function of Time in a 1500 W, 20 mTorr, 200 μs Pulse.**

The main electron loss process at this pressure is ambipolar diffusion. In this case the electron density decay in the afterglow can be written as:

$$n_e(t) = {}^{n_{e(0)}}\Big/_{\alpha n_{e(0)} t} \qquad \textit{Equation 4.8}$$

where $n_{e(0)}$ is the electron density at the beginning of the afterglow and α is the decay co-efficient, the ambipolar diffusion co-efficient. The variation of electron density with time in the afterglow is confirmed by a linear plot of the logarithm of the electron density versus time from which the decay co-efficient can be evaluated. It is found to be ~ 100 μs. Doing the same with data measured in higher power discharges under the same conditions give the same values. This can be seen in the following graph in Fig.4.22

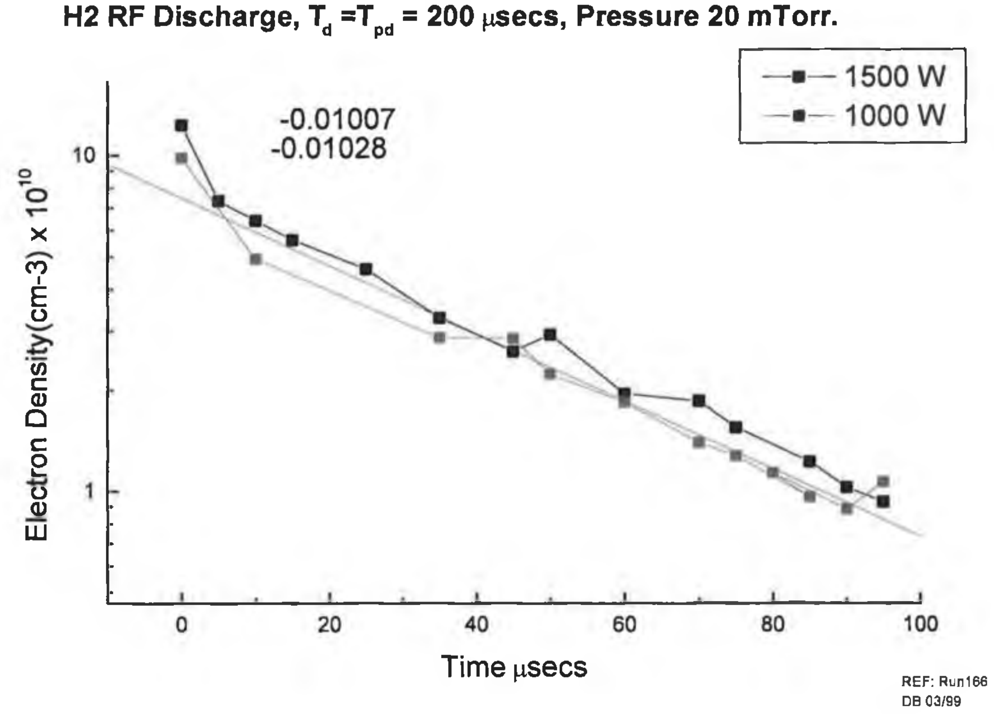

Fig. 4.22 **Logarithmic Plot of Electron Density in the Afterglow as a Function of Time in a 1500 W, 20 mTorr, 200 μs Pulse.**

The floating potential V_f can be obtained by simply measuring the potential reached by the probe when no external polarization is applied to it. During the discharge régime, the measure of the floating potential yielded the time needed for the plasma to reach a stationary state and gives information about the stability of the discharge. During the post-discharge the variation of V_f with time leads to the determination of the real afterglow duration, that can be defined as the time during which charged species remain in the gas phase, that is when the V_f does not reach zero.

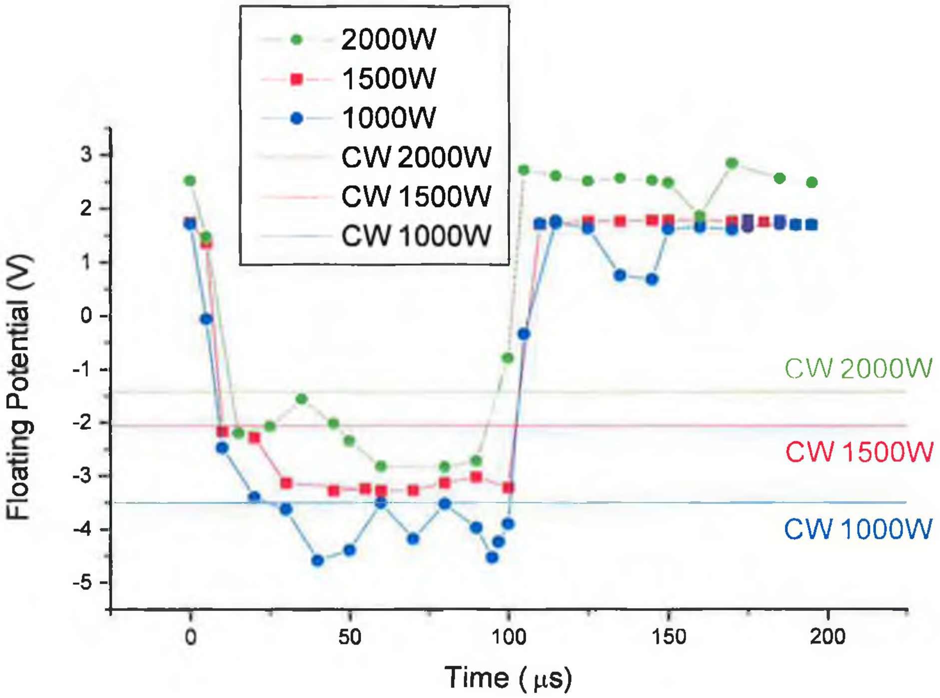

Fig. 4.23 **Variation of Floating Potential with Time in the Discharge and Post-Discharge of a 20 mTorr, 200μs Pulse Train**

From the measurements carried out on V_f, Fig. 4.23, we can see ~20μs stability time required for discharge breakdown. The plasma is then stabilized for the duration of the discharge but once into the aftergflow the floating potential becomes positive and never seem to go to zero. This confirms what we said earlier about the plasma not actually turning off at this frequency.

4.7.3 Determination of the EEDF in the RF Temporally Modulated Discharge

Figs. 4.24 and 4.25 below show the EEDF's collected in a 1000 W discharge at 20 mTorr, in a 20 μs pulse train. In Fig. 4.24 the EEDF's are shown as a function of time in the post-discharge. Fig. 4.25 below this shows the EEDF collected in the discharge, in the first 100 μs of the pulse train.

Temporally modulating the discharge then has the effect of allowing control over the EEDF. This is achieved by having an "on" period of a hot plasma, followed by having a cooler discharge, the post discharge, in the "off" period. This results in having a time averaged EEDF that can be changed simply by changing the pulse duration and duty cycle of the pulse. Fig. 4.26 below shows the variation in the EEDF with the alteration of the duty cycle.

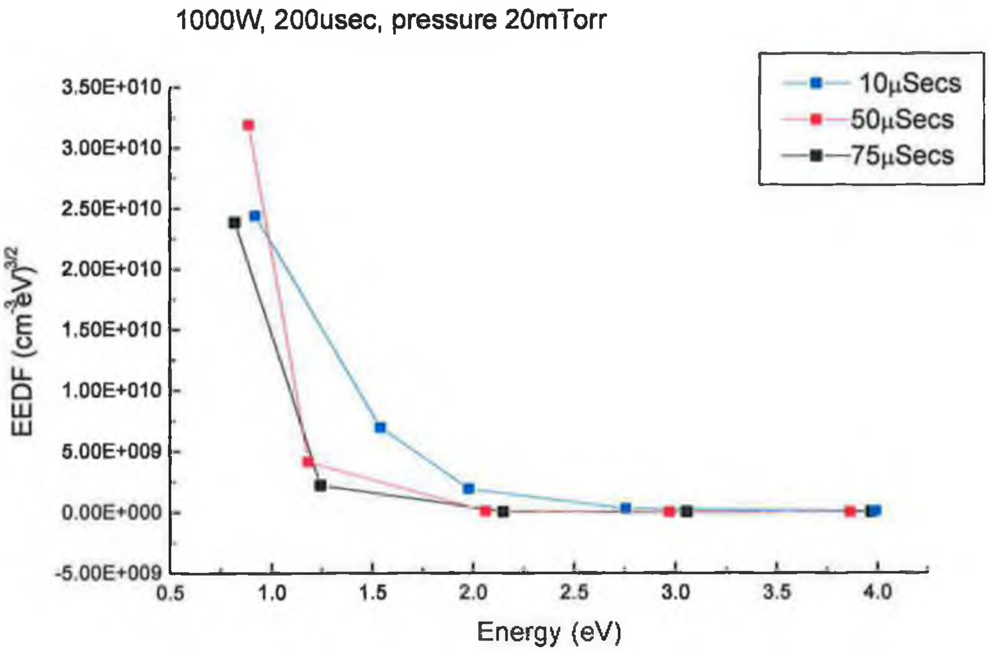

Fig. 4.24 EEDF's Collected at Different Times in the Post-Discharge in a 1000 W Discharge with a Pulse Train of 200 μs at 20 mTorr.

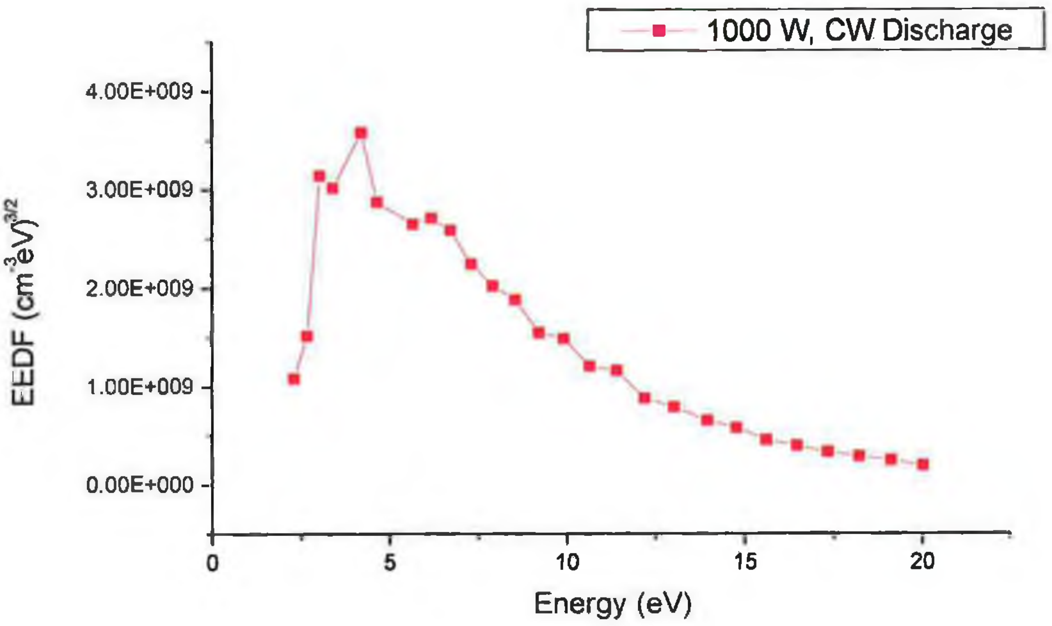

Fig. 4.25 EEDF Collected in the Discharge of a 1000 W, 20 mTorr, 200 μs Pulse Train

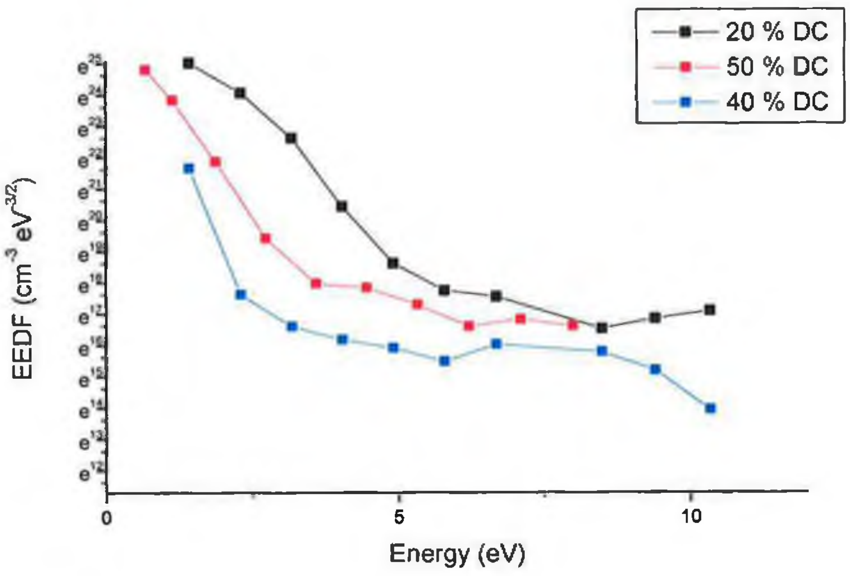

Fig. 4.26 Variation in EEDF Profile with Change in Duty Cycle for a 200 μs Pulse Train (1500 W , 20 mTorr discharge).

This can be seen in the the following graphs also, where the effect of the variation of the duty cycle is investigated with respect to the electron density and the electron temperature, Figs. 4.27 and Fig. 4.28.

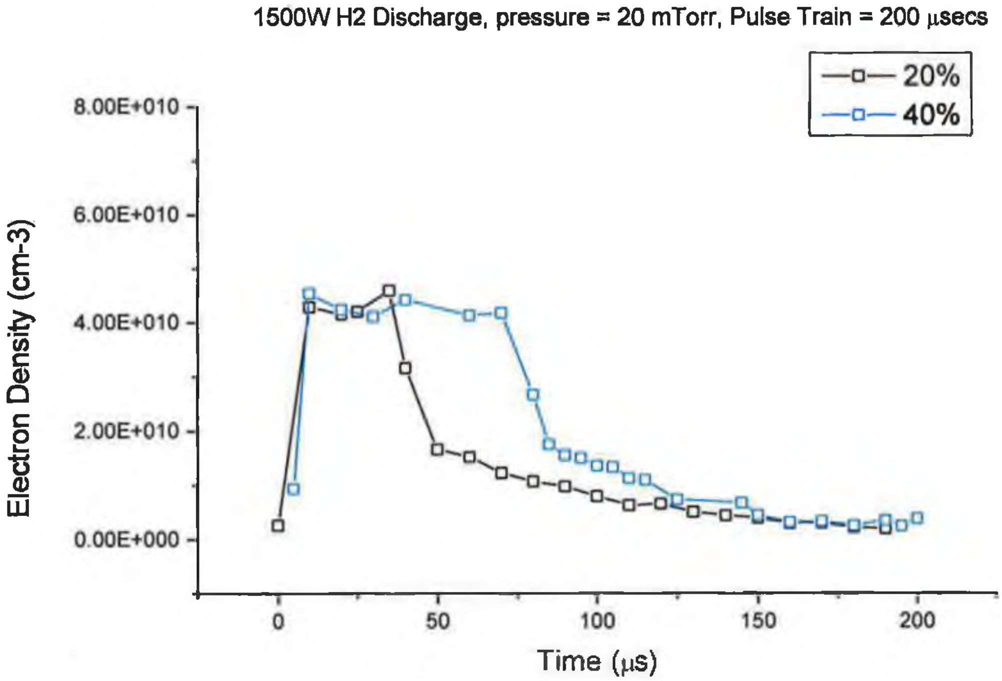

Fig. 4.27 **Variation of Electron Density with Duty Cycle in the Afterglow**

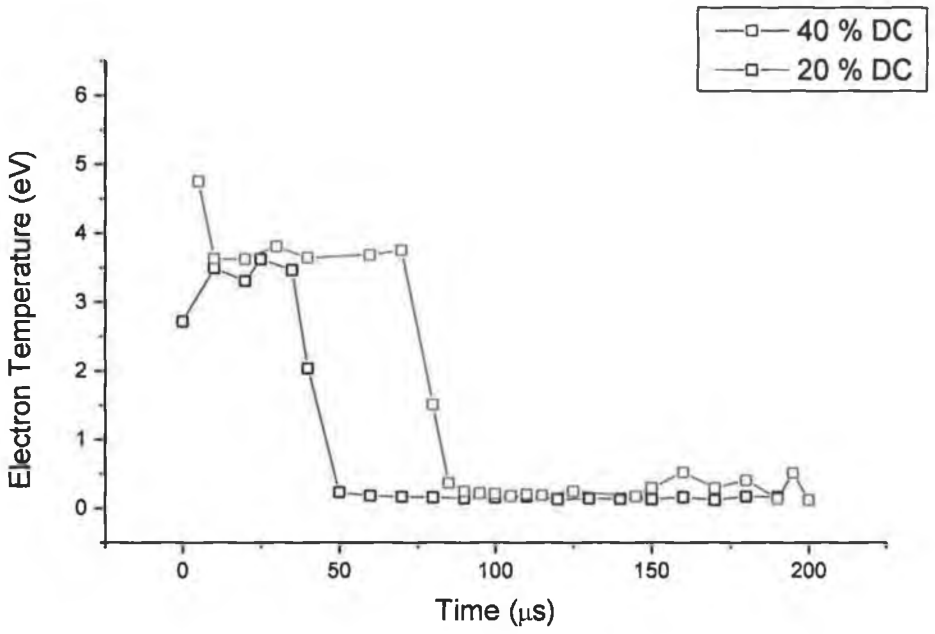

Fig. 4.28 Variation of Electron Temperature with Duty Cycle in the Afterglow.

4.8 Conclusion

The DC and RF discharges were characterised with the use of a Langmuir probe. All plasma parameters were determined over a range of pressures and powers when operating both systems in continuous modes. It was seen that the application of an external magnetic field greatly increased the efficiency of the RF ion source, allowing higher plasmadensity for lower source pressures.

The magnetic field in the source was modeled with the use of the POISSONSUPERFISH programme. Radial measurements were determined in the plasma with a magnetic filed applied and the effect of the applied field on the plasma densities determined.

The concept of temporal modulation was examined, to determine the effect of pulsing the discharge on the plasma parameters. The SmartProbe operated in boxcar mode served as an excellent tool in the acquisition of all plasma parameters in the discharge and in the afterglow. Information on the electron densities and temperatures, the floating potential and EEDF's in the modulated discharge was collected. Relatively high electron densities were found in the afterglow and low electron temperatures. It was concluded that the decrease in the electron temperature would serve to effectively increase the reaction rate for

DA in the afterglow and hence lead to an increased yield of negative ion production in the post-discharge. The determination of the negative ion yield was carried out in the following Chapter 5.

References

[1] Bishop, A.S.,
Project Sherwood, Chapters 9 and 14, Addison-Wesley, 1958

[2] POISSON-SUPERFISH Group of Codes Manual, LAUR-87-126

[3] User's Guide for the POISSON-SUPERFISH Group of Codes, LAUR-87-115.

[4] Peart, B. and Hayton, D.
J. Phys. B: At. Mol. Opt. Phys. 25 p5109, 1992

[5] Dolder, K. and Peart, B.
Rep. Prog. Phys. 48 p1283, 1985.

[6] Mellon, K.N.
"Enhanced Production of Negative Ions in a Pulsed Volume Ion Source."
PhD. Thesis, Dublin City University, 1993.

[7] Hopkins, M.B.,
Journal of Applied Physics, 70 (4), p2009, 1991.

[8] Hopkins, M.B. and Graham, W,
Journal of Applied Physics, 69 (6), p3461, 1991.

[9] Hall, R.I., Cadez, I, Landau, M.,Pichou, F., and Schermann, C.
Physical Review Letters, 60 (4), p377, 1988.

[10] Lefebvre, M et al
Proc. Production and Application of Light Negatiev Ions
Paris, 1986.

[11] Hopkins, M.B.
4 th European Workshop on the Production and Application of Light Negative Ions, Belfast, March 1991

Chapter Five

Negative Ion Measurements

5.0 Introduction

In Chapter 4 both RF and DC ion sources were temporally modulated and the plasma parameters determined in the discharge and the post-discharge. A decrease in the electron temperature is observed for relatively high electron density. It has been presented that these plasma conditions are favourable for the enhanced production of negative ions. This chapter serves to investigate negative ion densities in the discharges.

Several methods have been used to allow negative ion measurements to be carried out in a discharge, e.g. Langmuir probes [1, 2] and mass spectrometry [3]. However, one of the most successful methods to date is that of photodetachment of the negative ions by a pulsed laser [4, 5]. This technique is used to temporally resolve the H^- density in the filament driven discharge when operated in continuous mode or temporally modulated mode and to compare with measurements carried out on a temporally resolved RF discharge. The results of such temporal measurements in both pulse modulated discharges are presented in this chapter.

A theoretical model of the expected negative ion density in the post-discharge is presented and compared to the experimental results.

5.1 Negative Ion Measurements on the DC Source

The negative ion densities were determined by the use of the laser photodetachment technique described preciously in Chapter Three, section 3.2. The set-up is shown here in Fig. 5.1. It was determined in the previous section that the electron density increased as a function of power and pressure. All the discharges measured in this section were generated below 10 mTorr, with a discharge voltage constant at 70 V. Fig. 5.2 below shows the increase in electron density occurring as a function of increased discharge current from 0.2 A up to 3 A.

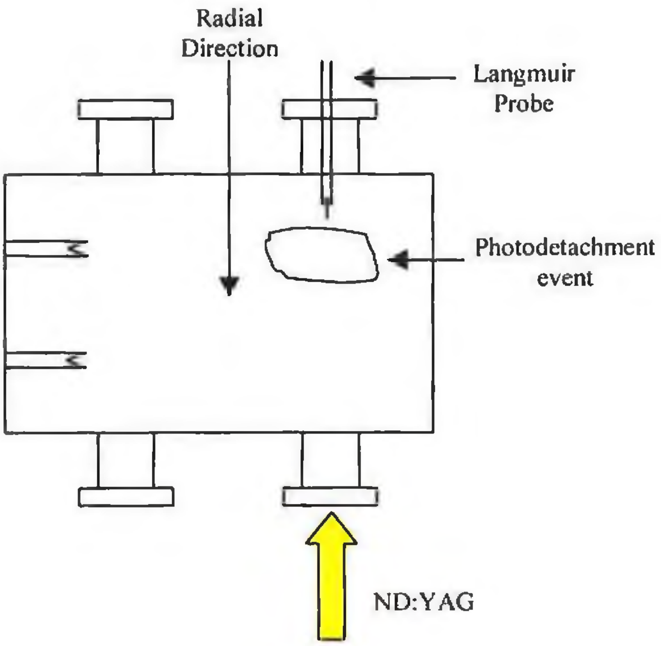

Fig. 5.1 Schematic of Photodetachment SetUp for the DC Ion Source.

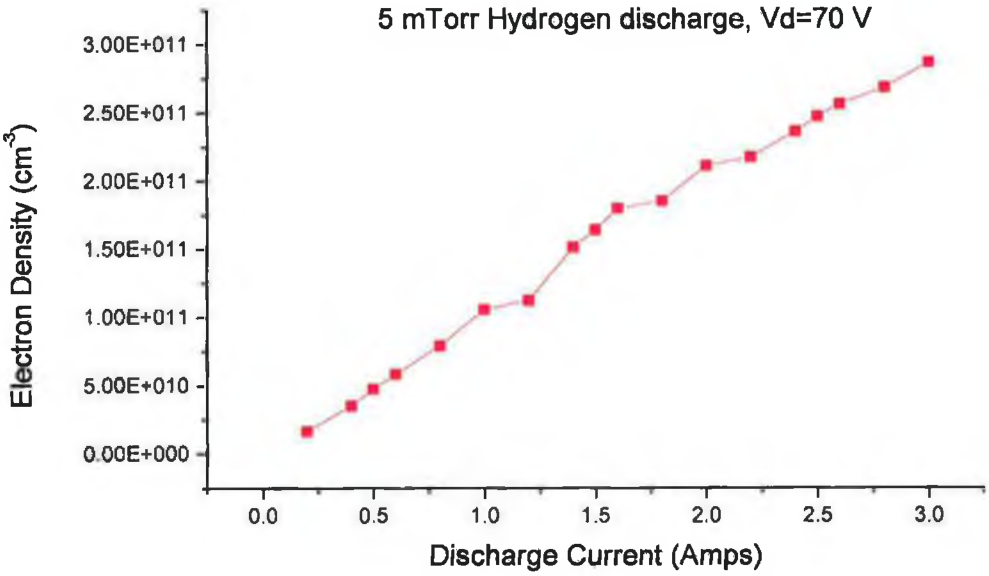

Fig. 5.2 Electron Density Variation with Discharge Current for a Hydrogen Discharge.

In the following graph, Fig. 5.3, the increase in electron density is seen as a function of the neutral gas density. The pressure ranges from 1 mTorr to 10 mTorr. The increase in electron density ranges from 1.2 x 10^{10} cm^{3} to 8 x 10^{10} cm^{-3}. As before thedischarge voltage is kept constant at 70 V.

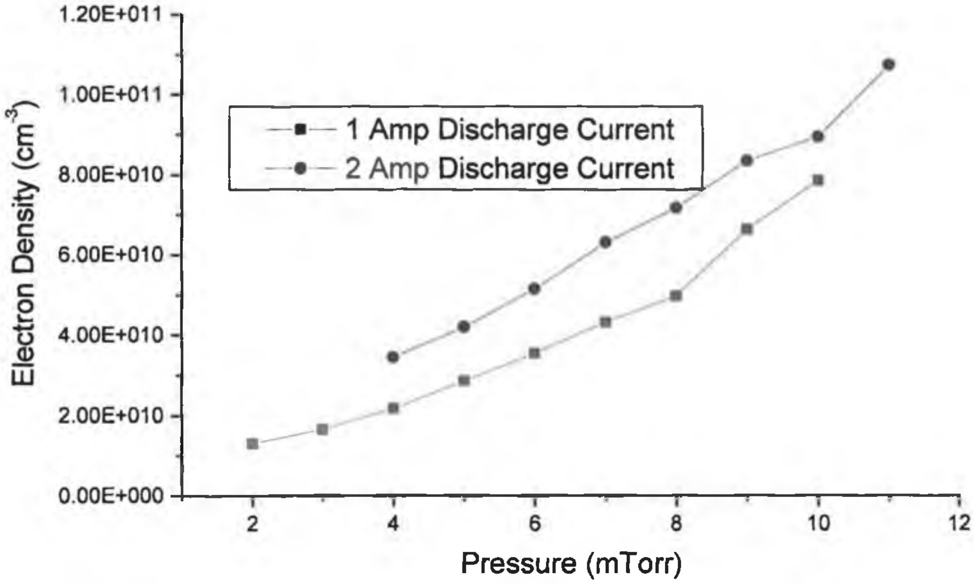

Fig. 5.3 **Electron Density Variation with Pressure for 1 and 2 A Hydrogen Discharges.**

By measuring the DC electron current, I_{dc}, in the plasma, and the AC current, I_{ac}, generated by the photodetachment technique the following graph is attained for a 1 A discharge. This can be seen in Fig. 5.4. Previous publications have shown that the dependence of the photodetachment signal in the source is highly dependent on the pressure. [6, 7] As can be seen from this graph, the DC electron current rises with increasing pressure. This is as expected as it corresponds to the increase in the electron density seen previously in Fig. 5.2. However the AC current is seen to rise rapidly from 0.1 mA to reach a plateau at 0.35 mA before decreasing as the pressure is further increased above 8 mTorr. This pressure plateau represents the optimum conditions for negative ion production taking into consideration the two stage process assumed as the major production mechanism [8], i.e. excitation of the vibrational levels, E-V process and the subsequent dissociative attachment by thermal electrons to produce the negative hydrogen ions (see Chapter One).

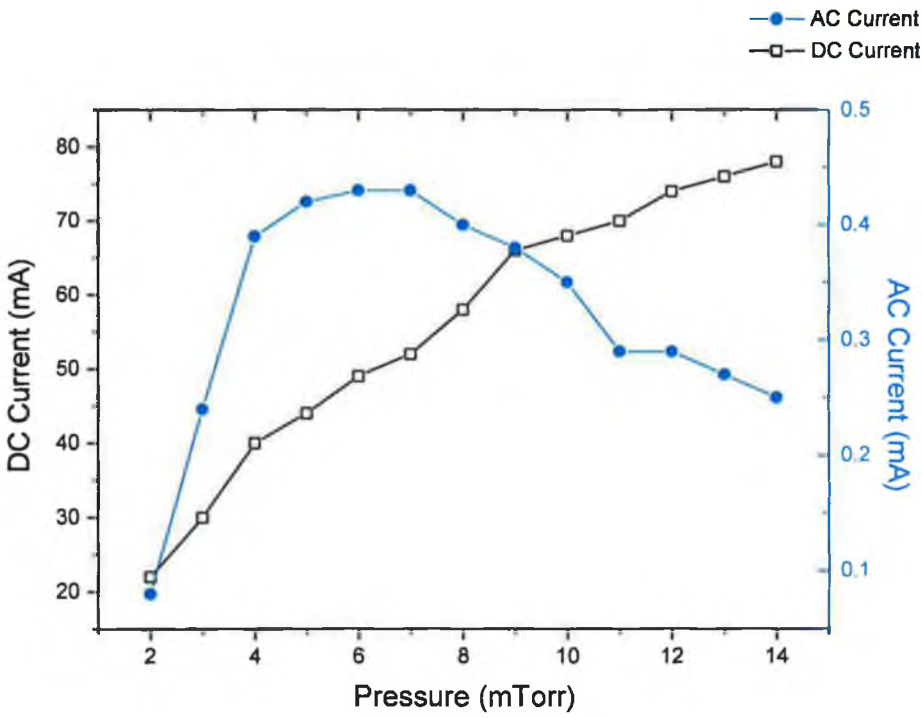

Fig. 5.4 **DC and AC Currents from 1 A Hydrogen Discharges with Varying Pressure (discharge voltage 70 V).**

As explained previously in Chapter three, the AC current, I_{ac}, collected from the photodetachment event is directly proportional to the negative ion density, and the DC current, I_{dc}, collected is directly proportional to the electron density. Therefore the ratio of I_{ac}/I_{dc} yields the ratio of n/n_e. The variation of the negative ion density to the electron density ratio is calculated and graphed in Fig. 5.5

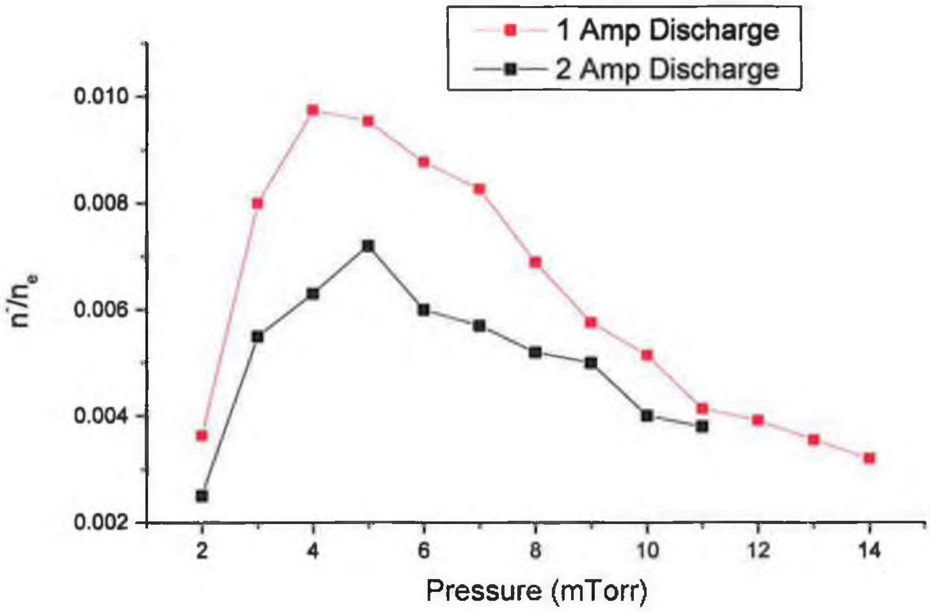

Fig. 5.5 **Variation of n_-/n_e with Pressure for 1 A Hydrogen Discharges (discharge voltage 70 V).**

The ratio of densities is seen to increase rapidly until the pressure reaches 4 mTorr, after this, the decrease is steady with increasing pressure. Having now determined the ratio it is possible to determine the actual value for the negative ion density. Knowing the electron density in the discharge plotted in Fig. 5.2 above, the absolute value for the negative ions is obtained. The density of negative ions is then plotted as a function of the increasing pressure and this is shown in Fig. 5.6 below.

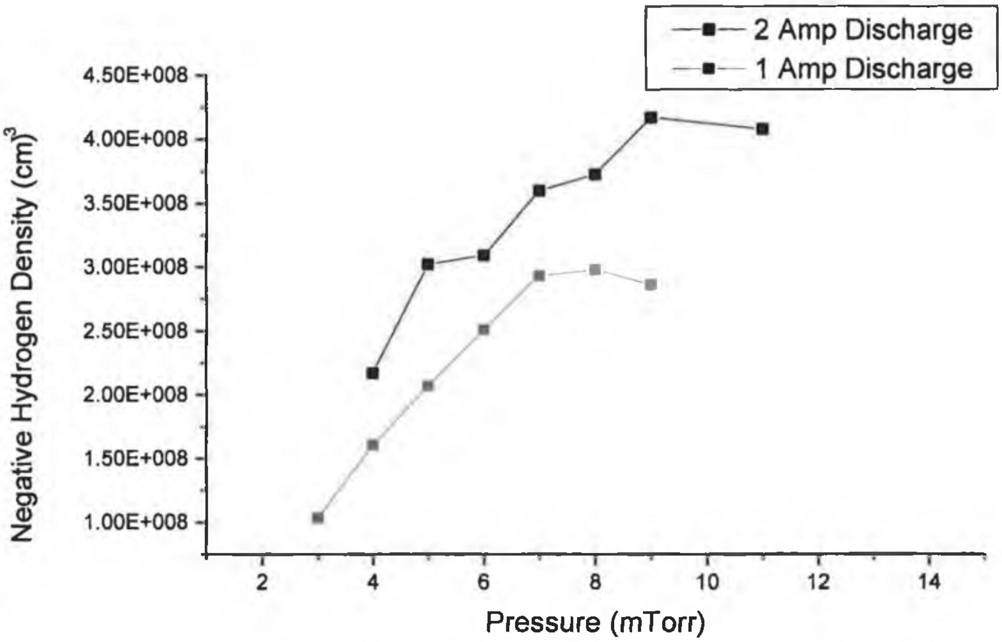

Fig. 5.6 **Negative Ion Densities Measured in a 1 A and 2 A Hydrogen Discharge at Various Pressures (discharge voltage 70 V).**

5.1.1 Negative Ion Measurements as a Function of Discharge Current

As seen previously the electron density increases with increasing discharge current. This can be seen in the following graph. In the hydrogen discharge shown above in Fig. 5.2 the characteristic increase is plotted as a function of current. The dependence of the ratio of the negative ion density to the electron density is then plotted as before by monitoring the DC current in the discharge and the AC current due to the photodetachment event. The ratio is shown in Fig. 5.5.

Knowing the ratio as before the negative ion density absolute value could be determined. The dependence of the negative ion density on the discharge current and pressure was shown for a 1 A discharge and a 2 A discharge. The plot shows the optimum conditions at 10 mTorr for a 2 A discharge, but for a 1 A discharge the optimum occurs at 7 mTorr. This change in the pressure plateau can be explained by the difference in the electron temperatures of the 1 A and 2 A discharges. The temperature in the 2 A discharge will be higher than that of the 1 A discharge and therefore a higher pressure is required for optimisation of the production of the negative ions. It is because of this high pressure maximum plateau that can limit the use of volume ion sources for neutral beam heating, as negative accelerators will require lower pressure operating conditions. [9]

5.2 Time Resolved Photodetachment Measurements on the DC Source.

It has been shown [9, 10, 11] that an increase in negative ion density can be obtained by time modulation of low pressure, high power volume ion sources in the post-discharge. These experiments were repeated here and verified. As explained previously in Chapter One, the main production mechanism for negative hydrogen ions is that of dissociative attachment of highly vibrationally excited hydrogen molecules. The main destruction mechanism is that of electron detachment by hot electrons. As stated previously, the main solution to this problem, to avoid the destruction of the ions is to divide the chamber into two different regions, the driver regions and the extraction region. This method results in the suppression of the fast electrons, and the reduction of the destruction mechanism. The solution being explored here relies on the same principle. That is the enhancement of the production process by means of suppressing the fast electrons, however instead of the spatial separation as a solution, this technique utilises a temporal solution.

By temporally modulating the discharge, i.e. switching the discharge on and off, it has been proposed that the high lying vibrational state population of H_2, with vibrational levels >5, will survive a number of wall collisions [12].

In the post-discharge the fast electrons disappear and the electron temperature falls dramatically. By reducing or suppressing the fast electrons, the main destruction mechanism is reduced, and therefore the negative ion density increases the lifetime of the vibrationally excited hydrogen molecules which is longer than that of the fast electrons. Hence the negative ions are continued to be produced until the slow electrons disappear.

The results of these measurements are shown here. Fig. 5.7 shows a plot of the photodetachment signal variation with time in the discharge and the post-discharge régimes. The pressure is 1 mTorr and the discharge is 1 A. The pulse duration is *2ms* and the repetition rate 10 Hz. The probe was situated in the centre of the discharge. The steady state signal is 2.2 x10 $^{-4}$ A. When the discharge is switched off, at 0 μs, the photodetachment signal increases to 3 x 10-4 A in approximately 17 μs rise time.

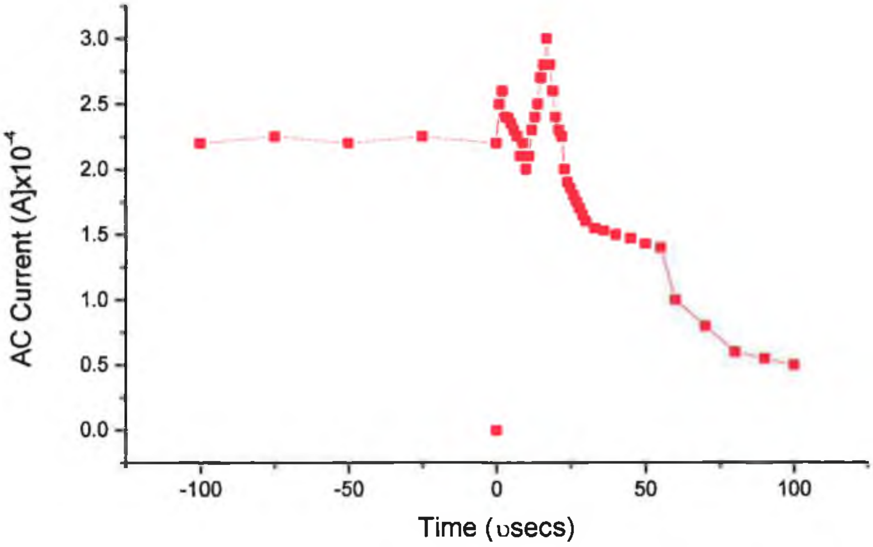

Fig. 5.7 **Time Resolved Photodetachment Signal in the Discharge and Post Discharge Régimes (pressure 1 mTorr, discharge current 1 A).**

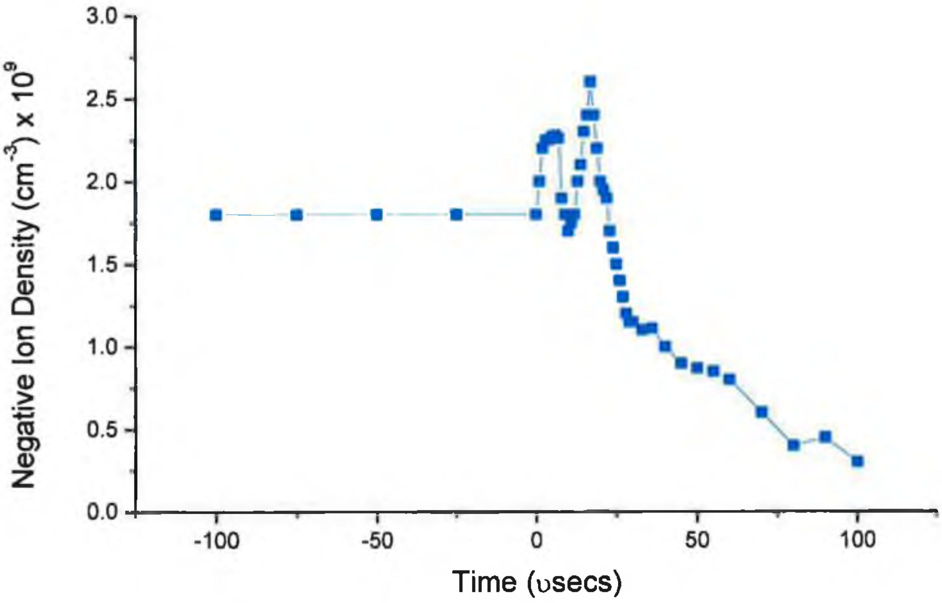

Fig. 5.8 **Time Resolved Negative Ion Density in the Discharge and Post Discharge Régimes (pressure 1 mTorr, discharge current = 1 A).**

The negative ion densities calculated and plotted above in Fig 5.8 are given by:

$$n^- = n_e \times \frac{I_{ac}}{I_{dc}} \qquad \textit{Equation 5.1}$$

The electron current collected by the probe is given by:

$$I = \frac{n_e e u_e A}{4} \qquad \textit{Equation 5.2}$$

Where the average electron velocity is given by:

$$u_e = \left[\frac{8kT_e}{\pi m_e}\right]^{\frac{1}{2}} \qquad \textit{Equation 5.3}$$

therefore,

$$n^- = \frac{1}{(kT_e)^{1/2}} \qquad \textit{Equation 5.4}$$

This shows that while the electron flux in the post-discharge increases, the electron temperature decreases in the post-discharge. This increase in flux represents a sharp increase in the negative ion density as shown in Fig. 5.8. The importance of the two graphs shown above, Fig. 5.7 and Fig 5.8 lies in the fact that an enhanced negative ion density is indeed found in the post-discharge at low pressures.

It must be noted that a double peak is observed in the afterglow of the negative ion density profile. In an effort to understand this "double-peak" a basic model of the reactions taking place, DA, CD and EV , are modelled with respect to variation of the plasma parameters in the afterglow . This is discussed in Section 5.6.

5.2.1 Pressure Dependence of the Time Resolved Photodetachment Signal

Fig. 5.9 below shows the measured time resolved negative ion densities in the discharge and the post-discharge régimes as a function of pressure in a 1 A , 70 V discharge. The probe is in the centre of the chamber for these results. It can be seen that at lower pressures the post-discharge peak in the negative ion density is larger than in the steady state. At 1 mTorr the negative ion density increased from the steady-state value of 1.8 x10^4 cm^{-3} to 2.6 x10^{-4} cm^{-3} in the post-discharge, whereas at 10 mTorr the steady-state value for the density of the negative ions was 3.6 x 10^4 cm^{-3} and the increase in the post-discharge only brought the density to 3.8 x 10^4 cm^{-3}. Increasing the pressure reduces the magnitude of the increase seen in the post-discharge.

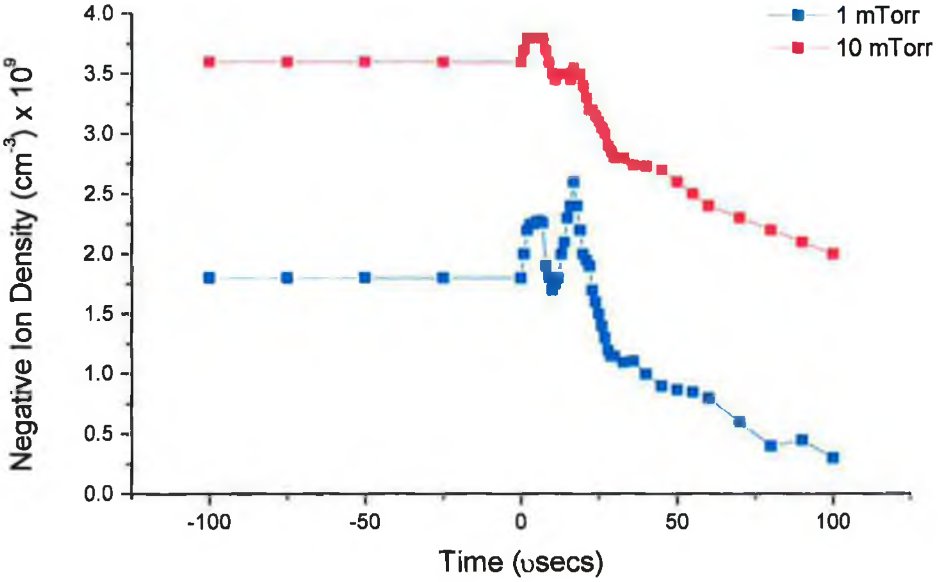

Fig. 5.9 **Time Resolved Negative Ion Densities for Different Source Pressures (discharge current 1 A).**

5.2.2 Current Dependence of the Time Resolved Photodetachment Signal

Shown below are the peak photodetachment signals in the post-discharge, I_{ac}(peak), and the photodetachment signals in the discharge, I_{ac}(cw), for two different discharge currents, Fig 5.10(a) and Fig 5.10(b). From these graphs it is evident that the post-discharge peak to continuous peak ratio variation with pressure is dependent on the discharge current. From Fig 5.10(a) it can be seen that the ratio at the lower discharge current of 1 A, for the 4 mTorr plasma is very small and tending towards unity. In Fig 5.10(b) at 3 A the peak/DC ratio goes to zero again but at higher pressures.

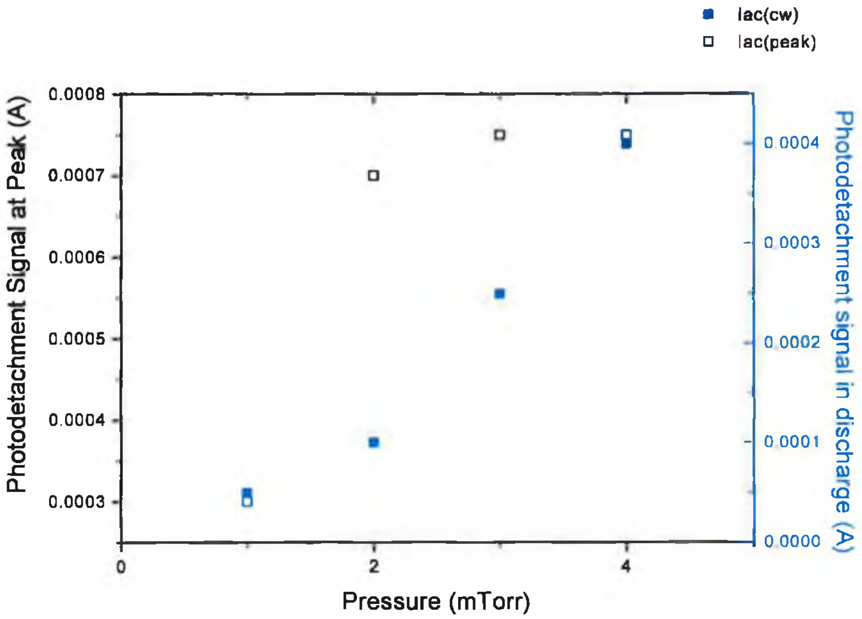

Fig. 5.10(a) Photodetachment Signals as a Function of Pressure Taken at the Peak and during the Discharge (discharge current 1 A).

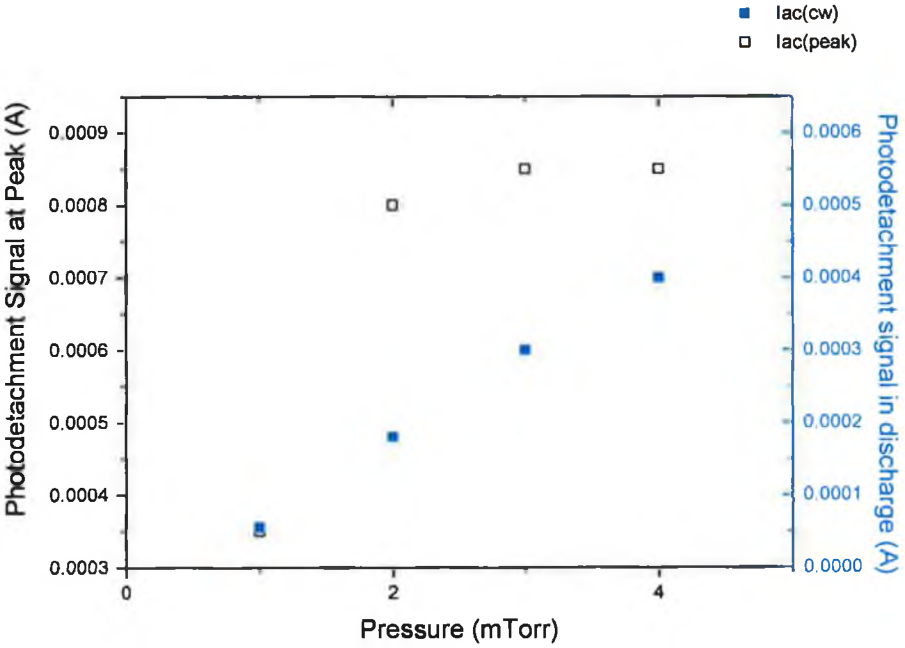

Fig. 5.10(b) Photodetachment Signals as a Function of Pressure Taken at the Peak and during the Discharge (discharge current 3 A).

5.3 Spatial Dependence of the Temporally Resolved PhotodetachmentSignal

Previous experiments have reported the dependence of the ion source parameters on where the measurements have been taken within the discharge. Knowledge of the spatial dependence of the pulsed discharge is important as further insights into the processes occurring with temporal modulation can be gained. The radial dependence of the negative ion density is discussed here for the DC ion source on DENISE.

5.3.1 Radial Dependence of the Photodetachment Signals

The probe was aligned with the Nd:YAG laser as shown in Fig. 5.1. This configuration allowed for the probe to be moved across the radius of the chamber, 15cm from the front plate. Photodetachment measurements were taken in a 1 mTorr discharge, with a discharge current of 1 A and discharge voltage of 70 V. The centre of the discharge is referred to as being at 0 cm. The following graph, Fig. 5.12 shows the variation in the photodetachment signal on moving the probe from the centre outwards towards the wall.

In the centre of the discharge at 0 cm, the signal current in the discharge is measured to be 1 x 10^{-4} A. Moving the probe towards the wall shows an increase in the measured photodetachment signal until about 6 cm from the wall where it is measured to be 3x10^{4} A. Moving closer to the wall the signal starts to fall off. The peak value for the photodetachment shows a similar trend, increasing from 7 x 10^{4} A at the centre to 8.7 x 10^{-4} A at 4 cm from the wall and then falling off dramatically. The ratio of the peak to continuous photodetachment signal in the centre of the chamber is found to be 7. But while moving towards the wall the ratio falls off until it reaches unity at 8 cm from the centre (or 2 cm from the wall). This can be explained by considering the permanent magnetic field arranged on the chamber walls. This field prevents the hot, primary electrons from reaching the walls and confines them into the centre of the plasma. This spatial dependence was shown previously in Chapter 4, Fig. 4.5.

The electron temperature in the centre of the plasma is hot, and this temperature decreases as the wall is approached in the magnetic filed region. This suggests that the centre of the plasma is where the molecules become excited, while in the magnetic field region only the vibrationally excited levels exist, where it is cooler allowing for a higher production level of negative ions at the wall. The ratio of the peak to continuous photodetachment signal indicates that this is actually what is happening.

The reaction rate of the dissassociative attachment process increases as the electron temperature decreases resulting in the increased production of the negative ions on moving towards the wall. Therefore the losses due to the fast electrons are decreased, the collisional detachment reaction rate is diminished. The reduction in the ratio of the peak to continuous photodetachment signal indicated a reduction in the loss process and a cooler electron temperature at the wall results in a less dramatic increase in the negative ion density in the post-discharge. The fall in the negative ion density at the walls is due to a low electron density in the cusps.

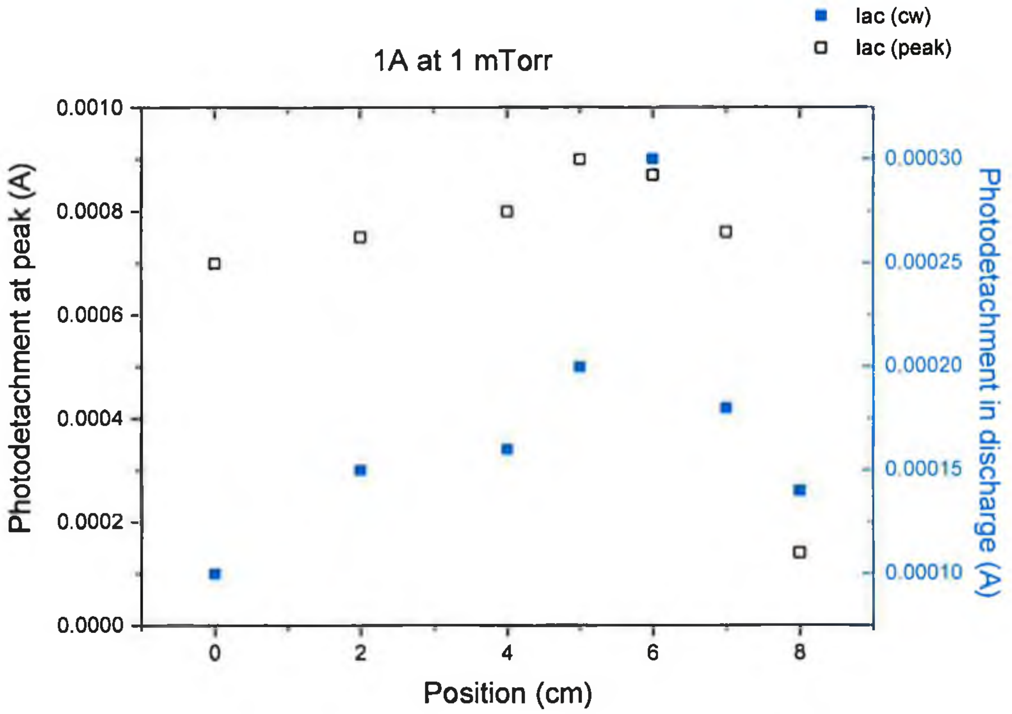

Fig. 5.11 **Photodetachment Signals from Peak and Continuous Discharge as a Function of the Radial Position in the Chamber (discharge current 1 A, pressure 1 mTorr).**

5.4 Negative Ion Measurements on the RF Source

The laser photodetachment technique was set up as described previously for the RF ion source on DENISE. The schematic of the set-up is shown in Fig. 5.13. The alignment of the laser is set up as previously described. The front plate of the ion source is changed so that it now provides a port to install the quartz tube, which houses the copper antenna. The power supply units are changed over to use the RF generator described in Chapter Two.

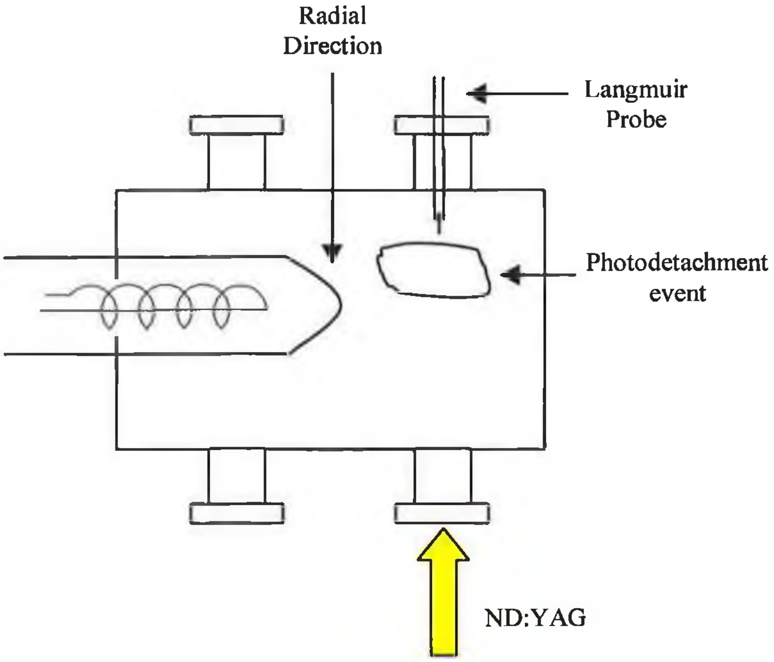

Fig. 5.12 **Schematic of Photodetachment Set-Up on the RF Ion Source.**

As previously, a plot of the electron density as a function of power is obtained. A typical plot is shown below in Fig. 5.14. This graph shows the variation in the electron density with increasing power as measured by the output of the RF power supply and forward power measured by the Bird meter. When the power is below ~1250 W, the discharge is still in the E- mode or capacitive mode and the electron densities in this region are quite low, typically 10^7 cm^{-3} / 10^8 cm^{-3}. On increase of the input power the discharge moves from capacitive to inductive H-mode and the electron density increases dramatically to 10^{10} cm^{-3} - 10^{11} cm^{-3}. The input power is varied between 200 and 2800 W. In the following graph Fig. 5.14 the increase in the electron density is shown as a function of the neutral gas density. The pressure ranges from 10 mTorr to 50 mTorr. The increase in the electron density ranges from 10^{10} cm^{-3} to 10^{11} cm^{-3}.

The laser photodetachment technique cannot be carried out on these plasmas as the generation frequency is 13.56 MHz, therefore the time is 1/f = 73 nsecs. The photodetachment even takes place in at nearly the same period. For this reason another solution to determining the negative ion densities in RF driven discharges was required. The solution chosen was to use the temporally resolved photodetachment technique and therefore determine the negative ion density in the afterglow of the discharge. This solution was chosen because of the effectiveness of temporal modulation seen on the DC source described in the previous section.

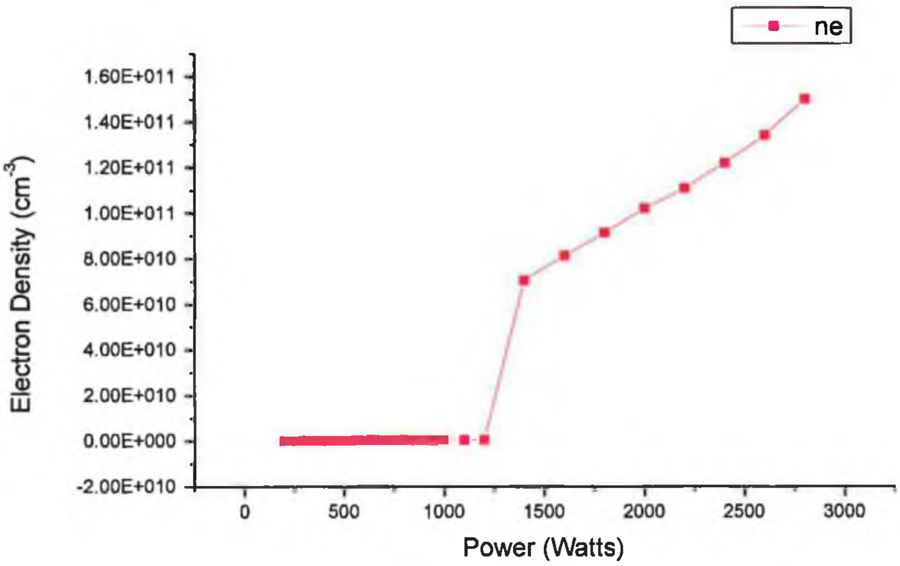

Fig. 5.13. **Electron Density Variation with Input Power for a Hydrogen Discharge at 10 mTorr.**

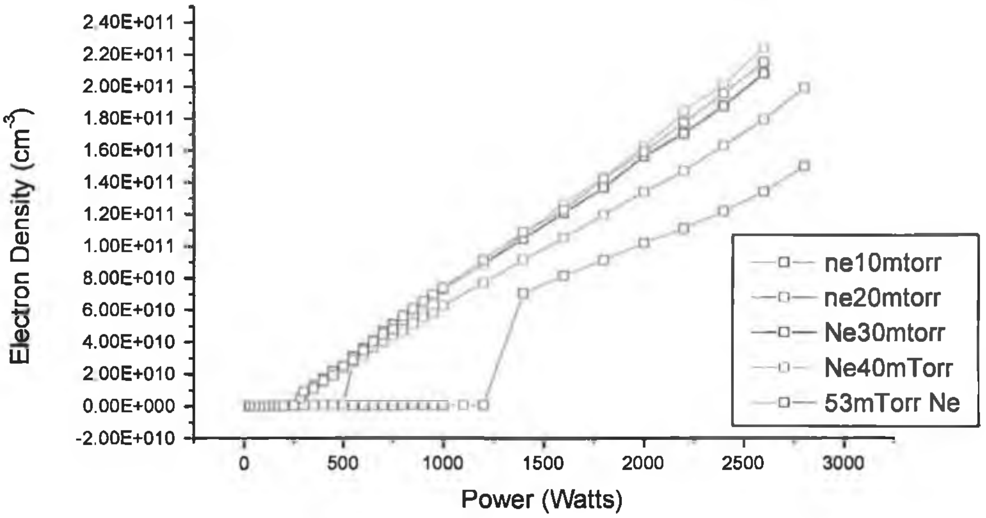

Fig. 5.14 **Electron Density Variation as a Function of Power for Varyious Pressures.**

5.5 Temporally Modulated Photodetachment Measurements on the RF Ion Source

In an effort to measure the negative hydrogen densities in the RF source, the RF input power was temporally modulated as described previously in Chapter 4. In the post-discharge the electron temperature falls dramatically. In the following graph, Fig. 5.16, the dramatic drop in electron temperature can be seen from approx. 4.5 eV to approx. 0.5eV in a 1500 W discharge at 20 mTorr, with a pulse train of 200 μs and 50 % duty cycle.

The decrease in electron temperature happens instantaneously with the "switch-off" of the plasma. The electron density is also shown in this graph and as explained previously the density falls off due to ambipolar diffusion in the source. By reducing the electron temperature in the source in the post-discharge, the main destruction mechanism is also reduced, and the negative ions are continued to be produced until the slow electrons disappear, when the discharge is switched back on. The results of these measurements are shown here.

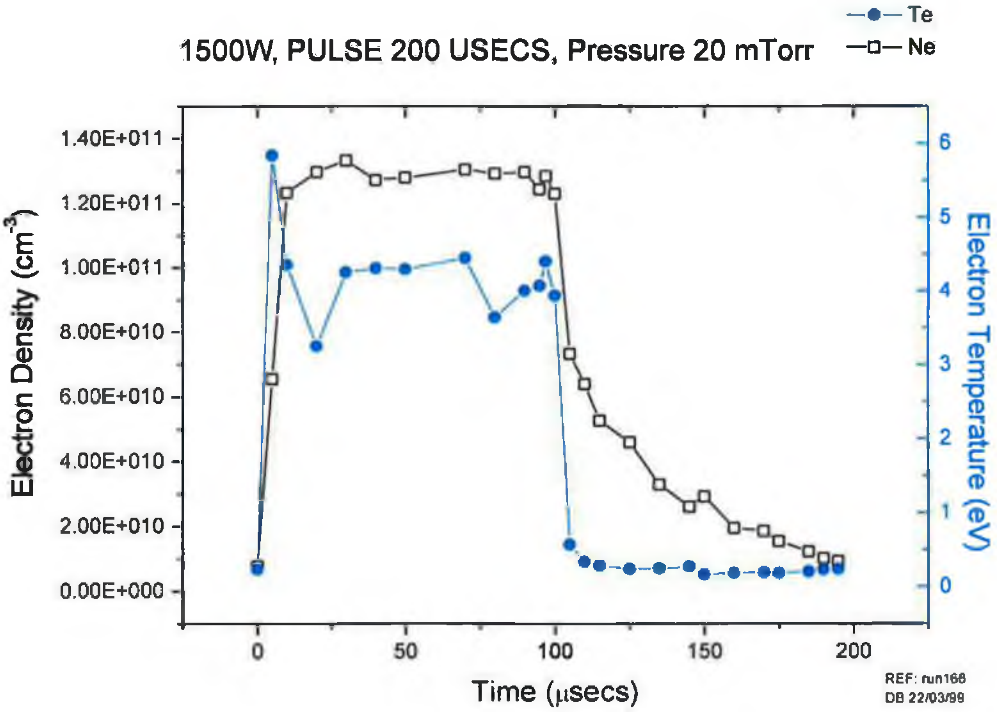

Fig. 5.15 **Variation of Electron Density and Temperature in a 1500 W RF Hydrogen Discharge at 20 mTorr Pulsed at 200 μs with a 50 % Duty Cycle.**

In order to get an idea of the efficiency of negative ion production in both the RF and the DC source

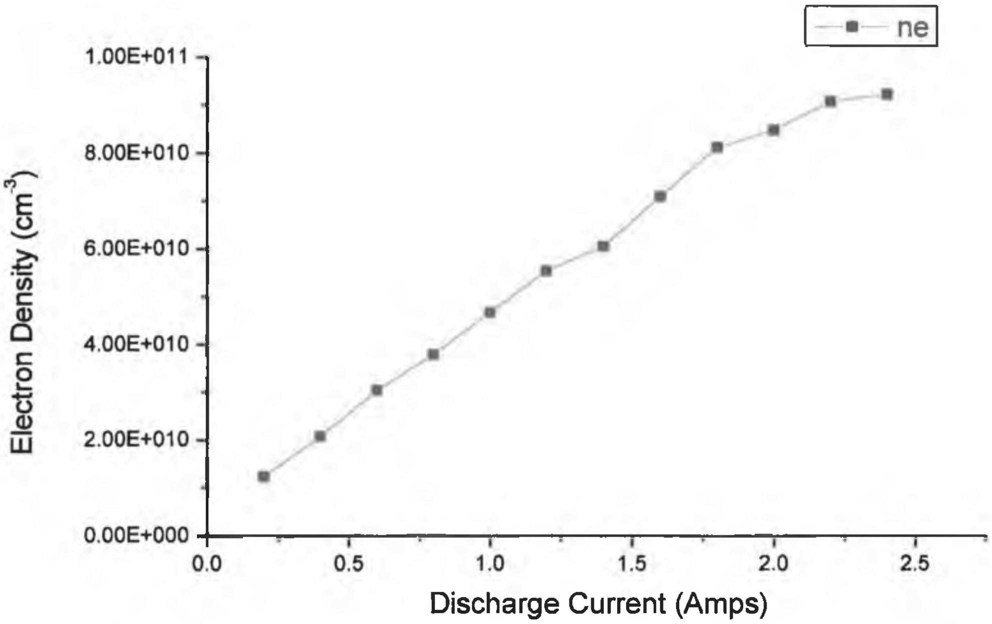

Fig. 5.16 **Electron Density as a Function of Current in a DC Discharge at 10 mTorr.**

discharges of similar electron densities at the same pressures are compared. Looking at the two previous graphs in Figs. 5.13 and Fig.5.16it can be seen that the density of electrons in the RF discharge at 1500 W is comparable to the density of electrons in the DC discharge at 1.5 A discharge current when both plasmas have a source pressure of 10 mTorr.

A plot of the negative ion density found in a 10 mTorr H_2 discharge generated in the RF source is shown below, Fig. 5.18. The input power is measured to be 1500 W, the pulse train is 200 μs and the duty cycle is 50 %. The electron density is shown here as a function of time in the afterglow of the discharge, where 0 μs is the switch-off time of the input power.

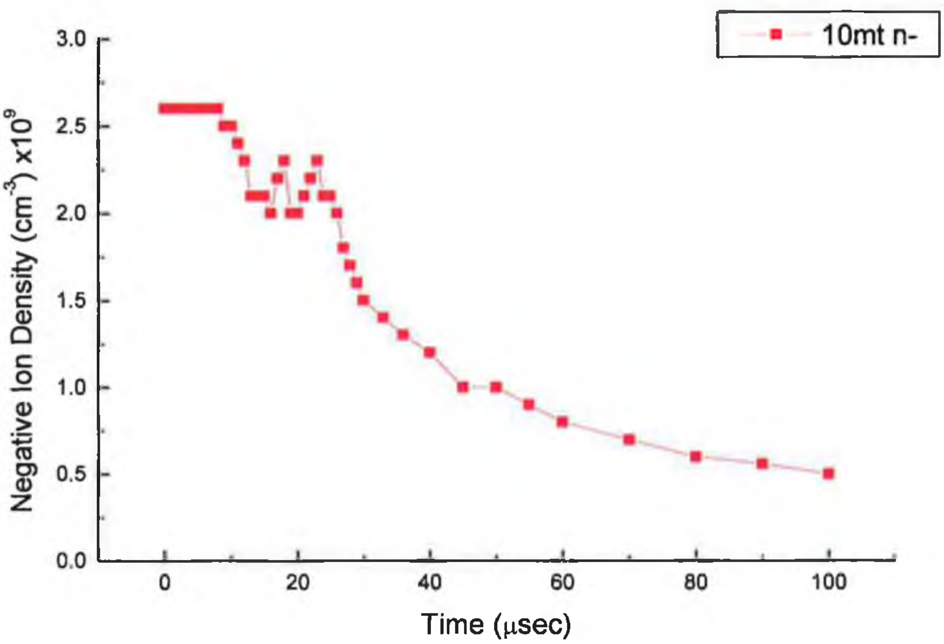

Fig. 5.17 **Negative Ion Density Measured as a Function of Time in the Afterglow of a 1500 W H_2 discharge (200 μs pulse train with 50% dutycycle).**

The double peak in the negative ion density yield seen in the post-discharge of the DC plasma is also observable in the afterglow of the RF discharge. The profiles of both density functions with time are similar. The decay rates are very alike.

The density of negative ions in the afterglow of the RF discharge is found to be slightly less than that found in the afterglow of the DC discharge with comparable electron density. A graph showing the collected negative ion densities as a function of time in each afterglow is shown below in Fig. 5.19.

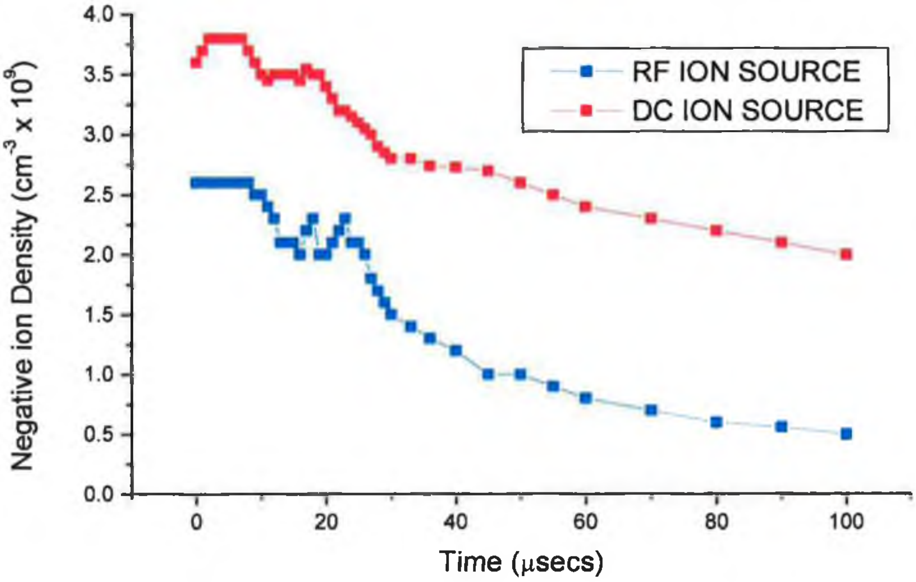

Fig. 5.18 **Comparison of Negative Ion Densities in the Afterglow between an RF and a DC Discharge of Comparable Plasma Density (10 mTorr source pressure, 200 μs pulse train, 50% duty cycle).**

It is surprising that the negative ion yield from the RF discharge is less than that of the DC discharge. Although the powers and pressures investigated here are not relative to the powers and pressures required for the ITER NBI systems, investigations on the small sources used here can lead to further experimentation on the more relevant sources.

In another series of experiments the duty cycle was altered to increase the "on-time" of the dishcarge and decrease the "off-time". The cycle was set at 75 % , allowing a discharge duration of 150 μs and an afterglow of 50 μs. A plot of the measured negative ion density is shown below in Fig. 5.20. The conditions are the same as for the previousfigures, the pressure is set at 10 mTorr and the RF forward power is 1500 W. The density of negative ions is shown as a function of time in the afterglow, where 0 μs is the beginning of the afterglow, when the forward power is turned off. A slight increase in ion density is measured in the 200 μs pulse train modulated at 75% duty cycle. An initial increase of 0.4 is observable in the begining of the afterglow, but after 30 μs into the post-discharge the negative ion density falls below the measured ion density for the 50 % duty cycle and the density falls rapidly then to near zero.

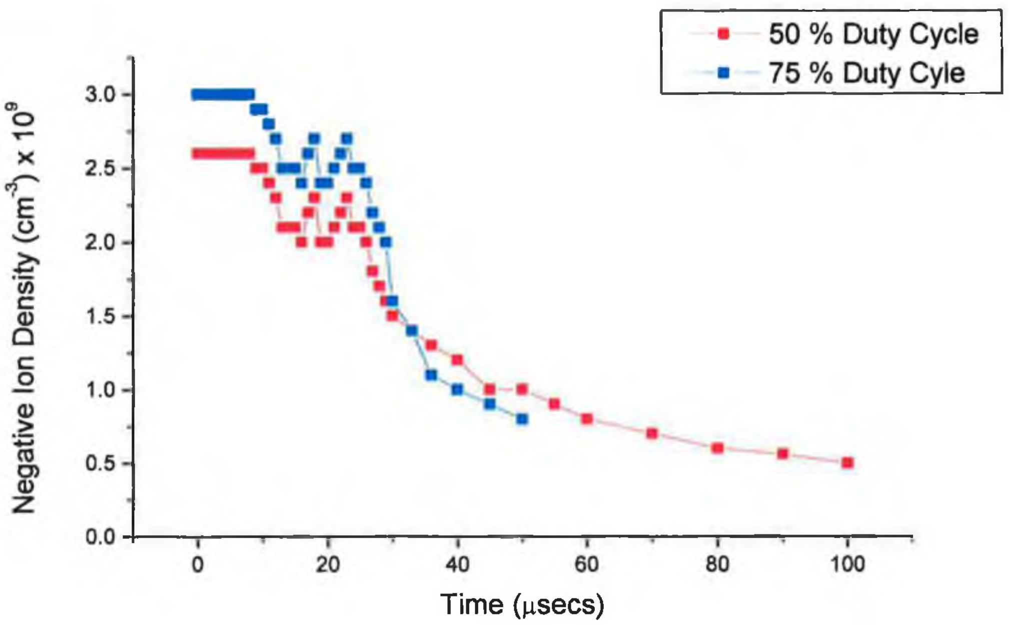

Fig. 5.19 **Negative Ion Density as a Function of Time in the Afterglow of a 1500 W H_2 Discharge (200 μs pulse train, varied duty cycle).**

As seen in the filament driven discharge, it is believed that the reaction rate of the dissociative attachment process increases as the electron temperature decreases when the forward RF power is turned off. The electron temperature for the 75 % Duty cycle in the afterglow is found to be approximately 0.7 eV and is measured at 0.5 eV for the 50 % duty cycle. The reaction rate for the dissociative attachment process, calculated by Wadehra and Bardsley [13] at an electron temperature of 0.5 eV is approximately 2.5 cm^3s^{-1}, and the reaction rate at 0.7 eV is approximately 3.25 cm^3s^{-1}. This increased reaction rate for the process of dissassociative attachment results in the slight increase seen in the negative ions produced at the two different duty cycles.

5.6 Modeling the Negative Ion Density in the Afterglow of the RFDischarge.

In an effort to model the negative ion densities in the post discharge of an RF plasma, a number of assumptions were made. It was assumed that the dominant mechanism for the production of negative ions was dissociative attachment, allowing the negative ion density in a steady state discharge to be determined by:

$$n_- = n'' n_e < \sigma_{DA} u_e > \qquad \textit{Equation 5.5}$$

where n_- is the negative ion density , n_e the plasma density, n" is the density of vibrationallly excited molecules and $< \sigma_{DA} u_e >$ is the reaction rate for dissociative attachment of electrons to $H_2(v'')$.

The decay of n_- in the steady state discharge can be determined by the following equation:

$$t_- = V / L + n_e < \sigma_{CD} u_e > + n_i < \sigma_{MN} u_i > \qquad \textit{Equation 5.6}$$

from left to right these terms represent the loss terms due to wall collisions, collisions with fast electrons in the electron detachment reaction, collisions with positive ions respectively.

As seen in *Equation 5.5.* the negative ion density is dependent on the density of vibrationally excited molecules, assuming that the predominant process for negative ion production is DA. Therefore the dependence of the vibrational states on the temporal behaviour of the discharge must also be determined when the plasma is pulsed. The assumption here is that the predominant process of the vibrational excitation of molecules is by fast electron ionisation through the singlet states. This assumption is valid for high density discharges. In the steady state the density is determined by

$$n'' = n_g n_e < \sigma_{EV} u_e > \qquad \textit{Equation 5.7}$$

where n_g is the gas density and $< \sigma_{EV} u_e >$ is the reaction rate coefficient for vibrational excitation through the EV process.

The loss of $H_2(v'')$ is determined by the following equation:

$$t'' = V'' / B'' L'' + n_e < \sigma_{MN} u_e > + n_e < \sigma_{DA} u_e > \qquad \textit{Equation 5.8}$$

where from left to right the terms represent losses to the wall, mutual neutralisation (MN) and losses by DA.

In the post-discharge the vibrational denstiy will decay with a loss time of 1 ms [14].

5.6.1 *Calculation of the Rate Coefficients.*

The velocity distribution of the particles in the discharge can be expressed by:

$$f(u) = 4\pi n u^2 \left[\frac{m}{2\pi kT}\right]^{3/2} e^{-\frac{mu^2}{2kT}} \qquad \text{Equation 5.9}$$

In the post-discharge the distributions are Maxwellian so this can be used to determine the reaction rate coefficients *<P(u)>*.

$$< P(u) >= \frac{1}{n}\int_0^\infty P(u) f(u) du \qquad \text{Equation 5.10}$$

Thus for a maxwellian distribution the collisional rate is given by,

$$< \sigma(u) >= \frac{1}{n}\int_0^\infty \sigma(u) u f(u) du \qquad \text{Equation 5.11}$$

Thus,

$$< \sigma(u) >= 4\pi\left(\frac{m}{2\pi kT}\right)^{3/2} \int_0^\infty u^3 \sigma(u) e^{-\frac{mu^2}{2kT}} du \qquad \text{Equation 5.12}$$

Usually the cross sections are expressed in terms of the energy rather than the velocity so the energy distribution has to be determined by,

$$f(\varepsilon) = \frac{2\sqrt{\varepsilon}}{\sqrt{\pi}(kT)^{3/2}} e^{-\frac{\varepsilon}{kT}} \qquad \text{Equation 5.13}$$

where the energy distribution function is normalised such that,

$$\int_0^\infty f(\varepsilon)d\varepsilon = 1 \qquad \textit{Equation 5.14}$$

and from this the reaction rate coefficient can be defined by:

$$<\sigma(u)>= 8\frac{\pi}{\sqrt{m}}\left(\frac{1}{2\pi kT}\right)^{\frac{3}{2}}\int_0^\infty \varepsilon\sigma(\varepsilon)e^{-\frac{\varepsilon}{kT}}d\varepsilon \qquad \textit{Equation 5.15}$$

Using the energy distribution function and the appropriate cross section the reaction rate coefficient for any process of interest can be determined.

Using the above Equations the H$^-$ density can be modeled in the afterglow of the pulsed RF discharge. The following process was used:

$$\frac{dn_-}{dt} = production - loss \qquad \textit{Equation 5.16}$$

where, the production rate is given by Equation 5.5 above and the loss rate is given by Equation 5.6.

In the steady state discharge, $\frac{dn_-}{dt} = 0$, therefore the density can be calculated from the following equation:

$$n_- = \frac{production}{loss} \qquad \textit{Equation 5.17}$$

which yields the following equation:

$$n_- = \frac{n_e n'' <\sigma_{DA}u>}{(b''u''/l'') + n_e <\sigma_{DA}u_e> + n_e <\sigma_{MN}u_e>} \qquad \textit{Equation 5.18}$$

In the temporally modulated discharge the negative ion density changes with time, $\frac{dn_-}{dt}$ is not equal to zero. This means that the density equation produces the following equation:

$$dn_- = n_e n'' < \sigma_{DA} u > *dt - (u''/b''l'') + ne < \sigma_{CD} u_e > + n_e < \sigma_{MN} u_e > *dt$$

Equation 5.19

Using plasma parameters determined by the Langmuir probe in a temporally modulated discharge at 20 mTorr and 1500 W, a plot of the negative ion density expected was calculated. These densities are plotted as a function of time in the afterglow of an RF discharge in Fig. 5.21.

The reaction rates for the above equations were calculated using the cross sections given inAppendix B.

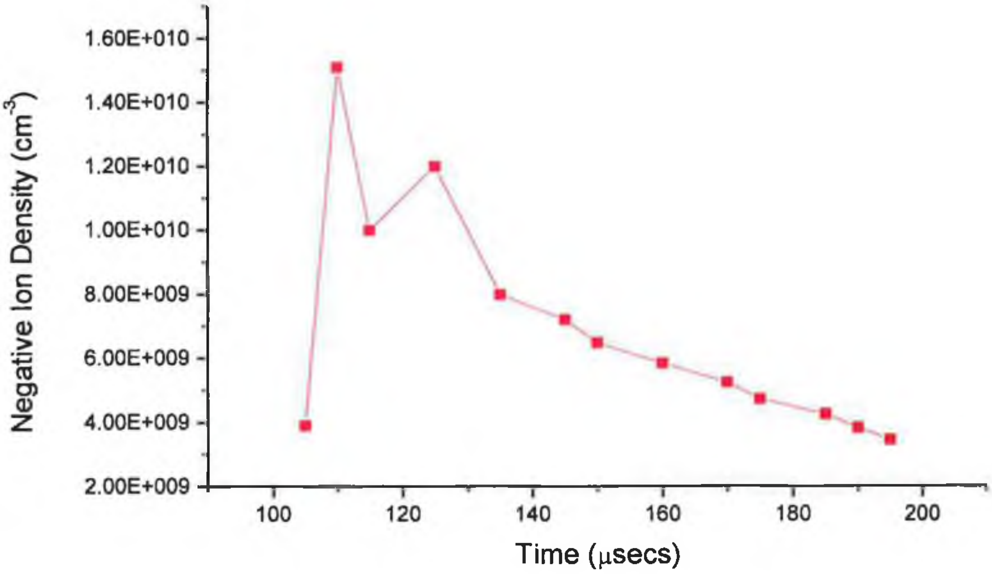

Fig. 5.20 **Modelled Negative Ion Densities in the Afterglow of a 20 mTorr H_2 RF Discharge (power 1500 W , duty cycle 50 %, pulse train 200 μ s).**

From Fig. 5.21 It can be seen that the double peak observed in the afterglow of the experimental data is also present in the model. Alterations in the plasma parameters in the afterglow lead to the alterations in the yielded negative ion density. The profile of the temporal density agrees qualitatively very well with experimental results.

5.7 Conclusions

In this chapter the photodetachment technique was used to determine the negative ion densities in the DC and RF volume ion sources on DENISE. The DC source was operated in both continuous and temporally resolved modes of operation. The results shown here verify the enhancement in negative ion densities in the post-discharge. Spatial dependence studies show a strong increase in density in the centre of the source.

The RF source was operated in pulsed mode and negative ion densities were determined as a function of the time in the afterglow. Comparison between the RF and the DC data show that the DC source produces a higher density of negative ions than the RF ion source when modulated at the same duty cycle.

Further it was seen that the density of negative ions in the source could be increased with modulation of the discharge at different duty cycles. This increase is due to the change in electron temperature which then in turn alters the reaction rate for the main production mechanism of negative ions, dissassociative attachment.

A double peak in the negative ion density is observed in the afterglow of both the RF and DC discharges in the experimental data. In an effort to determine the validity of these results, the negative ion density in the afterglow of the RF discharge was modeled . The characteristic double peak was again observed in good qualitative agreement with the measurements.

It can be concluded from this chapter that the RF ion source operates relatively efficiently as a volume production source. However, the "RF specific" lower H^-yield compared to a DC discharge in comparable plasma conditions is unexpected and deserves further investigation.

References

[1] Katsch, H.M. and Quandt, E.
4th European Workshop on the Production and Application of Light Negative Ions, Belfast, 1991.

[2] Ameniya, H.
Journal of Pysics D: Applied Physics, 23, p999, 1990

[3] Nicolopoupou, E, Bacal, M.,and Doucet, H.J.
Journal de Physique, 38, p1399, 1997.

[4] Bacal, M. and Hamilton, G.W.
Physical Review Letters, 42, p1538, 1979.

[5] Devynck, P. *et al*
Rev. Sci. Instrum., 60 (9), p2873, 1989.

[6] Holmes, A.J.T *et al*
Rev. Sci. Instrum., 58 (2), p223, 1987.

[7] Ehlers, K.W. *et al*
4th Internalional Symposium on the Production and Neutralization of Negative Ions, Brookhaven 1986.

[8] Bardsley, J.N.
2nd International Symposium on the Production and Neutralization of Negative Ions and Beams, Brookhaven, 1980.

[9] Heeran, R.M.A. et al
Europhysics Letters, 17 (6), p503 – 508, 1992

[10] Katsch, H.M. and Quandt, E.
J. of Physics D: Applied Physics, 25, p430, 1992.

[11] Mellon, K.N.
PhD Thesis, Dublin City University, 1993.

[12] Hisks, J., Karo, A., Bacal, M., Brunteau, A., Graham, W.
J. Appl. Phys. 53, p3469, 1982

[13] Wadehra , J., and Bardsley, J.
Phys. Rev. Lett. 41 p1795, 1978

[14] Lefebvre, M. et al.
“Proc. Production and Application of Light Negative Ions.” Paris 1986

Chapter Six

Argon Seeding of Volume Negative Ion Sources

6.0 Introduction

It has been found that the addition of argon in a negative ion source can have the effect of much improving the negative hydrogen ion density. The extracted negative ion current for multicusp volume ion sources was shown to increase with the addition of argon or xenon at low pressures [1, 2]. These increased extracted currents were, however, found in the extraction region where the extraction system had been optimised for the particular gas system. In an effort to enhance negative ion production in continuous wave DC and RF volume ion sources, small amounts of argon gas were added to the hydrogen discharge and the effect of the admixture on the plasma parameters was investigated. The observations were interpreted in terms of changes of electron temperature and density caused by the addition. A number of different systems were used to carry out this investigation, two different RF sources and two filament driven sources.

The RF sources investigated were the DENISE RF source described previously and a volume ion source on the BATMAN (BAvarian Test MAchine for Negative ions) located at the Institute for Plasma Physics (IPP) in Garching, Germany. The main differences between the two RF sources is the antenna geometry. The BATMAN type III source considered has an external antenna configuration, while the antenna on the DENISE RF system is housed in a quartz tube located in the centre of the discharge chamber, as described previously in Chapter Three.

The DC sources investigated were the filament driven source described previously on the DENISE system and the filament driven discharge source on the MANTIS (Multi Ampere NegaTive Ion Stand) source located at CEA, Cadarache. Descriptions of these sources are given here.

6.1 The KAMABOKO Source on MANTIS

The experimental system used in CEA Cadarache consists of an ion source, the KAMABOKO source, and a large cylindrical stainless steel chamber housing an accelerator, extractor and neutralizer system, the MANTIS system. The KAMABOKO source was developed by the Japan Atomic Energy Research Institute (JAERI) and currently resides at CEA-Cadarache for long pulse (1000 s) deuterium testing on the MANTIS test bed.

The KAMABOKO source has been described in detail in [3], a brief description is given here. It is a 30 litre semi cylindrical chamber of machined oxygen free copper. The plasma is powered via 12 tungsten filaments mounted on water cooled feedthroughs. Efficient confinement is achieved by 16 magnetic line cusps generated by Sm-Co magnets arranged longitudinally in machined channels on the outside of the chamber. The source is cooled by countersunk lines also on the outside of the source and situated next to the magnetic channels. Typically, 70 kW of arc power are injected into the source to create a plasma with density of 10^{13} cm^{-3} and an electron temperature of about 5 eV [4].

The extraction area is a rectangular plane measuring 250 x 340 mm cut into the side of the cylinder. A magnetic filter of up to 1800 G cm is achieved by placing magnets (additional to the line cusps) along the sides of the opening. The plasma grid has 45 holes, of 14 mm diameter each. These are arranged in a 7 x 7 matrix, excluding the 4 outer holes which are used for alignment of the three-stage acceleration system. The plasma grid is electrically and thermally isolated. Extracted beams of H^- or D^- are accelerated up to energies of 30 keV [4].

6.2 The RF Ion Source on BATMAN

The BATMAN type III system has a compact design with an external antenna and a Faraday screen integrated in the copper source body. The advantage of this compact source is that investigations of different magnetic field configurations and modifications of the RF antenna can be easily carried out. The source has a vacuum-tight, self supporting Faraday shield made of copper. RF power of up to 100 kW at a frequency of 1 MHz can be coupled to the external coil with six turns. The extraction system has three grids with a matrix of 4x12 holes of 11 mm diameter, arranged in an area of a 6x20 cm^2 and is mounted inside a modified PINI (Positive Ion Neutral Injector used at JET, the Joint European Torus) extraction structure. In order to reduce the electron current, a magnetic filter field is generated by two rows of Co-Sm permanent magnets placed close to the edge of the extraction area. The strength of the magnetic filter parallel to the plasma grid, integrated in the perpendicular direction to the plasma grid is 700 G cm. For the purpose of biasing the plasma grid with respect to the source, the front cover plate and the source body are connected to each other and isolated against the plasma grid. A fast-injection Langmuir probe is mounted at the centre of the backplate. [5]

The operation range on this source is limited to pressures > 0.5 Pa, as otherwise the ion current is below the detection limit. A schematic of the type III source is shown below in Fig. 6.1, together with the type II predecessor in which the function of the Faraday screen and the vacuum boundary are still separated.

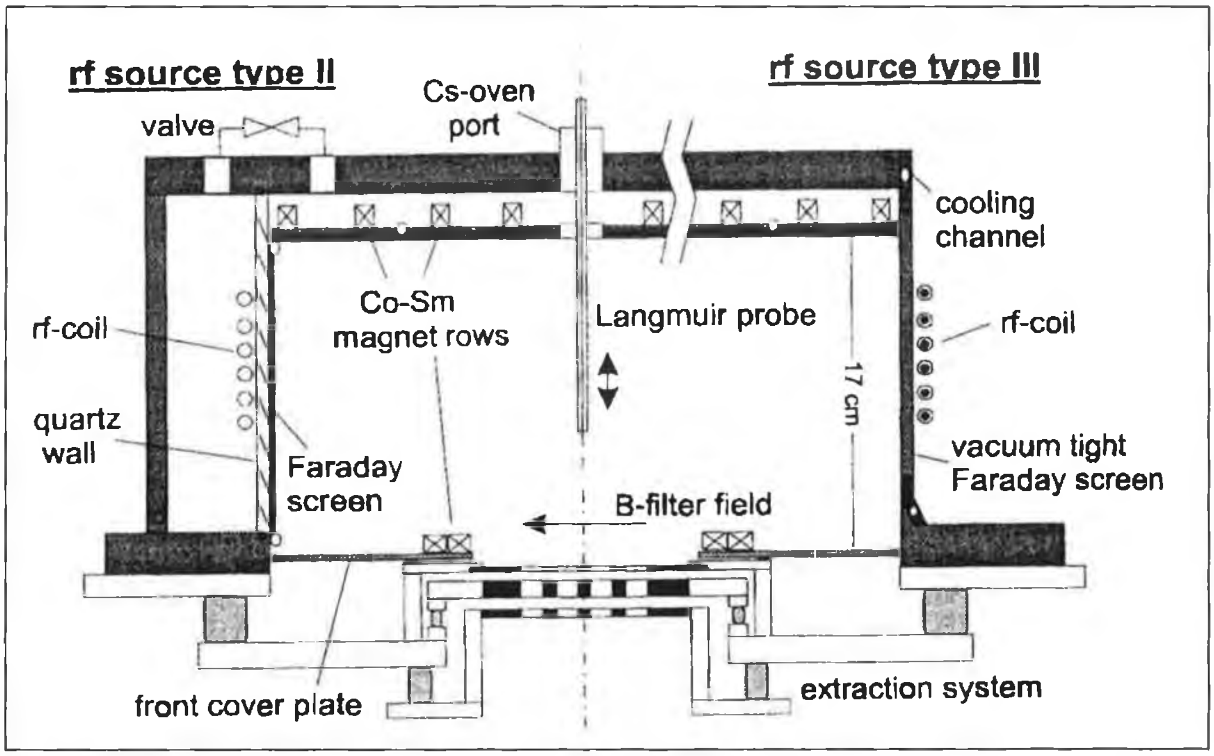

Fig. 6.1 **BATMAN Type III and II RF Ion Sources in Garching.**

6.3 DENISE RF and DC Multicusp Ion Sources

The plasma sources from the DENISE system have been described in detail in Chapter Three. In brief the DC source is a filament driven discharge which is magnetically confined. The RF source utilises an internal coil housed in a quartz tube to couple power to the plasma.

6.4 Diagnostics

On the DENISE ion sources plasma parameter measurements were carried out with the use of the Scientific Systems SmartProbe Langmuir probe technique [6], as described previously. Previous measurements were also carried out on this source to determine the negative ion densities with the use of the laser photodetachment technique described in detail in Chapter Three. This is the technique of Bacal and Hamilton [7] in which laser beam photons remove the attached electron form the negative hydrogen ions. It was shown that an increase in negative ion densities was apparent for low pressure mixtures of hydrogen and argon.[8]

The plasma parameters of the KAMABOKO source and the BATMAN ion sources were measured by a Scientific Systems fast- injection Langmuir probe technique. The theory of operation and analysis of this probe is the same as the one described earlier in Section 3.1. The main difference in these probes lies in the fact that the fast- injection probe is a modified SmartProbe on an automatic linear drive (ALD) which allows for a spatial scan of the whole source to be acquired in milliseconds. A modification to the electronics also allows for the collection of currents up to 2 A which is required in these hot plasma ion sources. This SmartSoft system allows for the acquisition of both temporal and spatial scans.

6.5 Plasma Parameters on the RF and DC Ion Sources in a Hydrogen/Argon Discharge

Increased percentages of Ar were added to a pure hydrogen discharge on the DC and RF ion sources on DENISE. In the DC filament driven source the overall source pressure was kept constant at 2 mTorr. The discharge voltage was kept at 70 V. Fig. 6.2 shows the increase in electron density as a function of increasing added percentages of Ar to the H_2 discharge for different discharge currents. A graph of the electron temperature as a function of the percentage addition of Ar is plotted in Fig. 6.3 below. It can be seen hat the electron temperature drops with the increasing amount of Ar in the gas mixture.

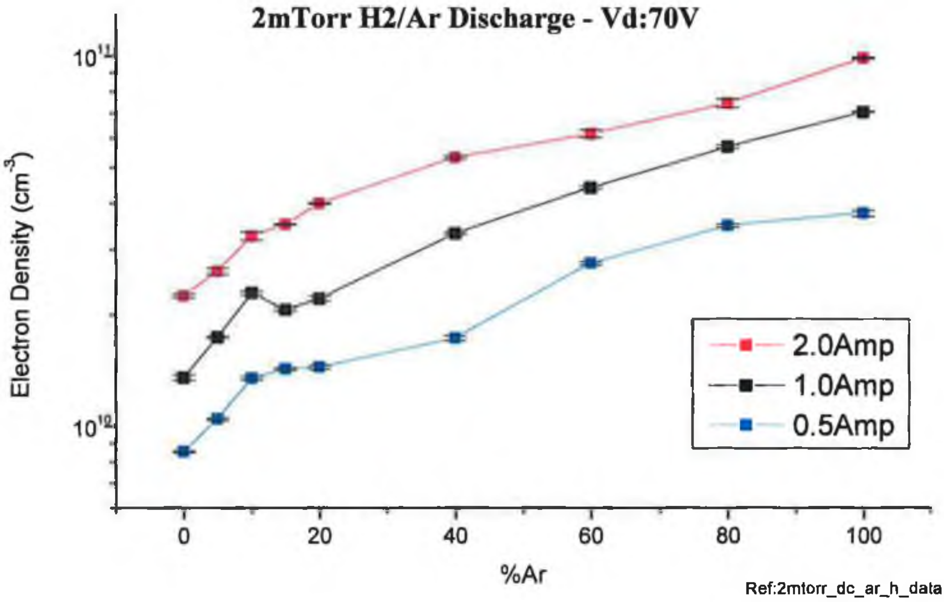

Ref:2mtorr_dc_ar_h_data.opj
11/9/98-NC/DB

Fig. 6.2 Variation in Electron Density with Addition of Ar.

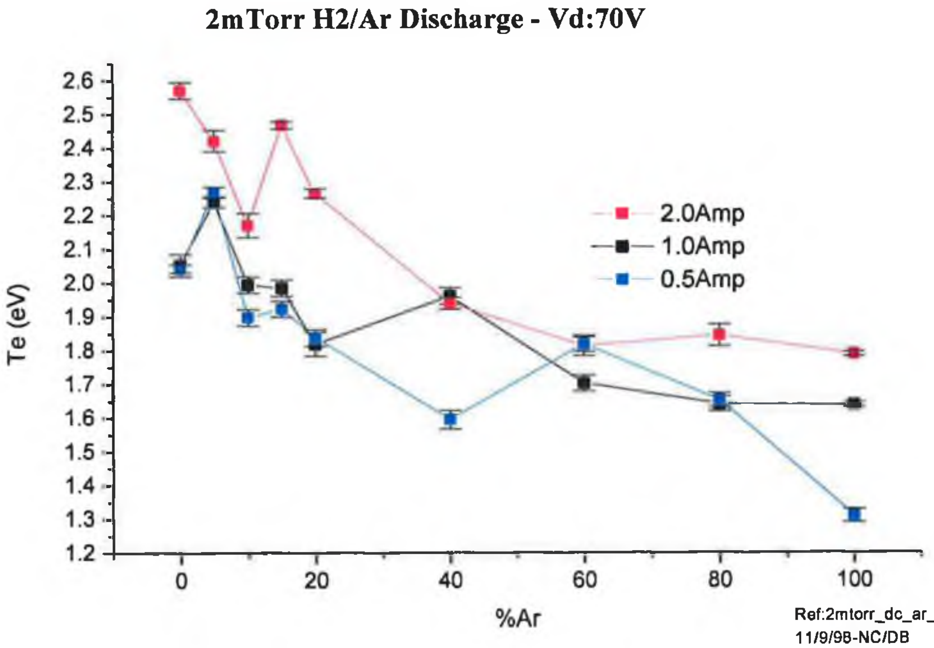

Ref:2mtorr_dc_ar_h_data.opj
11/9/98-NC/DB

Fig. 6.3 Variation in Electron Temperature with Addition of Argon.

The increase in the electron density collected by the probe with increased percentage addition of Ar to the plasma is expected as it reflects the lower ionization cross-section of hydrogen in comparison with argon.

The decrease in electron temperature is also expected as the mass of the Ar atom is 40 amu while that of the hydrogen atom is 1 amu. As the electron density increases the number of collisions also increases therefore reducing the overall electron temperature. In Fig. 6.4 and 6.5 a similar trend is seen in the RF source, the increased electron density and the decreased electron temperature.

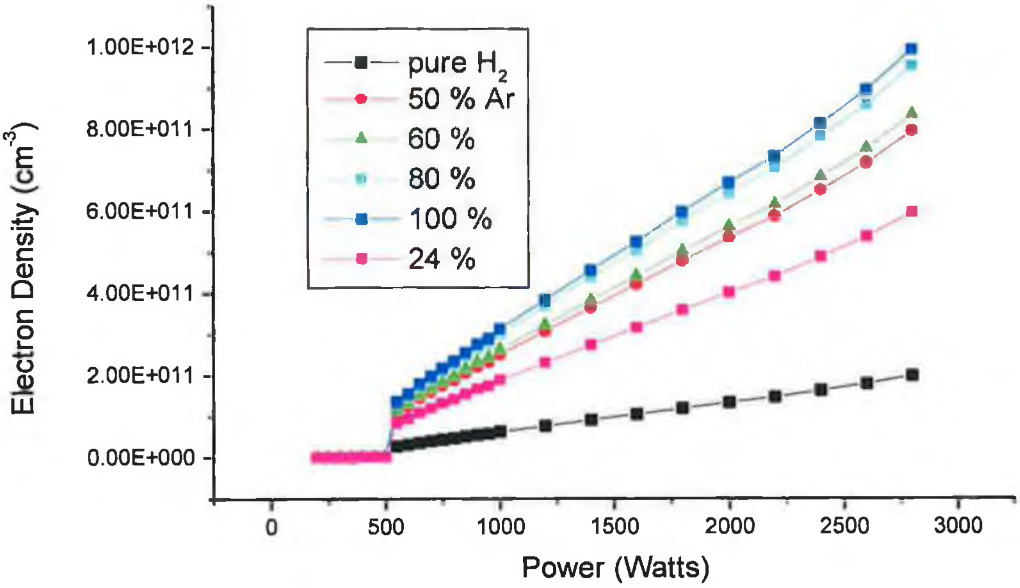

Fig. 6.4 **Variation in Electron Density as a Function of Power with Increasing Ar Percentage.**

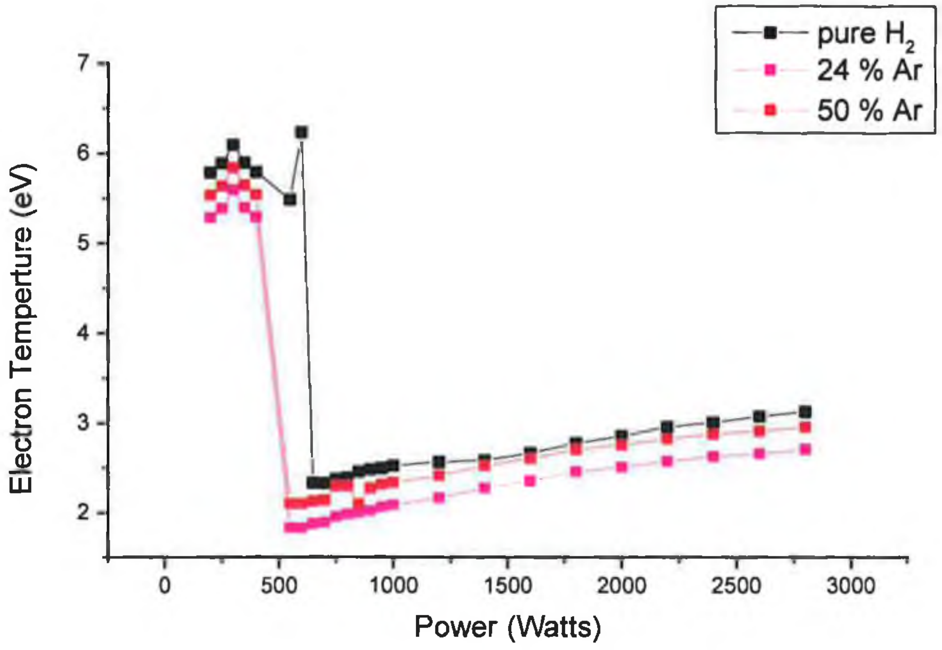

Fig. 6.5 **Variation in Electron Density as a Function of Power with increasing Ar percentage.**

6.6 EEDF Results on the DC Ion Source on DENISE

Examination of the EEDF in the low pressure, 2 mTorr, pure hydrogen DC discharge with 1.5 A discharge current and 70 V discharge voltage, shows strongly bi-maxwellian distributions, Fig. 6.6. This bi-maxwellian can be considered as the sum of two maxwellian distributions, which can be characterised by different electron temperatures, $T_{e\ cold}$ and $T_{e\ hot}$. This can be seen in the following equation, *Equation 6.1*

$$f(u) = n\left(\frac{m}{2\pi kT_e}\right)^{3/2} \exp\left(-\frac{mu^2}{2kT_e}\right) \qquad \textit{Equation 6.1}$$

A calculated value for both $T_{e\ cold}$ and $T_{e\ hot}$ can be obtained by fitting a component on a graph of the EEDF with a natural logarithmic scale. The temperature that each line represents can be evaluated from the slopes of the lines using a slope of $-1/T$. In the case of Fig. 6.2 the colder distribution of electrons have a temperature of $T_{e\ cold} = 1.04$ eV and the hotter distribution corresponds to an electron temperature of $T_{e\ hot} = 3.36$ eV. Getting the integral under each distribution results in the determination of the electron density of each population which also leads to the ratio of hot to cold electrons. For the graph of the EEDF in Fig. 6.5 it was found that the colder distribution has an electron density of 6.31 x 10^9 cm^{-3} and the hotter distribution a density of 4.42 x 10^8 cm^{-3}. The ratio of the densities then is determined to be approximately 14:1, which shows a lower population of hot electrons in the distribution.

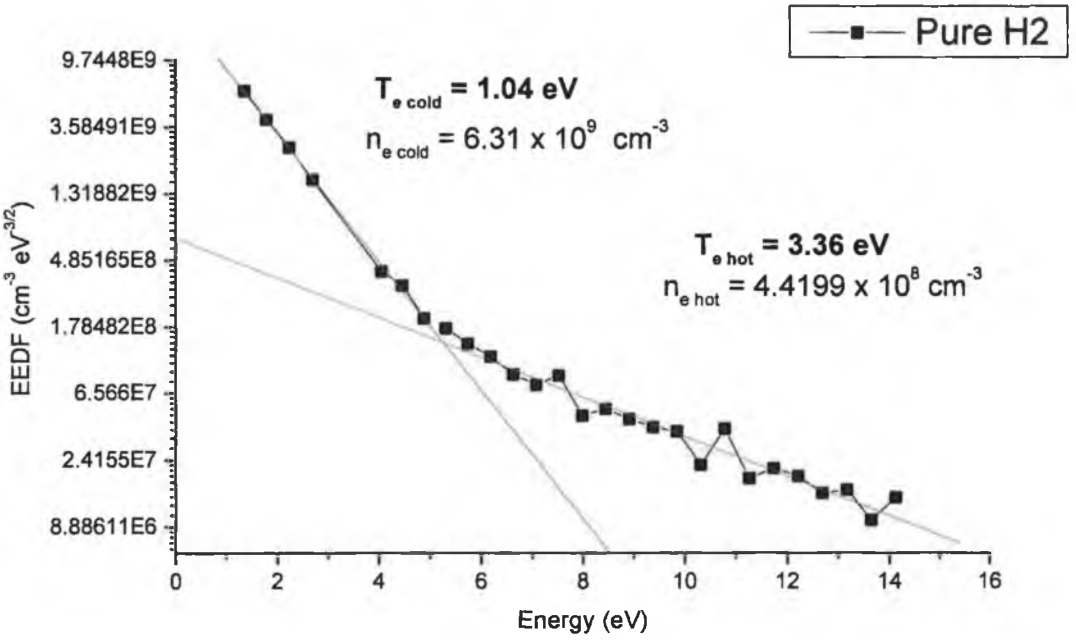

Fig. 6.6: Graph of Electron Energy Distribution Function (EEDF) for a 70 V, 1.5 A Hydrogen Discharge at 2 mTorr.

Electron energy distribution functions of a mixture of argon and hydrogen were then examined. The total fill pressure was always kept constant, in this case at 2 mTorr, with partial pressures of argon at 10 %, 20 %, 50 %, 80 % and 100 % of the total pressure. On addition of argon to this discharge it was noted that the density of hot electrons decreased. The temperatures of the hot and cold electrons were again calculated as for the previous distribution, and the densities found by integrating under each component distribution. Figs. 6.7 to 6.10 illustrate the effect of the argon on the hydrogen discharge. In Fig 6.7, the EEDF of a 2 mTorr hydrogen plasma with a partial pressure of 10 % argon with a discharge current of 1.5 A and 70 V is shown. The EEDF still maintains the bi-maxwellian distribution function, however on calculation of the densities of the hot and cold electrons it can be seen that the ratios have changed slightly. The two different temperature regimes were identified and determined. $T_{e\ cold}$ was found to be 1.15 eV and $T_{e\ hot}$ 3.21 eV. Not much of a temperature difference is seen. However on calculation of the densities, $n_{e\ cold}$ was found to be 7.3 x 10^9 cm^{-3} and $n_{e\ hot}$ 4.10 x 10^8 cm^{-3}. The ratio in this case is then ~18 : 1, which means that there are 18 times more cold electrons than hot electrons in the plasma.

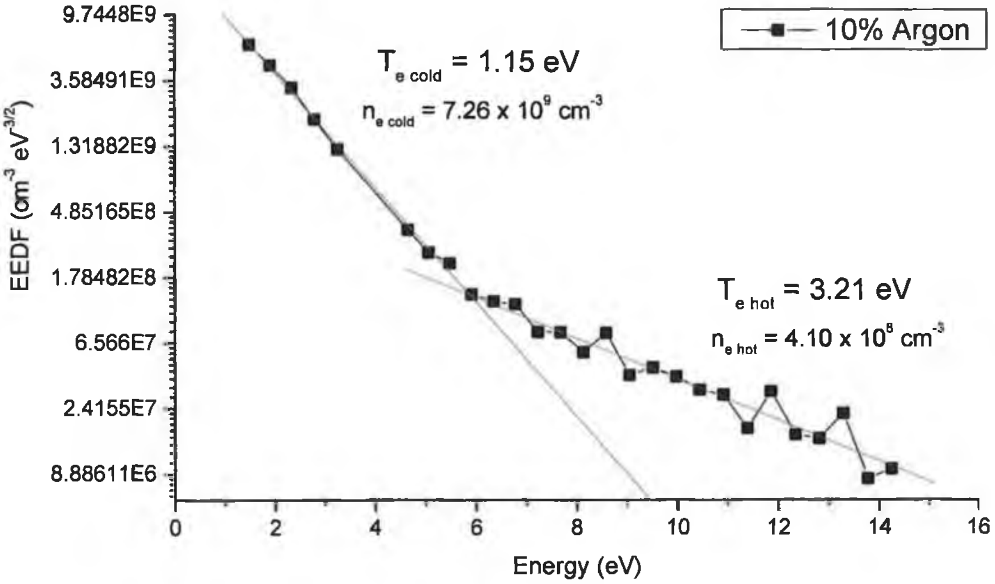

Fig. 6.7 **Graph of Eletron Energy Distribution Function (EEDF) for a 2 mTorr, 70 V, 1.5 A, Hydrogen Discharge with 10% Argon Added.**

On increasing the percentage of added argon from a partial pressure of 10 % to 50 %, the ratio of cold to hot electrons is seen to change dramatically. The density of cold electrons has increased significantly, and the ratio of cold to hot electrons is calculated to be 58 : 1. This can be seen in Fig. 6.8 below.

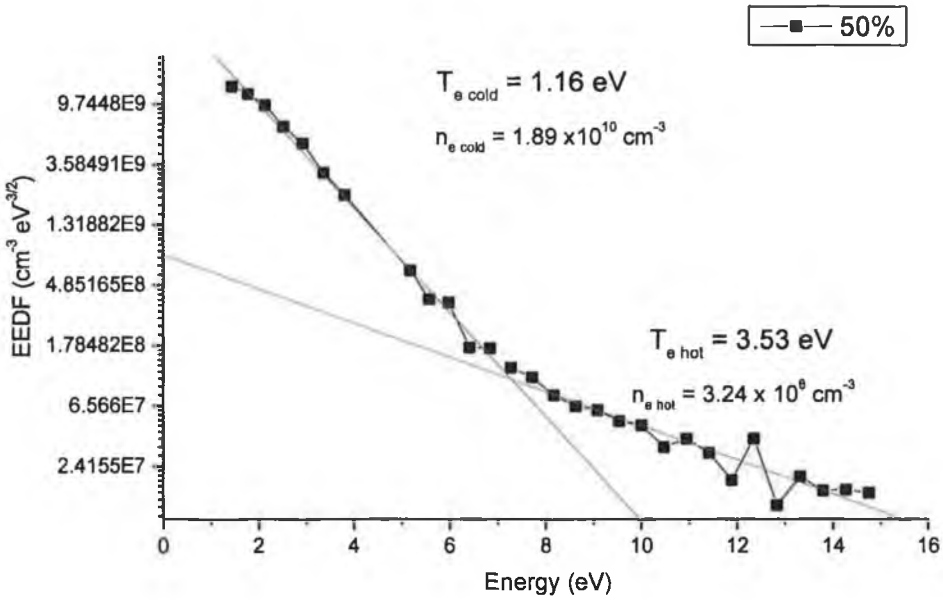

Fig. 6.8 Electron Energy Distribution Function (EEDF) for a 2 mTorr, 70 V, 1.5 A, Hydrogen Plasma with 50% Argon Added.

Increasing the argon percentage added to the hydrogen discharge to 80 % as shown below in Fig. 6.9 again cools the plasma down significantly and the distribution ratio of cold to hot electrons becomes 100:1. The density of cold electrons is calculated to be 2.23 x 10^{10} cm^{-3} and the density of hot electrons in the distribution is calculated to be 2.23 x 10^{8} $cm^{-3.}$ However on examinning the EEDF's with increasing percentage compositions of argon in the hydrogen discharge it is clear that the distributions are becoming less and less bi-maxwellian until at 100% Ar with 0% hydrogen the distribution returns to the characteristic maxwellian shape. This can be seen below in Fig 6.10.

The transition from bi-maxwellian to maxwellian is illustrated clearly when comparing the EEDF's collected from pure hydrogen and pure Ar discharges. This is shown in Fig. 6.11.

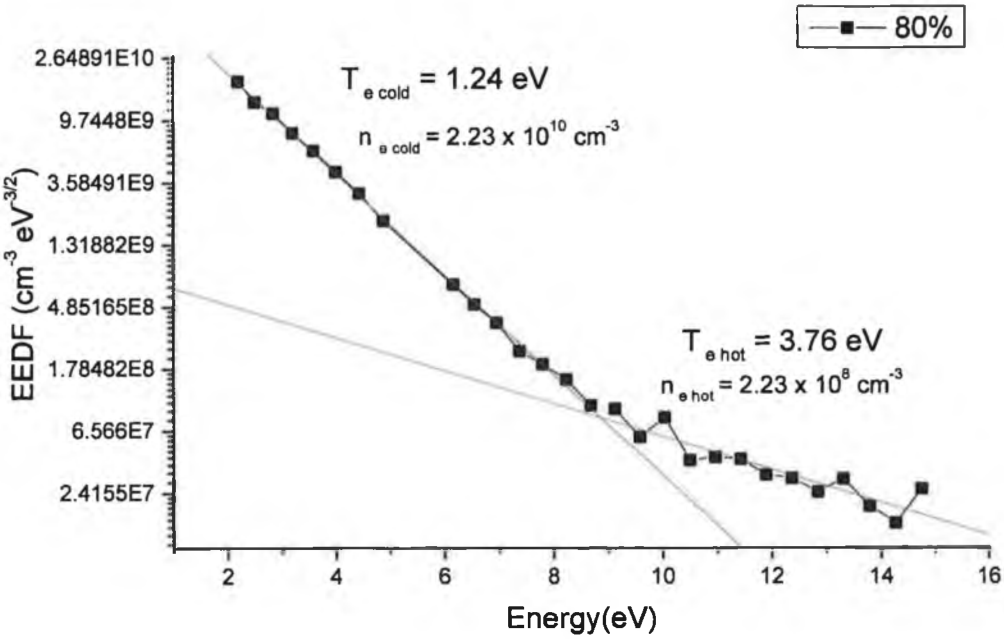

Fig 6.9 **Electron Energy Distribution Function (EEDF) for a 2 mTorr, 70 V, 1.5 A, Hydrogen Plasma with 80 % Argon Added.**

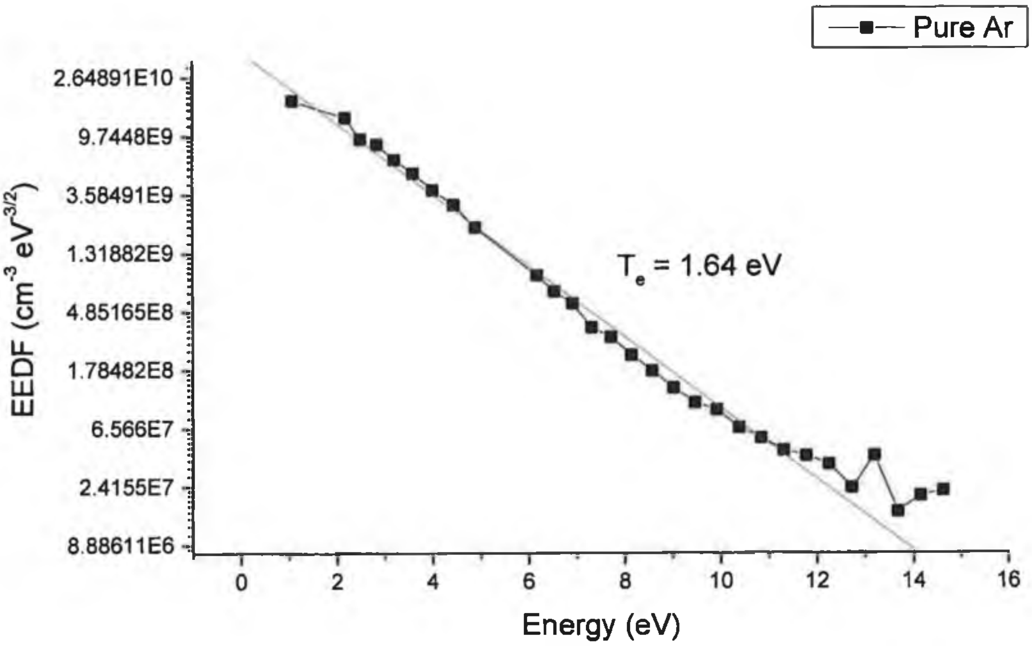

Fig. 6.10 **Electron Energy Distribution Function (EEDF) for a 2 mTorr, 70 V, 1.5 A, Argon Plasma with 0 % Hydrogen Added.**

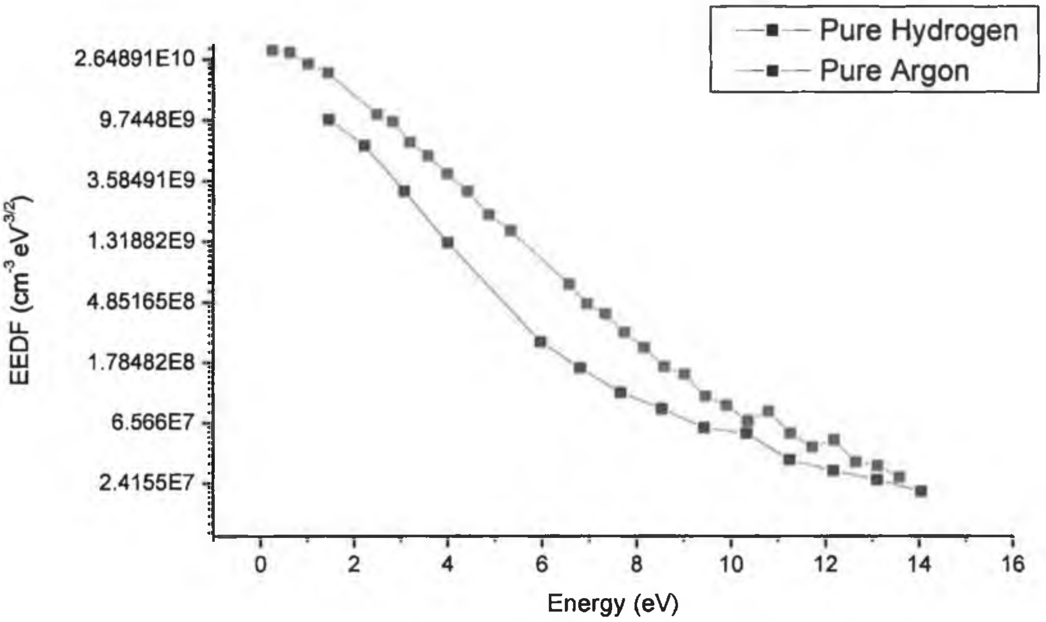

Fig. 6.11 Comparison of EEDF's Collected in Pure Hydrogen and Pure Argon Discharges (the bi-maxwellian observable in the hydrogen discharge is not seen in the argon discharge).

6.7 Plasma Parameter Measurements on the BATMAN Type III RF Ion Source

As with the experiments on the DENISE system in DCU, a similar experiment was carried out on the RF ion source on the BATMAN system in IPP Garching. The probe used in this case was a fast-injection probe described earlier. A temporal scan was collected in a 7 mTorr hydrogen discharge at 70 kW. After 600 ms a percentage of argon was injected into the source. The overall source pressure therefore had increased. It was not possible to keep the pressure constant and vary the mixtures of the two gases on this system. Figures 6.12(a) and (b) below show that the addition of 14 % Ar after 600 ms into a 7 mTorr hydrogen discharge had an immediate effect on the increase of the electron density. This increase could be an effect of the argon but it cannot be excluded that it is just a consequence of the overall increase in the source pressure reflecting the increase in neutrals in the chamber undergoing collisions. On addition of 16 % argon to a 7 Torr hydrogen discharge the source pressure has increased to approximately 8 mTorr.

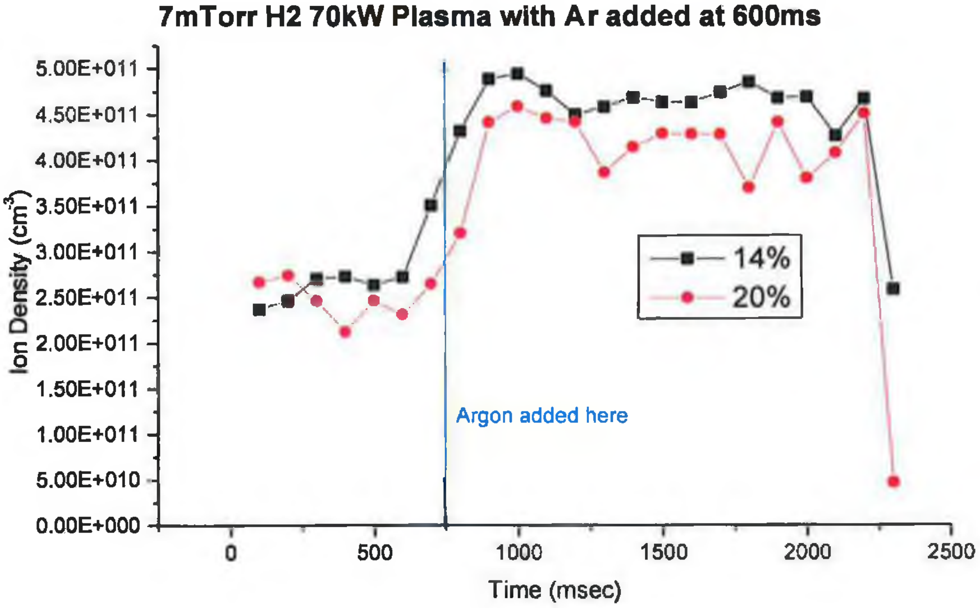

Fig. 6.12(a) **Increased Ion Density upon Addition of Ar at 600 ms.**

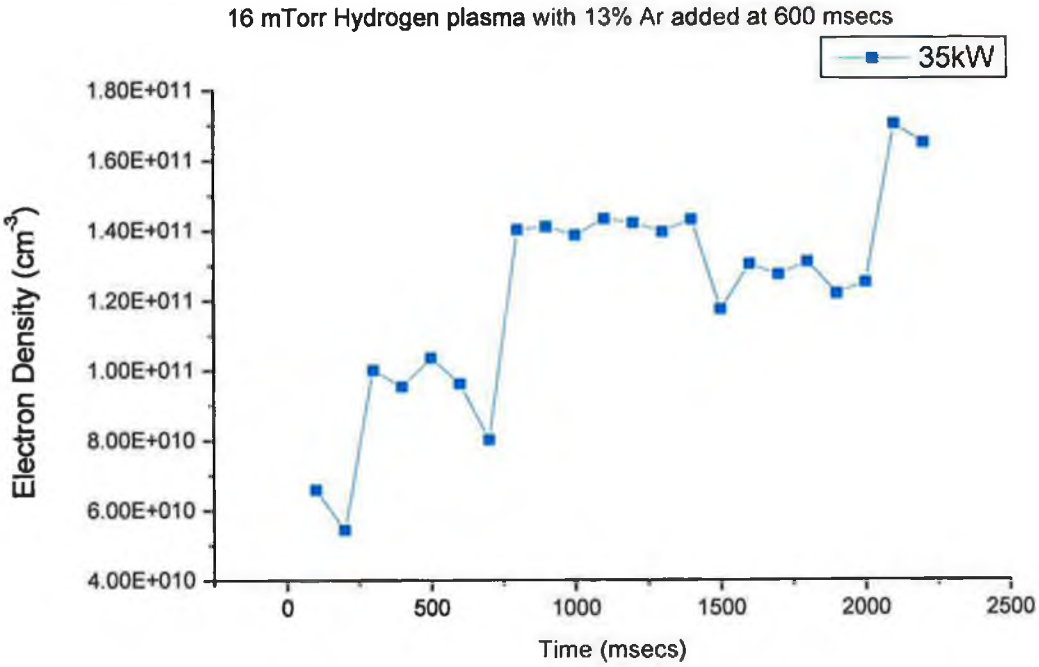

Fig. 6.12(b) **Increased Electron Density upon Addition of Ar at 600 ms.**

6.8 Plasma Parameter Measurements on the MANTIS System

The following two graphs shown in Fig. 6.13 and 6.14 below, show the effect of Ar addition to a hydrogen filament driven discharge on the KAMABOKO ion source on MANTIS. The increased electron density due to the lower ionisation energy of argon is not observable in this source. Also the decrease in electron temperature is not seen.

This source was operated at lower pressures than any of the other sources investigated. It is thought that the optimisation effect observable in the other sources is not evident here as the source is so well confined and already operating at its optimum.

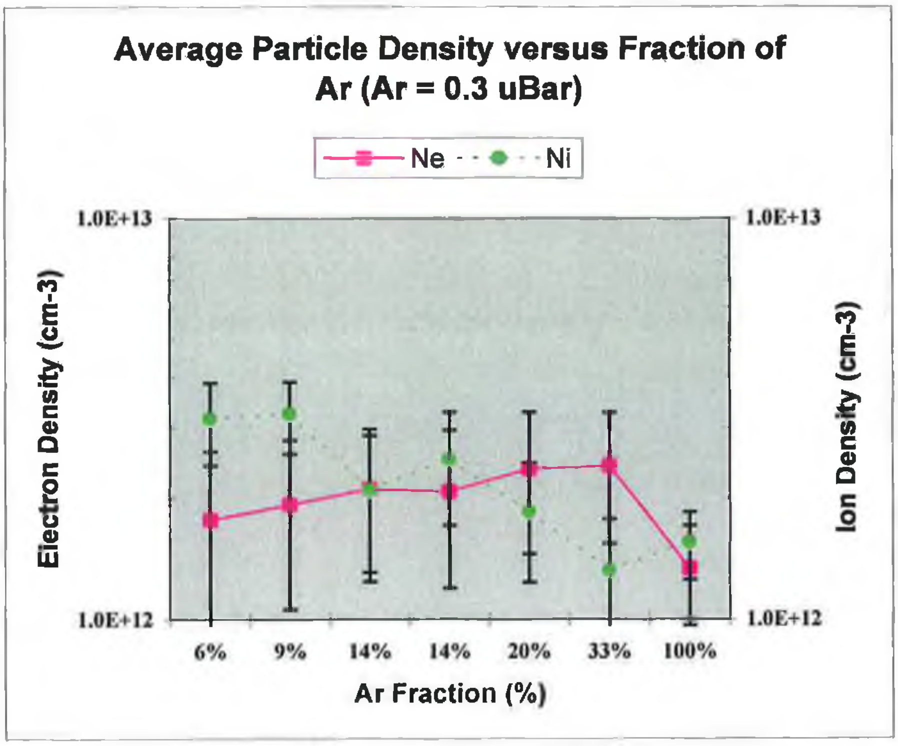

Fig. 6.13 Electron and Ion Densities as a Function of Ar Admixture.

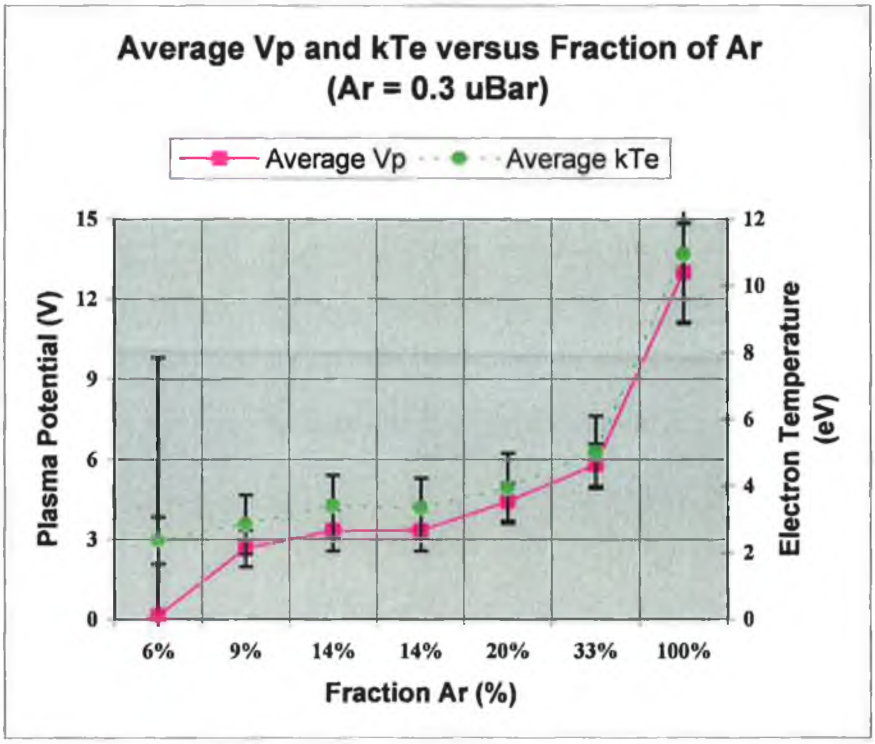

Fig. 6.14 **Plasma Potential and Electron Temperature as a Function of Ar Admixture.**

As stated previously the processes that lead to the production of negative ion in the hydrogen discharge rely heavily on dissociative attachment to vibrationally excited hydrogen molecules.

$$e^- + H_2(v'' > 3) \rightarrow H_2^- \rightarrow H^- + H^+ \qquad \textit{Equation 6.2}$$

The vibrationally excited hydrogen molecules are a result of a 2-step process, which involves the excitation of the hydrogen atom in the ground state to an excited electronic state, followed by the radiative decay to the vibrationally excited level of the ground state, this process has been explained in Chapter One.

In an attempt to enhance the production rate of negative hydrogen ions, the above reactions were utilised to alter the plasma conditions favourably. As can be seen from the Langmuir probe measurements which determined the plasma parameters shown in the different systems investigated, the effect of the addition of the noble gas argon to the hydrogen discharge altered conditions favourably by increasing the electron density and decreasing the electron temperature. Previously reported work has shown an increase in negative ion beam extraction in large multicusp sources with the addition of argon and xenon at low pressures. [2, 3]

6.9 Negative Ion Measurements in H/Ar Discharges

In an effort to determine the effect of the addition of Ar to the H_2 discharge, negative ion yield measurements were made by use of the laser photodetachment technique. These results are shown below for the DC ion source on DENISE. There are no negative ion measurements carried out on the MANTIS or BATMAN systems as these systems did not facilitate this diagnostic. Fig. 6.15 shows the n_- / n_e ratio as a function of the percentage Ar added into a 2 mTorr discharge. As before the total pressure was kept constant at all times in this experiment at 2 mTorr. Fig. 6.16 shows the calculated negative ion densities for this discharge.

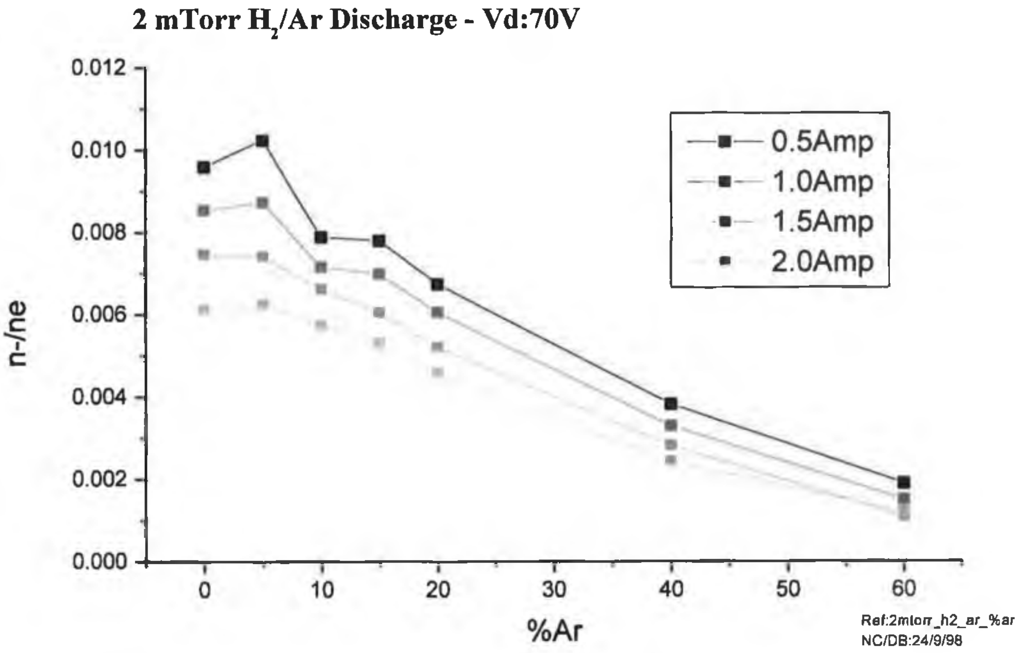

Fig. 6.15 **n_- / n_e Ratio as a Function of Added Percentages of Argon.**

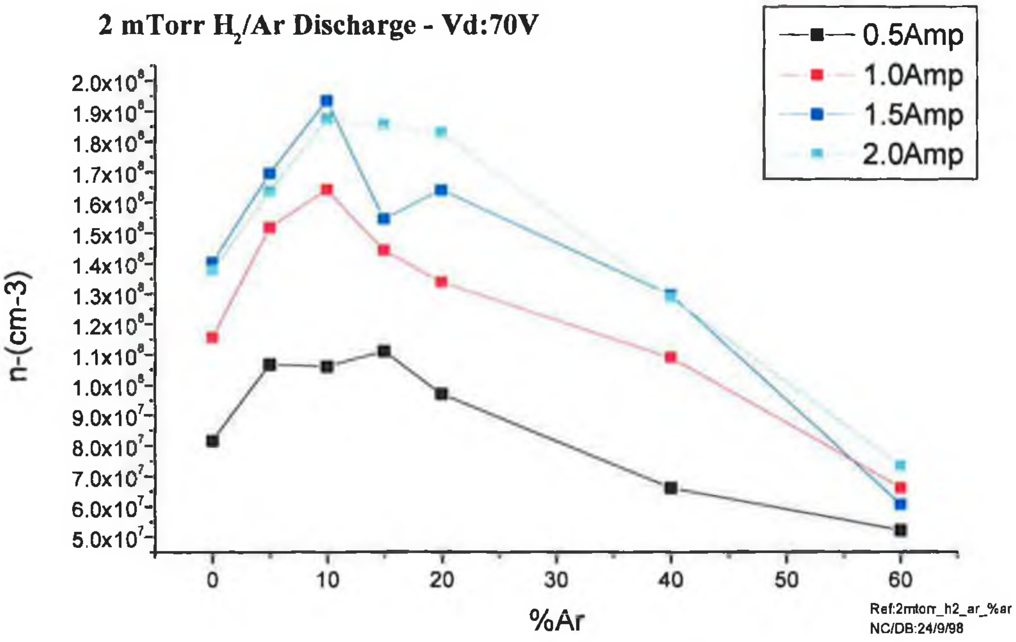
2 mTorr H_2/Ar Discharge - Vd:70V

Ref:2mtorr_h2_ar_%ar
NC/DB:24/9/98

Fig. 6.16 **Measured Negative Ion Densities with Increased Added Percentages of Argon.**

With low percentage additions of Ar to the 2 mTorr hydrogen discharge it can be seen that the negative ion density is enhanced. Addition of up to 20 % Ar shows a significant increase in the densities measured.

The threshold for the production of excited vibrational states of H_2 is 12.4 eV. Therefore the electrons which are required for the production of the vibrationally excited H_2 are not effected significantly by the addition of argon. However, the DA process which is the main process for the production of H^- has an increasing cross-section and decreasing threshold with increasing v. Wadhera et al have shown that the cross-section near threshold increases by five orders of magnitude between $v = 0$ and $v = 7$ while the threshold energy decreases from 3.75 eV to less than 1 eV [9].

This leads to the conclusion then that the DA process which is responsible for the production of the H- is largely dependent on variation in the electron temperature.
The effective DA rate is given by the following equation when ignoring rotational level excitation

$$\langle \sigma u \rangle_{eff} = \frac{N_0}{N}\langle \sigma_0 u \rangle + \frac{N_1}{N}\langle \sigma_1 u \rangle + \frac{N_2}{N}\langle \sigma_2 u \rangle + \ldots\ldots\ldots \frac{N_n}{N}\langle \sigma_n u \rangle \qquad \text{Equation 6.3}$$

where σ_n is the DA cross-section for the nth vibrational level, and its population density is given by N_n and N is the population density of the molecular hydrogen.

Fig. 6.17 shows the reaction rate of DA as a function of the electron temperature for the vibrational state of $v'' = 5$. The reaction rate coefficient values were obtained by fitting to cross-sections calculated by Wadehra and Bardsley [5]. A listing of the cross-sections used is shown in Appendix C.

Also in this plot is the reaction rate for the electron detachment process which is the dominant loss mechanism. The reaction rates were calculated using the cross-sections published by Bailey et al. The rate coefficients are calculated in both cases, DA and CD processes by the method explained previously in Chapter 5.

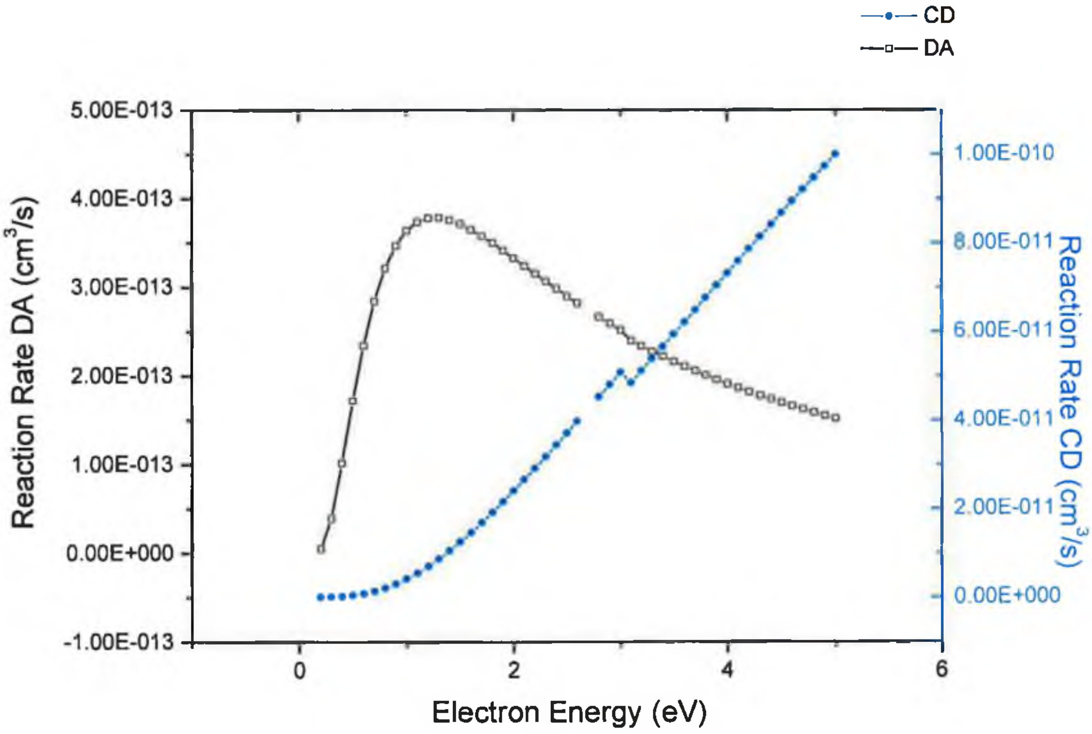

Fig. 6.17 **Reaction Rates for DA and ED as a Function of Electron Temperature.**

From this graph Fig. 6.16 is can be seen that the best condition of DA occurs slightly above 1 eV. Also from this graph it can be seen that the loss process of electron detachment increases when temperatures above 1 eV are reached.

It is suggested that the effect that the argon has on the production of negative ion in the hydrogen discharge is due to the increased electron density, as the argon is more easily ionized than the hydrogen and also because of the fact that the electron temperature has been lowered to a range where the DA process is optimized and the electron detachment process is at a minimum.

When the source pressure is increased, the effect on the electron density and the electron temperature is very small and therefore little increase in the negative ion production mechanism is observable.

6.10 Conclusion

Adding argon to a hydrogen discharge in the DENISE sources it is found that the effect on the plasma parameters is an increase of the electron density and a decrease of the electron temperature. It is suggested that the increase in the electron density is due to the lower ionization potential of argon than that of hydrogen. The increase in the negative ion density resulting at low pressures for low admixtures of argon and hydrogen is thought to be due to this increased electron density and decreased electron temperature which provides optimum conditions for the main production mechanism of DA and low reaction rates for electron detachment.

Unfortunately, the above explanation can not directly be applied to the results obtained from the type III source on BATMAN as the effect is disturbed by a non-constant total pressure. However, meanwhile the existence of a substantial enhancement due to argon (plus caesium) admixture has been clearly demonstrated on BATMAN using a different type of RF source. This source operates very reliably and has the potential for long pulse operation. Current densities up to 15 mA/cm^2 could be extracted at a source pressure of 0.65 Pa. By pure volume production 9 mA/cm^2 current density at the same pressure level has been achieved with the addition of Ar to the source operating gas. [10]. Recently 19 mA/cm^2 has been reported as extracted from this source. [11].

Why the "argon effect", i.e. the electron density increase and the electron temperature decrease thought responsible for an enhanced negative ion yield, is not observed in the KAMABOKO source on MANTIS remains unexplained for the time being.

References

[1] Leung K, Ehlers, K, Pyle R,
Rev. Sci. Instrum. 56, p2097, 1985

[2] Walther S, Leung, K, Hunkel, W
J. Appl. Phys. 64, p3424, 1988

[3] Miyamoto, N., Oguri, H., Okumura, Y., Inoue, T., Fujiwara, Y., Miyamoto, K., Nagase, A., Ohara, Y., and Watanabe, K.,
7th International Symposium on the Production and Neutralisation of Negative Ions and Beams, Brookhaven National Laboratory, Oct. 1995.

[4] Jacquot, C., Riz, D., Trainham, R., Miyamoto, K., Okumura, Y., and Hopkins, M.B
Proc. of the 19th Symp. on Fusion Techn., Lisbon 1996.

[5] Shoji T, Sakawa Y, Nakazawa, S, Kadota, K., and Sato, T.,
Plasma Sources Sci. Technol. 2, 5 1993.

[6] Hopkins, M.B., Graham, W.,
Rev. Sci. Instrum. 57, p2210, 1986

[7] Bacal, M., Hamilton, G.,
Phys. Rev. Lett. 42, p1538, 1979

[8] Curran, N.P, Hopkins, M.B.,Vender, D, James, B.W.
Plasma Sources Sci. Technol. 9 (2000) p169-175

[9] Wadehra J., and Bardsley, J.
Phys. Rev. Lett. 41, p1795, 1978

[10] Vollmer O. et al.,
Rev. Sci. Instrum. 71 (2), p939, 2000

[11] McNeeley P.
Private communication.

Conclusion and Future Work

Summary and Conclusion

A comprehensive investigation of negative ion production in multicusp ion sources of interest for neutral beam heating applications in proposed nuclear fusion reactors has been conducted using different diagnostic methods. The main diagnostics used in this work were the Langmuir probe and the laser photodetachment technique. Discharges in an RF ion source and a filament driven ion source were compared using the same discharge chamber.

Both ion sources were characterized by the use of the Langmuir probe technique to evaluate plasma parameters. Determination of the plasma parameters, the electron temperature, ion density , plasma potential, floating potential and electron energy distribution functions were carried out in both continuons and temporally modulated modes of operation of both ion sources. The effect of the application of an exteral applied magnetic field was studied and the magnetic field modeled. An increased efficiency was found by the application of such a field and its effect in particular on the radial dependence of the electron densities and temperatures was investigated.

The concept of a temporal filter was examined with a view to increase the negative ion yield from the afterglow of a temporally modulated RF discharge. The effect of temporal modulation on the plasma parameters was investigated. Information on the electron densities and temperature, floating potentials and EEDF's in the modulated discharge were collected. Power dependence and duty cycle were examined and it was found that the EEDF of the discharge could be controlled by modulating the frequency and the duty cycle. With greater control of the EEDF in the discharge it was proposed that also greater control of the production mechanisms and destruction mechanisms for negative hydrogen ions may be achieved. In the afterglow of the pulsed discharge a significant decrease in electron temperature was observed for relatively high electron densities. These characteristics are ideal for the production of negative ions, as the main destruction mechanism CD is no longer dominant in the afterglow and is practically negligible. The main production mechanism of DA is at an optimum at these low electron temperatures.

The negative ion densities were then determined by use of the laser photodetachment technique. The data collected verified the enhancement in negative ion densities in the post discharge of a filament driven discharge. Spatial dependence studies indicated a strong increase in density in the center of the discharge. The RF ion source was examined in pulsed mode of operation and negative ion densities were determined as a function of time in the afterglow. Comparison between the RF and filament driven discharges shows that the DC discharge of the same plasma density modulated at the same duty cycle produces a higher density of negative ions than the RF ion source. It was also seen that the density of negative ions in the source could be increased with modulation of the discharge at different duty cycles. The reaction rates for the production and destruction mechanisms of H^- were determined and a model of the processes acting in the production of negative ions written. The negative ion density was calculated for the afterglow of a 20 mTorr H_2 plasma, the density profile being in good qualitative agreement with the experimental data.

Having determined the negative ion densities in both volume ion sources in pure hydrogen, the addition of argon to the discharge was then investigated. On addition of argon to a hydrogen discharge it was found that the effect on the plasma parameters was an increase in the electron density in the discharge and a decrease in the electron temperature. It is suggested that the increase in electron density is due to the lower ionisation energy of argon compared to hydrogen. Negative ion densities were then determined from a hydrogen discharge with an admixture of Argon and an increase in negative ion density was determined. The increase is thought to be due to the lowering of the electron temperature providing optimum conditions for the main production mechanism of dissassociative attachment and resulting in low reaction rates for electron detachment, the assumed main destruction mechanism for H^-. Plasma parameters were determined on both RF and filament discharges of the DENISE system on the filament driven Japanese KAMABOKO ion source at Cadarache and on the type III RF ion source of the BATMAN experiment in Garching.

In conclusion, the RF ion source has been shown to operate efficiently as a volume ion source with the application of a magnetic confining field to a temporally modulated discharge. However, the "generation specific" effect that the RF driven discharge yields less negative ions than a filament driven one at the same plasma density is unexpected and deserves further investigation.

Admixtures of argon prove successful in enhancing the negative ion yield in some sources. From the point of view of NBI application this is very important as it could eliminate the need of caesium seeded ion sources which add to the complexity of the systems. While the explanation for the enhancement being due to the (observed) increase in electron density and decreased electron temperature appears plausible for the DENISE sources it remains unexplained why a similar effect is not observed in the KAMABOKO source on MANTIS.

Future Work

The next stage for the development of this work is the investigation into the extraction of a negative ion beam from the RF temporally filtered discharge. This could not be performed on the DENISE system due to an operational malfunction of the cryopump resulting in a source pressure that was to high to efficiently extract an ion beam due to beam stripping. Some measurements on the extraction of this system were attempted [1]. Initial investigations into the design of different antenna was also carried out and comparisons in electron densities determined on changing the number of turns on the antenna, and on coating the antenna with a film of gold. [2] It is thought that the efficiency of the source could be increased by the use of different antenna designs. Much work needs to be carried out in this area and an investigation of the skin dept on such coils by use of a B.DOT probe would be an area of interest.

An advanced negative ion measurement technique based on cavity ring-down spectroscopy is proposed to determine negative ion densities in the RF discharge. This technique relies on monitoring the time decay of a laser pulse signal which undergoes multiple passes through the chamber. The degree of interaction between the laser pulse and the plasma is determined from the ring-down time of the pulse. This is considered an accurate technique and has been used for H^- diagnostics with great success [3, 4, 5].

References.

[1] Boilson D, Curran N, McNeely P, Hopkins M and Vender D
14th ESCAMPIG, Malahide, Ireland 1998, p358.

[2] Boilson D, Curran N, McNeely P, Hopkins M and Vender D
Joint Development Committee Meeting, Dublin, Ireland, 1998

[3] Romanini D, Kachanov, A, Sadeghi N, and Stoeckel F.
Chem Phys Lett. 264 p316 1998.

[4] Campargue, A, Romanini D, and Sadeghi N,
J. Phys. D: Appl Phys. 31 pl 168, 1998.

[5] Quandt E.
Private Commumication, 1998.

Appendix A

Modelling the magnetic Field with the POISSON/SUPERFISH Programme (Structure Code.)

Bucket Confining Magnet Structure 3 of 12 magnets DC filament source geometry

```
&reg kprob=0,dx=.25, dy =.25, mode=0,nbslo=0,
xmin=-15.0,xmax=15.0,icylin=0
ymin=-15.0,ymax=15.0, &

&po x=  -15.0,y=  -15.0 &
&po x=  -15.0,y= 15.00 &
&po x= 15.00,y= 15.00 &
&po x= 15.00,y=  -15.0 &
&po x=  -15.0,y=  -15.0 &

&reg mat=2,mshape=1,mtid=1 &
&po r=9, theta=356.82 &
&po r=10, theta=356.82 &
&po r=10, theta=3.18 &
&po r=9.0 ,theta=3.18 &
&po r=9.0 ,theta=356.82 &

&reg mat=3,mshape=1,mtid=2 &
&po r=9,theta= 26.82 &
&po r=10,theta=26.82 &
&po r=10,theta=33.18 &
&po r=9,theta=33.18 &
&po r=9,theta= 26.82 &

&reg mat=4,mshape=1,mtid=3 &
&po r=9,theta= 56.82 &
&po r=10,theta=56.82 &
&po r=10,theta=63.18 &
&po r=9,theta=63.18 &
&po r=9,theta= 56.82 &

&reg mat=5, mshape=1, mtid=4 &
&po r=9,theta=  86.82  &
&po r=10 ,theta= 86.82 &
&po r=10,theta= 93.18 &
&po r=9,theta=93.18 &
&po r=9 ,theta=86.82 &

&reg mat=6, mshape=1, mtid=5 &
&po r=9,theta=  116.82  &
&po r=10 ,theta= 116.82 &
&po r=10,theta= 123.18 &
&po r=9,theta= 123.18 &
&po r=9 ,theta= 116.82 &

&reg mat=7, mshape=1, mtid=6 &
```

```
&po r=9,theta=  146.82  &
&po r=10 ,theta= 146.82 &
&po r=10,theta= 153.18 &
&po r=9,theta=153.18 &
&po r=9 ,theta=146.82 &

&reg mat=8, mshape=1, mtid=7 &
&po r=9,theta=  176.82  &
&po r=10 ,theta= 176.82 &
&po r=10,theta= 183.18 &
&po r=9,theta=183.18 &
&po r=9 ,theta=176.82 &

&reg mat=9, mshape=1, mtid=3 &
&po r=9,theta=  206.82  &
&po r=10 ,theta= 206.82 &
&po r=10,theta= 213.18 &
&po r=9,theta= 213.18 &
&po r=9 ,theta= 206.82 &

&reg mat=10, mshape=1, mtid=2 &
&po r=9,theta=  236.82  &
&po r=10 ,theta= 236.82 &
&po r=10,theta= 243.18 &
&po r=9,theta= 243.18 &
&po r=9 ,theta= 236.82 &

&reg mat=11, mshape=1, mtid=8 &
&po r=9,theta=  266.82  &
&po r=10 ,theta= 266.82 &
&po r=10,theta= 273.18 &
&po r=9,theta= 273.18 &
&po r=9 ,theta= 266.82 &

&reg mat=12, mshape=1, mtid=6 &
&po r=9,theta=  296.82  &
&po r=10 ,theta= 296.82 &
&po r=10,theta= 303.18 &
&po r=9,theta=303.18 &
&po r=9 ,theta=296.82 &

&reg mat=13, mshape=1, mtid=5 &
&po r=9,theta=  326.82  &
&po r=10 ,theta= 326.82 &
&po r=10,theta= 333.18 &
&po r=9,theta=333.18 &
&po r=9 ,theta=326.82 &

&mt mtid=1
```

```
aeasy=0,gamper=1
hcept=-10800,bcept=11600 &

&mt mtid=2
aeasy=210,gamper=1
hcept=-10800,bcept=11600 &

&mt mtid=3
aeasy=60.0,gamper=1
hcept=-10800,bcept=11600 &

&mt mtid=4
aeasy=270.0,gamper=1
hcept=-10800,bcept=11600 &

&mt mtid=5
aeasy=120.0,gamper=1
hcept=-10800,bcept=11600 &

&mt mtid=6
aeasy=330.0,gamper=1
hcept=-10800,bcept=11600 &

&mt mtid=7
aeasy=180.0,gamper=1
hcept=-10800,bcept=11600 &

&mt mtid=8
aeasy=90.0,gamper=1
hcept=-10800,bcept=11600 &
```

APPENDIX B

CROSS-SECTION DATA

Cross-Sections used to determine the rate coefficients for the different processes.

Dissociative Attachment Reaction.

e + H2 ----> H + H-
Ref: Wadehra'79

Energy	Cross-section
3.72	0
3.75	3.00E-21
4.00	2.00E-21
4.37	1.00E-21
4.42	9.00E-22
4.50	8.00E-22
4.57	7.00E-22
4.64	6.00E-22
4.71	5.00E-22
4.81	4.00E-22
5.21	0

e + H2_v1 ----> H + H-
Ref: Wadehra'79

Energy	Cross-section
3.2	0
3.25	8.34E-20
3.32	8.00E-20
3.4	7.00E-20
3.48	6.00E-20
3.58	5.00E-20
3.7	4.00E-20
3.86	3.00E-20
4.05	2.00E-20
4.35	1.00E-20
4.45	8.00E-21
4.65	5.00E-21
4.85	3.00E-21
5	2.00E-21
5.3	0

e + H2_v2 ----> H + H-
Ref: Wadehra'79

Energy	**Cross-section**
2.74	0
2.75	1.05E-18
2.875	9.00E-19
2.94	8.00E-19
3	7.00E-19
3.08	6.00E-19
3.21	5.00E-19
3.42	3.00E-19
3.6	2.00E-19
3.9	1.00E-19
4	8.00E-20
4.15	6.00E-20
4.3	4.00E-20
4.6	2.00E-20
4.88	1.00E-20
5.16	0

e + H2_v3 ----> H + H-
Ref: Wadehra'79

Energy	**Cross-section**
2.25	0
2.26	7.45E-18
2.424	6.00E-18
2.64	4.00E-18
2.95	2.00E-18
3.3	1.00E-18
3.34	9.00E-19
3.45	7.00E-19
3.6	5.00E-19
3.8	3.00E-19
3.96	2.00E-19
4.25	1.00E-19
4.38	8.00E-20
4.5	6.00E-20
4.66	4.00E-20
4.95	2.00E-20
5.24	0

e + H2_v4 ----> H + H-
Ref: **Wadehra'79**

Energy	Cross-section
1.82	0
1.85	3.20E-17
2	2.32E-17
2.15	2.00E-17
2.45	1.00E-17
2.57	8.00E-18
2.7	6.00E-18
2.9	4.00E-18
3.2	2.00E-18
3.54	1.00E-18
3.6	9.00E-19
3.68	7.00E-19
3.8	5.00E-19
4	3.00E-19
4.18	2.00E-19
4.5	1.00E-19
4.6	8.00E-20
4.75	6.00E-20
4.95	4.00E-20
5.35	0

e + H2_v5 ----> H- + H
Ref: **Bailey'90**

Energy	Cross-section
1.373	0
1.408	1.05E-16
1.613	8.00E-17
1.768	6.00E-17
1.901	4.00E-17
2.331	2.00E-17
2.676	1.00E-17
2.78	8.00E-18
2.9	6.00E-18
3.09	4.00E-18
3.32	2.00E-18
3.74	1.00E-18
3.86	8.00E-19
3.97	6.00E-19
4.14	4.00E-19
4.36	2.00E-19
4.64	1.00E-19
4.75	8.00E-20
4.86	6.00E-20
5.03	4.00E-20

e + H2_v6 ----> H- + H
Ref: **Bailey'90**

c	Cross-section
1.0387	0
1.042	2.47E-16
1.225	2.00E-16
1.613	1.00E-16
1.72	8.00E-17
1.89	6.00E-17
2.08	4.00E-17
2.44	2.00E-17
2.76	1.00E-17
2.88	8.00E-18
2.99	6.00E-18
3.16	4.00E-18
3.46	2.00E-18
3.74	1.00E-18
3.86	8.00E-19
3.97	6.00E-19
4.14	4.00E-19
4.43	2.00E-19
4.79	1.00E-19
4.85	8.00E-20
5	6.00E-20

e + H2_v7 ----> H- + H
Ref: **Bailey'90**

Energy	Cross-section
0.687	0
0.69	4.31E-16
0.754	4.00E-16
1.127	2.00E-16
1.493	1.00E-16
1.61	8.00E-17
1.77	6.00E-17
1.9	4.00E-17
2.33	2.00E-17
2.68	1.00E-17
2.78	8.00E-18
2.9	6.00E-18
3.09	4.00E-18
3.32	2.00E-18
3.74	1.00E-18
3.86	8.00E-19
3.97	6.00E-19
4.14	4.00E-19
4.36	2.00E-19
4.64	1.00E-19
4.75	8.00E-20
4.86	6.00E-20
5.03	4.00E-20

e + H2_v8 ----> H- + H

Ref: **Bailey'90**

Energy	**Cross-section**
0.356	0
0.359	3.39E-16
0.697	2.00E-16
1.056	1.00E-16
1.19	8.00E-17
1.34	6.00E-17
1.55	4.00E-17
1.96	2.00E-17
2.32	1.00E-17
2.42	8.00E-18
2.55	6.00E-18
2.75	4.00E-18
3.13	2.00E-18
3.45	1.00E-18
3.58	8.00E-19
3.66	6.00E-19
3.86	4.00E-19
4.14	2.00E-19
4.46	1.00E-19
4.53	8.00E-20
4.68	6.00E-20
4.85	4.00E-20

e + H2_v9 ----> H- + H

Ref: **Bailey'90**

Energy	**Cross-section**
0.109	0
0.1127	4.64E-16
0.204	4.00E-16
0.563	2.00E-16
0.92	1.00E-16
1.05	8.00E-17
1.19	6.00E-17
1.345	4.00E-17
1.7	2.00E-17
2.06	1.00E-17
2.24	8.00E-18
2.4	6.00E-18
2.61	4.00E-18
2.96	2.00E-18
3.3	1.00E-18
3.34	9.00E-19
3.45	7.00E-19
3.6	5.00E-19
3.8	3.00E-19
3.96	2.00E-19
4.25	1.00E-19
4.38	8.00E-20
4.5	6.00E-20
4.66	4.00E-20
4.95	2.00E-20
5.24	0

Electron Detachment process.

e + H- ----> e + e + H

Ref: **Takayanagi'78**

Energy	**Cross-section**
0.75	0
0.9	2.00E-17
1	5.00E-17
1.2	6.00E-17
1.5	1.15E-16
2	1.25E-16
2.5	2.00E-16
3	3.00E-16
4	5.00E-16
5	8.00E-16
6	1.20E-15
7	2.00E-15
8	2.35E-15
9	3.00E-15
10	3.24E-15

15	3.59E-15
20	3.50E-15
25	3.28E-15
30	3.22E-15
40	3.00E-15
50	2.63E-15
60	2.44E-15
70	2.18E-15
80	2.03E-15
90	1.88E-15
100	1.68E-15
200	1.04E-15
300	7.00E-16
400	5.49E-16
500	4.40E-16
600	3.65E-16
700	3.15E-16
800	2.66E-16
900	2.43E-16
1000	2.25E-16

E-V Process

e + H2 ----> e + H2_v1

Ref: **Hiskes'92**

Energy	**Cross-section**
15	0
20	3.19E-18
20.94	3.79E-18
26.28	4.72E-18
32.56	5.59E-18
40	6.12E-18
46.28	6.31E-18
52.56	6.37E-18
60	6.28E-18
66.28	6.16E-18
72.56	5.99E-18
80	5.84E-18
86.28	5.69E-18
92.56	5.54E-18
100	5.40E-18
106.28	5.26E-18
112.56	5.16E-18
119.06	5.07E-18
120	5.01E-18
198	0

e + H2 ----> e + H2_v2
Ref: **Hiskes'92**

Energy	Cross-section
15.1	0
20	2.87E-18
2.09E+01	3.42E-18
2.63E+01	4.25E-18
3.26E+01	4.99E-18
4.00E+01	5.52E-18
4.63E+01	5.81E-18
5.26E+01	5.73E-18
6.00E+01	5.66E-18
6.63E+01	5.53E-18
7.26E+01	5.42E-18
8.00E+01	5.24E-18
8.63E+01	5.12E-18
9.26E+01	4.88E-18
1.00E+02	4.85E-18
1.06E+02	4.72E-18
1.13E+02	4.61E-18
1.19E+02	4.54E-18
1.20E+02	4.48E-18
1.91E+02	0

e + H2 ----> e + H2_v3
Ref: **Hiskes'92**

Energy	Cross-section
1.51E+01	0
2.00E+01	2.87E-18
2.09E+01	3.42E-18
2.63E+01	4.25E-18
3.26E+01	4.99E-18
4.00E+01	5.52E-18
4.63E+01	5.81E-18
5.26E+01	5.73E-18
6.00E+01	5.66E-18
6.63E+01	5.53E-18
72.56	5.42E-18
80	5.24E-18
86.28	5.12E-18
92.56	4.88E-18
100	4.85E-18
106.28	4.72E-18
112.56	4.61E-18
119.06	4.54E-18
120	4.48E-18
191	0

e + H2 ----> e + H2_v4
Ref: **Hiskes'92**

Energy	Cross-section
15.1	0
20	2.87E-18
2.09E+01	3.42E-18
2.63E+01	4.25E-18
3.26E+01	4.99E-18
4.00E+01	5.52E-18
4.63E+01	5.81E-18
5.26E+01	5.73E-18
6.00E+01	5.66E-18
6.63E+01	5.53E-18
7.26E+01	5.42E-18
8.00E+01	5.24E-18
8.63E+01	5.12E-18
9.26E+01	4.88E-18
1.00E+02	4.85E-18
1.06E+02	4.72E-18
1.13E+02	4.61E-18
1.19E+02	4.54E-18
1.20E+02	4.48E-18
1.91E+02	0

e + H2 ----> e + H2_v5
Ref: **Hiskes'92**

Energy	Cross-section
15.1	0
20	2.70E-18
20.94	3.22E-18
26.28	4.03E-18
32.56	4.76E-18
40	5.36E-18
46.28	5.39E-18
52.56	5.40E-18
60	5.35E-18
66.28	5.24E-18
72.56	5.13E-18
80	4.97E-18
86.28	4.85E-18
92.56	4.73E-18
100	4.60E-18
106.28	4.48E-18
112.56	4.37E-18
119.06	4.28E-18
120	4.26E-18
302	0

e + H2 ----> e + H2_v6
Ref: Hiskes'92

Energy	Cross-section
14.95	0
20	2.38E-18
2.09E+01	2.82E-18
2.63E+01	3.54E-18
3.26E+01	4.18E-18
4.00E+01	4.59E-18
4.63E+01	4.72E-18
5.26E+01	4.75E-18
6.00E+01	4.71E-18
6.63E+01	4.61E-18
7.26E+01	4.50E-18
8.00E+01	4.38E-18
8.63E+01	4.29E-18
9.26E+01	4.17E-18
1.00E+02	4.06E-18
1.06E+02	3.97E-18
1.13E+02	3.87E-18
1.19E+02	3.81E-18
1.20E+02	3.76E-18
1.95E+02	0

e + H2 ----> e + H2_v7
Ref: Hiskes'92

Energy	Cross-section
14.2	0
20	2.22E-18
20.94	2.58E-18
26.28	3.22E-18
32.56	3.84E-18
40	4.25E-18
46.28	4.38E-18
52.56	4.40E-18
60	4.37E-18
66.28	4.29E-18
72.56	4.20E-18
80	4.10E-18
86.28	3.99E-18
92.56	3.91E-18
100	3.78E-18
106.28	3.70E-18
112.56	3.61E-18
119.06	3.54E-18
120	3.51E-18
237	0

e + H2 ----> e + H2_v8
Ref: Hiskes'92

Energy	Cross-section
14.4	0
20	1.91E-18
2.09E+01	2.23E-18
2.63E+01	2.81E-18
3.26E+01	3.33E-18
4.00E+01	3.66E-18
4.63E+01	3.79E-18
5.26E+01	3.83E-18
6.00E+01	3.78E-18
6.63E+01	4.15E-18
7.26E+01	3.65E-18
8.00E+01	3.55E-18
8.63E+01	3.46E-18
9.26E+01	3.37E-18
1.00E+02	3.28E-18
1.06E+02	3.20E-18
1.13E+02	3.10E-18
1.19E+02	3.03E-18
1.20E+02	3.00E-18
2.35E+02	0

e + H2 ----> e + H2_v9
Ref: Hiskes'92

Energy	Cross-section
15.4	0
20	1.59E-18
20.94	1.92E-18
26.28	2.37E-18
32.56	2.77E-18
40	3.04E-18
46.28	3.14E-18
52.56	3.17E-18
60	3.14E-18
66.28	3.10E-18
72.56	3.02E-18
80	2.95E-18
86.28	2.87E-18
92.56	2.80E-18
100	2.71E-18
106.28	2.64E-18
112.56	2.55E-18
119.06	2.51E-18
120	2.47E-18
197	0

Associative Attachment Process.

H- + H ----> e + H2
Ref: **Janev'89**

Energy	Cross-section
1.00E-02	2.04E-15
2.00E-02	2.09E-15
3.00E-02	2.12E-15
4.00E-02	2.14E-15
5.00E-02	2.15E-15
6.00E-02	2.16E-15
7.00E-02	2.17E-15
8.00E-02	2.17E-15
9.00E-02	2.17E-15
1.00E-01	2.17E-15
1.50E-01	2.16E-15
2.00E-01	2.15E-15
2.50E-01	2.14E-15
3.00E-01	2.13E-15
3.50E-01	2.13E-15
4.00E-01	2.13E-15
0.45	2.13E-15
0.5	2.13E-15

Mutual Neutralization Process.

H+ + H- ----> H + H
Ref: **Burnett'90**

Energy	Cross-section
0.01	5.83E-14
2.00E-02	7.47E-14
3.00E-02	8.31E-14
4.00E-02	8.75E-14
5.00E-02	8.97E-14
6.00E-02	9.06E-14
7.00E-02	9.07E-14
8.00E-02	9.03E-14
9.00E-02	8.96E-14
1.00E-01	8.87E-14
1.50E-01	8.37E-14
2.00E-01	7.89E-14
2.50E-01	7.51E-14
3.00E-01	7.18E-14
3.50E-01	6.88E-14
4.00E-01	6.65E-14
4.50E-01	6.45E-14
5.00E-01	6.28E-14

H2+ + H- ----> H2 + H
Ref: **Eerden'93**

Energy	Cross-section
0.01	9.44E-13
0.02	8.88E-13
0.03	8.12E-13
0.04	7.49E-13
0.05	6.99E-13
0.06	6.59E-13
0.07	6.27E-13
0.08	6.01E-13
0.09	5.78E-13
0.1	5.60E-13
0.15	4.97E-13
0.2	4.61E-13
0.25	4.38E-13
0.3	4.22E-13
0.35	4.11E-13
0.4	4.03E-13
0.45	3.97E-13
0.5	3.93E-13

H3+ + H- ----> H2 + H + H

Ref: **Eerden'93**

Energy	**Cross-section**
0.01	8.90E-13
2.00E-02	8.38E-13
3.00E-02	7.65E-13
4.00E-02	7.06E-13
5.00E-02	6.59E-13
6.00E-02	6.21E-13
7.00E-02	5.91E-13
8.00E-02	5.66E-13
9.00E-02	5.45E-13
1.00E-01	5.28E-13
1.50E-01	4.68E-13
2.00E-01	4.34E-13
2.50E-01	4.13E-13
3.00E-01	3.98E-13
3.50E-01	3.88E-13
4.00E-01	3.80E-13
4.50E-01	3.75E-13
5.00E-01	3.71E-13